Modeling of Salinity Effects on Waterflooding of Petroleum Reservoirs

Alexeev, Artem

Publication date:
2015

Document Version
Peer reviewed version

Modeling of Salinity Effects on Waterflooding of Petroleum Reservoirs

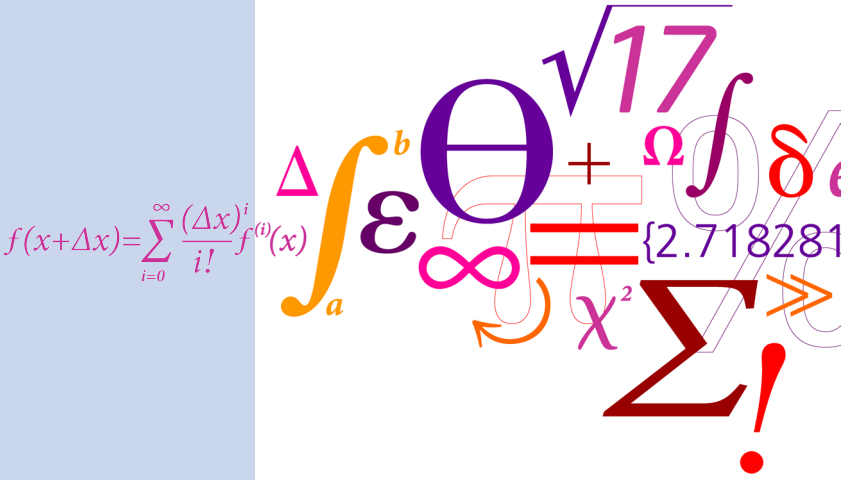

Artem Alexeev
Ph.D. Thesis
December 2015

DTU Chemical Engineering
Department of Chemical and Biochemical Engineering

Modeling of Salinity Effects on Waterflooding of Petroleum Reservoirs

Artem Alexeev

PhD Thesis

December 2015

Center for Energy Resources Engineering
Department of Chemical and Biochemical Engineering
Technical University of Denmark
Kongens Lyngby, Denmark

DTU Chemical Engineering
Department of Chemical and Biochemical Engineering

Technical University of Denmark
Department of Chemical and Biochemical Engineering
Building 229, DK-2800 Kongens Lyngby, Denmark
Phone: +45 4525 2800
Fax: +45 4525 4588
Web: www.cere.dtu.dk

Printed by GraphicCo A/S, Denmark

Preface

This thesis is submitted as partial fulfillment of the requirement for the Ph.D. degree at Technical University of Denmark (DTU). The work has been carried out at the Department of Chemical and Biochemical Engineering and Center for Energy Resources Engineering (CERE) from September 2012 to November 2015 under the supervision of Associate Professor Alexander Shapiro as the main supervisor and Associate Professor Kaj Thomsen as the co-supervisor. The project was supported by DONG Energy, Mærsk Oil, and the Danish EUDP program (a program for development and demonstration of energy technology) under the Danish Energy Agency, and by the Danish research councils.

First and foremost, I wish to express my deepest gratitude to Alexander Shapiro for his guidance on my research. I admire your profound knowledge in many different fields of science and beyond which you have been sharing with me during our numerous discussions. Your encouragement, patience, and support were extremely valuable to me. I am also grateful to Kaj Thomsen and all members of the SmartWater project for collaboration, useful discussions, and suggestions.

During the course of the study, I had a chance to spend 3 month at the Australian School of Petroleum (ASP), University of Adelaide, South Australia. Special thanks to Professor Pavel Bedrikovetsky for kindly hosting my visit and making me feel a part of ASP. Thanks to my friends at ASP, and especially Sara Borazjani for the interesting collaboration.

I would especially like to acknowledge my friend and colleague Tina Katika, who provided me with a lot of help and support. Thank you for our chitchats during coffee breaks at DTU and numerous profound scientific discussions held in Copenhagen bars.

I am also grateful to my dear colleagues at CERE for providing a comfortable and stimulating research environment.

Kongens Lyngby, December 2015

Artem Alexeev

Summary

Smart Water flooding is an enhanced oil recovery (EOR) technique that is based on the injection of chemistry-optimized water with changed ionic composition and salinity into petroleum reservoirs. Extensive research that has been carried out over the past two decades has clearly demonstrated that smart water flooding can improve the ultimate oil recovery both in carbonate and sandstone reservoirs. A number of different physicochemical mechanisms of action were proposed to explain the smart water effects, but none of them has commonly been accepted as a determining mechanism.

Most of the experimental studies concerning the smart water effects recognize importance of the chemistry of reservoir rocks that manifests itself in dissolution and precipitation of rock minerals and adsorption of specific ions on the rock surface. The brine-rock interactions may affect the wetting state of the rock and in some cases result in mobilization of the trapped oil.

In this thesis, we set up a generic model for the reactive transport in porous media to investigate how different mechanisms influence the oil recovery, pressure distribution and composition of the brine during forced displacement. We consider several phenomena related to the smart water effects, such as mineral dissolution, adsorption of potential determining ions in carbonate rocks, and mechanisms that influence mobilization of the trapped oil and its transport.

Dissolution of minerals occurs due to the different compositions of the injected brine and the formation water that is initially in equilibrium with the reservoir rock. We consider a displacement process in one dimension with dissolution affecting both the porosity/permeability of the rock and the density of the brine. Extending previous studies, we account for the different individual volumes of mineral in solid and in solution, which is found to affect slightly the velocity of the displacement front.

The rate of dissolution is found to have a significant influence on the evolution of the rock properties. At low reaction rates, dissolution occurs across the entire region between the injection and production sites resulting in heterogeneous porosity and permeability fields. Fast dissolution resembles formation of wormholes with a significant change in porosity and permeability close to the injection site.

Further, we study the mechanisms that can govern the mobilization of residual oil and its flow in porous media. The oil trapped in the swept zones after conventional flooding is present in a form of disconnected oil drops, or *oil ganglia*. While the macroscopic theory of multiphase flow assumes that fluid phases flow in their own pore networks and do not

influence each other, the flow of disconnected oil ganglia requires an alternative description. We address this problem by considering a micromodel for the two-phase flow in a single angular pore-body.

On the micro-level, both fluids can be present in a single pore body and interact during the flow. Considering water-wet systems, we find that presence of the water on the surface of the rock and in the corner filaments of pore bodies results in a larger velocity of the viscous flow of the oil phase due to the increased area of the moving oil-water interface. Moreover, the flow of oil may be induced solely by the action of viscous forces at the oil-water interface, which appears to be a new mechanism for the transport of disconnected oil ganglia in porous media. We derive correlations that allow calculating the flow velocities of fluid phases in single pore bodies based on the pore fluid saturations.

Based on the microscale considerations, we develop a macroscopic model of displacement accounting for the effects associated with oil ganglia. The model is based on the assumption that wettability alteration toward increased water-wetness caused by the presence of active species in the injected brine results in formation of the wetting films on the surface of the rock. Oil ganglia are mobilized and carried by the slow flow of wetting films. Considering simplistic pore-network model, we derive the macroscopic system of equations involving description of the transport of oil ganglia. As a result of numerical modeling of the tertiary recovery process, it is found that production of oil ganglia may continue for a long time of injection of around 10 to 20 PVI.

Unlike the conventional models of chemical flooding, where mobilized oil bank travels ahead of the concentration front, the oil ganglia model predicts that the mobilized oil is produced after the active species reaches the effluent. Further extension of the model is achieved by introduction of the non-equilibrium alteration of wettability and non-instantaneous oil mobilization. Such modifications may explain the delay observed in some experiments, where mobilized oil is produced during a long time after several pore volumes of injection.

One of the possible chemical mechanisms through which the mobilization of the residual oil may occur in carbonates is alteration of the electrostatic potential of the surface. Reduction of the surface charge due to adsorption of the potential determining ions results in the decrease in oil affinity towards the surface of the rock. We establish a mathematical model that takes into account adsorption of the potential determining ions: calcium, magnesium, and sulfate, on the chalk surface, to investigate how the composition of the injected brine affects the equilibrium surface composition and how adsorption process affects the composition of the produced brine. We use experimental data on the produced brine composition from the flow-through experiments to estimate the parameters of the adsorption model. The computations suggest that there is no evidence of usually assumed stronger adsorption of magnesium ion compared to calcium at high temperatures. In order to investigate the effect of surface composition on the flooding efficiency, we combine the adsorption model with the Buckley-Leverett model and perform simulations of the experiments concerning flooding in the water-wet outcrop chalk. Computations of the

equilibrium surface composition demonstrate a correlation between the concentration of the adsorbed sulfate and the ultimate recovery observed in the experiments indicating that a more negatively charged surface of chalk could be a factor that affects the recovery efficiency without wettability modification.

Resume på dansk

”Smart water flooding” er en forbedret olieindvindings (EOR) teknik, der er baseret på injektion af vand med kemisk optimeret saltindhold i olie reservoirer. Omfattende forskning, der er udført i løbet af de seneste to årtier har tydeligt vist, at smart water flooding kan forbedre den ultimative olieindvindingsgrad både i carbonat- og i sandstens- reservoirer. Der er blevet foreslået en række forskellige fysisk-kemiske mekanismer til at forklare smart water effekten, men ingen af dem har været almindeligt accepteret som den dominerende mekanisme.

De fleste af de eksperimentelle undersøgelser vedrørende smart water effekter anerkender betydningen af den kemiske interaktion mellem reservoir-klippe og den gennemstrømmende saltopløsning, der manifesterer sig ved opløsning og udfældning af klippe-mineraler og adsorption af specifikke ioner på klippens overflade. Interaktionen med saltopløsningen kan påvirke klippens befugtningstilstand og i nogle tilfælde resultere i mobilisering af blokeret olie.

I denne afhandling, opstiller vi en generel model for reaktiv transport i porøse medier for at undersøge, hvordan forskellige mekanismer påvirker olieindvinding, trykfordeling og sammensætning af saltopløsninger under tvungen gennemstrømning. Vi behandler flere fænomener i relation til smart water effekten, såsom opløsning af mineraler, adsorption af potentielt vigtige ioner i kalksten, og mekanismer, der har indflydelse på mobilisering af den blokerede olie og transporten af denne.

Opløsning af mineraler finder sted på grund af de forskellige sammensætninger af den injicerede saltopløsning og formationsvandet, der oprindeligt var i ligevægt med reservoiret. Vi betragter en gennemstrømningsproces i en enkelt dimension hvor opløsning af mineralsk materiale påvirker både porøsitet/permeabilitet af reservoiret og densiteten af saltopløsningen. Vi videreudvikler tidligere undersøgelser ved at redegøre for de forskellige individuelle mængder af mineral i fast form og i opløsning, som har vist sig at have en svag effekt på hastigheden af gennemstrømningsfronten.

Hastigheden for mineralers opløsning viser sig at have en betydelig indflydelse på udviklingen af reservoirets egenskaber. Ved lave reaktionshastigheder forekommer opløsning i hele området mellem injektions- og produktionssteder og resulterer i heterogene porøsitet og permeabilitet områder. Hurtig opløsning ligner dannelsen af ormehuller som fører til en betydelig ændring i porøsitet og permeabilitet tæt på injektionsstedet.

Endvidere studerer vi de mekanismer, der kan kontrollere mobiliseringen af resterende olie og dens flow i porøse medier. Den olie der er tilbage i de bestrøgne zoner efter konventionelle udvindinger er til stede i form af separate oliedråber eller olie ganglia. Den makroskopiske teori om flerfasestrømning forudsætter, at fluide faser strømmer i deres egne pore netværk uden at påvirke hinanden. Strømmen af sparate olie ganglia kræver en alternativ beskrivelse. Vi løser dette problem ved at overveje en micromodel for tofaset strømning i et enkelvinklet porevolumen.

På mikro-niveau, kan begge væsker være til stede i et enkelt pore volumen og interagere mens væsken strømmer. For water-wet systemer, finder vi, at tilstedeværelsen af vand på overfladen af reservoirmaterialet resulterer i en større hastighed i den viskøse strømning af oliefasen på grund af det øgede grænsefladeareal mellem olie og vand. Desuden kan oliestrømmen sættes i bevægelse udelukkende induceret af virkningen af viskøse kræfter ved olie-vand-grænsefladen. Dette lader til at være en ny mekanisme til transport af olie afbrudt ganglier i porøse medier. Vi udleder sammenhænge, som tillader beregning af strømningshastigheder af væskefaser i individuelle porer baseret på mætningsgraden af porens væske.

Baseret på de mikroskala betragtninger, udvikler vi en makroskopisk model for strømning i porer, der indberegner de virkninger, der er forbundet med olie ganglia. Modellen er baseret på den antagelse, at befugtningsændring mod øget water-wetness forårsaget af tilstedeværelsen af aktive ioner i det injicerede saltvand resulterer i dannelse af en fugt-film på overfladen af reservoirmaterialet. Olie ganglia mobiliseres og føres frem af den langsomme strøm af fugt-film. I betragtning af denne simplistiske pore-netværksmodel, udleder vi det makroskopiske ligningsystem, der involverer beskrivelse af transport af olie ganglia. Som et resultat af numerisk modellering af den tertiære indvindingsproces, er det konstateret, at produktionen af olie ganglia kan fortsætte i lang tid under injektionen, op til 10 til 20 PVI.

I modsætning til de traditionelle modeller for kemiske udskylninger, hvor en mobiliseret olie front bevæger foran koncentrationfronten, forudsiger olie ganglia modellen at den mobiliserede olie produceres efter de aktive ioner når frem. Yderligere udvidelse af modellen er opnået ved indføring af non-equilibrium ændring af befugtning og forsinket olie mobilisering. Sådanne modifikationer kan forklare forsinkelsen observeret i nogle eksperimenter, hvor mobiliseret olie produceres i lang tid efter flere porevolumener er injiceret.

En af de mulige kemiske mekanismer der mobiliserer resterende olie i kalk reservoirer er ændring af det elektrostatiske potentiale af overfladen. Reduktion af overfladeladningen som følge af adsorption af de potential bestemmende ioner resulterer i et fald i oliens affinitet for reservoiroverfladen. Vi etablere en matematisk model, der tager højde for adsorption af potential bestemmelse ioner: calcium, magnesium og sulfat på kalk overflader for at undersøge, hvordan sammensætningen af den injicerede saltopløsning påvirker ligevægten med overfladen, og hvordan adsorptionsprocessens påvirker sammensætningen af det

producerede saltvand. Vi bruger eksperimentelle data målt på saltvand produceret ved gennemstrømning af reservoirkerne. Beregningerne tyder på, at der ikke er tegn på en stærkere adsorption af magnesium ion sammenlignet med calcium ion ved høje temperaturer, som det ellers ofte antages.

For at undersøge overfladesammensætningens effekt på gennemstrømningens effektivitet, kombinerer vi adsorption modellen med Buckley-Leverett modellen og udfører simuleringer af forsøgene vedrørende gennemstrømninger i water-wet outcrop kridt. Beregninger af overfladesammensætningen ved ligevægt demonstrerer en korrelation mellem koncentrationen af den adsorberede sulfat og den opnåede olieindvinding observeret i forsøgene. Dette viser at en mere negativt ladet kridtoverflade kunne være en faktor, der påvirker olieproduktionens effektivitet uden at ændre wettability.

Contents

1

Introduction

Waterflooding of petroleum reservoirs was introduced more than a century ago and since then it is one of the most widely applied oil recovery techniques. It is applied for two particular purposes: give pressure support and displace oil by pressure and viscous forces. The key factors that make implementation of waterflooding attractive are: (1) water is readily available in large quantities; (2) injection of water is efficient for displacing oil and (3) it is relatively inexpensive so that operational costs are low. Nowadays, waterflooding is almost a synonym with the secondary recovery.

The tertiary recovery techniques are developed in order to improve the recovery that is available by means of waterflooding and are commonly named as an Enhanced Oil Recovery (EOR). EOR is targeting at the hydrocarbons that remain in the formation due to either low sweep efficiency or trapping of oil in the swept zones. The three conventional EOR techniques include (1) chemical flooding (polymer, foam, surfactant); (2) thermal flooding (steam, in situ combustion, how water) and (3) gas injection.

Traditionally, the composition of the injected water was not considered to play a significant role in industrial applications as a potential to increase recovery. Indeed, if the composition of the injected water is similar to the formation water, one should not expect any changes in the crude oil/brine/rock interactions. If, however, the injected water differs significantly from the formation water in composition, it may disturb the established chemical equilibrium in the reservoir. Extensive studies performed for different crude oil/brine/rock systems during the last 20 years clearly demonstrated that when a new equilibrium is established it may change the wetting properties of the fluids and result in a number of other effects leading to enhanced recovery. Injection of water with a composition deliberately altered to improve recovery, and different from the formation water, is named Smart Water flooding (SWF). The approaches that have been developed with regard to SWF so far include the modified seawater flooding in carbonate reservoirs and Low Salinity Waterflooding (LSW) in sandstone reservoirs. Recently LSW found its application in carbonates as well.

In this chapter, we will review the major progress in the smart water studies, established features, proposed mechanisms and modeling attempts. A major attention is paid to flooding and imbibition in carbonate rocks while we feel important that low salinity effects are also discussed.

1.1 Enhanced Oil Recovery by Smart Water Flooding

1.1.1 Seawater Flooding in Carbonates

A success of seawater flooding may be illustrated by its application in the Ekofisk field [1]. The initial estimated recovery of 17% of original oil in place (OOIP) was increased to 46% taking into account the potential of the seawater flooding that started in 1983. Current estimation of the ultimate recovery constitutes 55% OOIP, and it is speculated that additional 10% can be recovered by optimizing the seawater composition [2].

Due to the exceptional performance of the seawater injection into the Ekofisk chalk formation, Austad and co-workers initiated a series of studies on seawater-chalk interactions and their influence on the recovery. These studies were mainly focused on spontaneous imbibition experiments [3, 4], flow-through experiments [5, 6] and several core flooding experiments [7]. In the recent years, a growing number of studies on chalk, dolomite and limestone outcrop and reservoir cores have demonstrated improved oil recovery in coreflood [8-10] and spontaneous imbibition [11, 12] experiments. Below we present a brief overview of the consistent patterns observed in these experiments.

1.1.1.1 Effect of composition

Multivalent ions, such as SO_4^{2-} , Ca^{2+} and Mg^{2+} are readily present in the seawater and are reactive towards the chalk surface. These ions are called the potential determining ions due to their ability to adsorb on the carbonate rock changing the surface charge that is suggested to affect the interaction between the oil and the rock surface [3]. Therefore, the potential determining ions are considered to play an important role in the smart water effects in carbonates.

Strand et al. [13] found that presence of the sulfate ion in addition to a cationic surfactant improves the recovery by spontaneous imbibition. It was suggested that sulfate is adsorbed on the surface and acts as a catalyst for the reaction between the catalytic agent and carboxylic material in oil. It was further demonstrated that sulfate ions can improve recovery in the absence of a surfactant: Zhang and Austad [14] observed improved recovery during spontaneous imbibition in the Stevns Klint outcrop chalk as concentration of sulfate in the imbibing brine was increased. A significant increase in recovery of around 40% OOIP and more was observed as the sulfate concentration varied from zero to four times the concentration in seawater. No increase in recovery was reportedly observed in the spontaneous imbibition experiments, in the cases where divalent cations Ca^{2+} and Mg^{2+} were not present in the imbibing brine.

Zahid et al. [8] observed improvement of the oil recovery during the waterflooding in outcrop chalk cores when applying brines with different concentrations of the sulfate. Incremental

recovery, obtained for both secondary and tertiary mode corefloods, was in the range of 5−10% with a slightly better performance of sulfate-rich brines with three times the concentration in the seawater.

Flow-through experiments demonstrated that adsorption of sulfate from the seawater is determined by the concentrations of calcium and magnesium in the injected fluid [5] suggesting that the combined effect of potential determining ions should be considered. Zhang et al. [5] observed a marginal increase in oil recovery during the spontaneous imbibition of $MgCl_2$ solution that contained no sulfate. Karoussi et al. [11] investigated separate effects of sulfate and magnesium ions on the efficiency of the spontaneous imbibition process in the absence of calcium. Water saturated with the magnesium ion showed the highest oil recovery, compared to the water that contained sulfate only.

During the spontaneous imbibition experiments performed by Zhang et al. [5] the oil recovery increased from 28% to 60% as calcium concentration was varied from zero to four times the concentration in the seawater. Calcium ion improved recovery both at low (40°C) and high temperatures ($T > 90°C$), while magnesium ion worked only at high temperatures. It was suggested that reactivity of the magnesium ion significantly increases with temperature, so that it can substitute calcium on the carbonate surface.

Fathi et al. [7] studied the effect of both ionic composition and salinity on the spontaneous imbibition process. Decreasing salinity of brine resulted in a substantial decrease in recovery, from 60 to 15% OOIP. Additionally, no increase in recovery was observed during forced displacement after changing from seawater to diluted seawater injection. It was also reported that decreasing NaCl concentration has a positive effect on the imbibition process: both the imbibition rate and oil recovery increased with seawater depleted in NaCl. Presence of the chlorine ion was suggested to decrease the sulfate reactivity towards the calcite surface.

Rezaei Doust et al. [15] suggested that presence of SO_4^{2-} and either Ca^{2+}/Mg^{2+}, or both ions is a necessary condition for the smart water effect in carbonates. However, in several studies the potential determining ions were selectively removed or replaced by other ions, while the smart water effect was still observed. Gupta et al. [9] replaced sulfate in brine with the borate and phosphate ions. Core flooding with these modified brines in tertiary recovery modes resulted in increased oil production. Adding borate and phosphate gave 15% and 20% incremental recovery respectively, while the incremental recovery for the flooding with sulfate-rich seawater was in the range 5–9%. The smart water effect was also observed in the tertiary mode corefloods with the use of seawater brine without sulfate and formation brine without calcium and magnesium [9]. During the secondary mode corefloods, injection of distilled water yielded additional 11.6% oil recovery in the experiments of Al-Attar et al. [16]. Romanuka et al. [12] observed improved oil recovery with the imbibing brines that did not contain sulfate or all the three multivalent ions.

1.1.1.2 Effect of temperature

Temperature is an important parameter when considering most of the water-based EOR techniques. The smart water effects in carbonates have been observed at temperatures below 90°C in spontaneous imbibition experiments [5, 17, 18]. However, increasing temperature always resulted in a significant improvement in recovery [14, 19, 20]. Meanwhile, in the core flood experiments temperature has a much less definite effect; some secondary and tertiary core flood experiments showed no or only slight increase in recovery with temperature [8, 21].

It is also suggested that water-wetness of carbonate rocks increases with temperature [22]. Yu et al. [23] observed contact angle shifting from intermediate-wet to water-wet, as temperature increased from 20 to 130°C, with seawater and seawater with four times more sulfate. Zhang et al. [5] observed increased adsorption of sulfate from seawater in the flow-through experiments on the outcrop chalk under increasing temperatures. Larger adsorption of sulfate lowers the surface charge of the carbonate rock increasing its water-wetness.

1.1.1.3 Effect of low salinity

The low salinity water (LSW) was not considered as a possibility for EOR in carbonate rocks for a long time. According to the explanation given by Lager et al. [24], LSW was proved to be successful in sandstones with high clay content and, therefore, low salinity effects were not expected to be observed in carbonates due to typically minimal presence of the clay material. Recent studies, however, contradict this assessment.

Yousef et al. [25] performed flooding experiments on the composite limestone core plugs. They applied a number of brines obtained by diluting the seawater and demonstrated that sequential injection of diluted brine resulted in the recovery increase, after recovery plateau was reached with the previously injected brine. Lowering the solution salinity had an effect on the pressure in the core: an increase in pressure drop was observed when using low salinity brines, which was explained by probable migration of fines.

Zahid et al. [21] performed coreflood experiments on both reservoir and outcrop chalk using diluted seawater at high temperature. The overall efficiency of the seawater flooding of Middle East reservoir chalk was relatively low with a recovery factor of around 30%. Subsequent injection of the two and ten times diluted seawater yielded production of additional 5-10% OOIP. Similar to the previous study, the pressure drop increased on the injection of diluted brines. Meanwhile, increase of recovery was not observed for the outrcrop chalk cores.

Romanuka et al. [12] carried out a series of spontaneous imbibition experiments using chalk, limestone and dolomite core plugs. Application of brines with modified salinity demonstrated significant variance in the magnitude of incremental recovery. Overall, it was concluded that brines with a lower ionic strength promote recovery. It was observed that the chalk core plugs

produce more oil in response to increasing sulfate concentration at high ionic strength, in contrast to the behavior of limestone and dolomite.

1.1.1.4 Effect of oil properties

Strand et al. [4] used two different types of oil to study the impact of the oil acid number. Increase in the acid number (AN) from 0.70 to 1.9 mg of KOH/g resulted in decrease of the ultimate oil recovery by spontaneous imbibition from 30 to 10% OOIP. However, it was not proved that ultimate recovery for the forced displacement is affected by the AN and temperature, as most of the experiments were stopped before the recovery plateau was reached. A larger increment in oil recovery with the use of oil with low AN was also observed in several spontaneous imbibition experiments that were not directly addressing the properties of oil [14].

Fathi et al. [26] studied the interaction of oil with the surface of chalk using two artificially prepared oils different in the acid numbers (AN = 1.5 and 1.8 mg of KOH/g). During the spontaneous imbibition, both the rate and the ultimate recovery were higher for the cores saturated with oil depleted in the water soluble acids (low AN). It was concluded that oil properties affect the wetting state of carbonate rocks mainly due to the presence of the carboxyl groups in oil.

Zahid et al. [27] studied the interaction between the brine and Latin American oil and observed a decrease in oil viscosity in contact with brine as the sulfate concentration was increased. A possible explanation of this phenomena is a specific interaction of ions in the solution with heavy components in oil (aromatics, asphaltenes) so that brine was acting like a polymer. However, a particular mechanism that might explain the interaction of sulfate ions with the crude oil was not identified. Additionally, formation of a new phase, probably an emulsion, was observed during a similar experiment with the Middle East crude oil. The conditions for formation of a stable emulsion were reported to be high temperature (110°C), pressure (300 bars), and high concentration of sulfate.

Chakravarty et al. [28] conducted experiments to study a possibility and conditions for emulsion formation between an oil and an aqueous solution. The mixtures of oil and brine were stirred and left isolated for 18 hours to attain equilibrium. After an incubation period, emulsions could be visually observed if the oil initially contained polar components. It was suggested that heavier oil components participate in the formation of the emulsion. Meanwhile, in the recent Master thesis of Jakub Benicek [29] it was demonstrated that it is light oil components that participate in the formation of the emulsions. The problem needs further study.

1.1.1.5 Effect of rock material

Different mineralogical properties of carbonate rocks may affect the magnitude of response to mechanisms underlying the smart water effects. The outcrop rocks are often used as reservoir rock analogs. However, significant differences between them and the reservoir rocks have been observed in several studies under the same experimental conditions. Therefore, one should be careful when extending conclusions applicable to one rock type to another.

Zahid et al. [30] performed coreflooding experiments on the North Sea reservoir and Stevns Klint outcrop chalks. It was observed that the temperature increase did not have a significant effect on the recovery from the reservoir rocks while flooding in the outcrop chalk was strongly affected as the temperature was increased from 40 to 120°C. It was also reported that increasing the sulfate concentration three times compared to the concentration in seawater resulted in an increase of only 0.7 and 1.2% OOIP from the reservoir core, compared to the recovery achieved the with sulfate free brine.

Spontaneous imbibition experiments performed by Fjelde et al. [31] on the two core plugs from the fractured chalk field demonstrated an insignificant incremental recovery after switching from sulfate-free formation brine to seawater, which was incomparable to the apparent improvement observed in the Stevns Klint outcrop chalk. Fernø et al. [11] studied the effect of sulfate concentration on the oil recovery during spontaneous imbibition in Stevens Klint, Rørdal, and Niobrara outcrop chalks. Effect of increasing the sulfate concentration was different for the three cores in study: no effect was observed in Rørdal and Niobrara plugs, while in the Stevns Klint chalk the incremental recovery was smaller compared to previously reported in other studies.

1.1.1.6 Summary

Available evidence suggests that potential determining ions have a strong effect on the recovery from the carbonate rocks. Most of the published experimental data associate the smart water effect with the wettability alteration towards increased water-wetness for intermediate- and oil-wet carbonates. High temperature ($T > 90°C$) strengthens the magnitude of the smart water effect, especially in the spontaneous imbibition experiments. Nevertheless, high temperature is not the necessary condition, since improved recovery with seawater injection/imbibition has also been observed under low temperatures. Oil properties affect the wetting state of the rock; large acid number of oil indicates a stronger interaction between the polar oil components and the carbonate surface. A positive effect on recovery by seawater flooding and imbibition has been observed both in chalk, limestone and dolomite reservoir and outcrop chalk. However, in several experiments behavior of reservoir and outcrop cores was much different, and there is yet no explanation for the observed deviating behavior.

1.1.2 Recovery Mechanisms

1.1.2.1 Multi-ion exchange

Austad and co-workers [5] proposed that adsorption of sulfate onto positively charged sites on the carbonate surface lowers electrostatic repulsion between the mineral surface and divalent cations. The sulfate adsorption facilitates calcium to approach the surface and react with the negatively charged polar oil components that are adsorbed on the mineral surface, as shown in Figure 1.1A. As a result, organic material can detach from the surface or remain attached through the calcium carboxylate complex (Figure 1.1B). According to this mechanism, sulfate acts as a "catalyst" that helps adsorption of divalent cations by reducing the electrostatic repulsive force. Reactivity of ions increases with temperature. At high temperatures ($T > 90°C$), the magnesium ion becomes dehydrated and reactive [15, 32], and is suggested to displace carboxylate complexes at the calcite surface [5] (Figure 1.1B). As the acidic material is released, the carbonate surface becomes more water-wet.

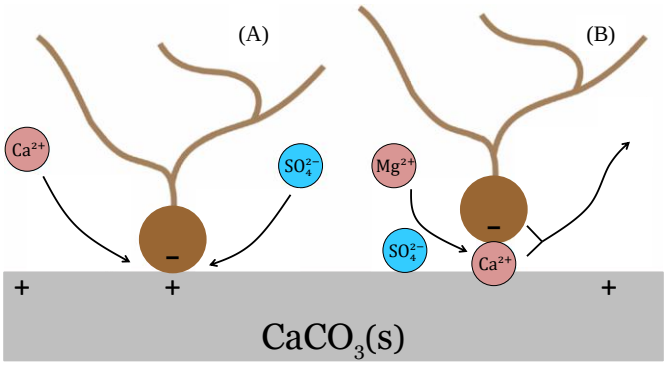

Figure 1.1: Schematic model of the suggested mechanism for the wettability alteration induced by seawater. (A) Proposed mechanism when Ca^{2+} and SO_4^{2-} are the active species. (B) Proposed mechanism when Mg^{2+} and SO_4^{2-} are the active species. Reproduced after Zhang et al. [5]

1.1.2.2 Mineral dissolution

Hiorth et al. [33] suggested that injection of the smart water may trigger mineral dissolution will cause the dissolution. Alternatively, a combined precipitation-dissolution process may be considered, as suggested by Madland et al. [34]: precipitation of minerals, such as huntite ($MgCa(CO_3)_4$), magnesite ($MgCO_3$) and anhydrite ($CaSO_4$), from the magnesium and sulfate-rich brine may cause calcite to dissolve in order to balance calcium and carbonate ion concentrations. Polar oil components adsorbed on the dissolved mineral surface are released, exposing the water-wet surface as shown in Figure 1.2.

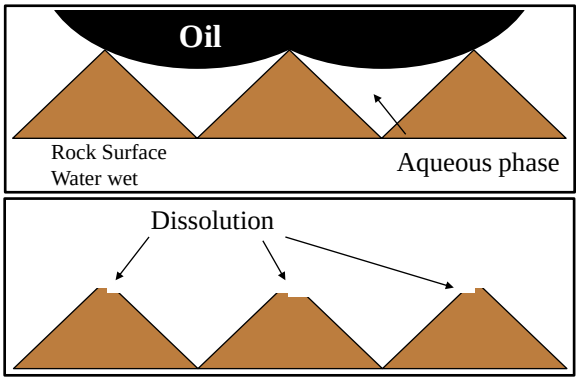

Figure 1.2: Top: A section of the pore space before any dissolution reaction. The surface is rough, and oil is attached where there is a large curvature and the water film is broken. Bottom: Dissolution of the chalk surface has taken place where the oil was attached, and new water-wet rock surface has been created. Reproduced after Hiorth et al. [33]

1.1.2.3 Mineral fines migration

Tang and Morrow [35] observed the fines migration and stripping of oil-wetted particles from rock surfaces in sandstones during LSW. The release of these particles has a double effect; first, it improves the water-wetness of the rock and, second, the mineral fines flowing along an established flow path plug pore throats, increasing the sweep efficiency. Rezaei Doust et al. [15] suggested that diversion of the original flow paths is more important than wettability modification by the fines release. Blocking the pore throats decreases the permeability that can be observed by increasing pressure drop [21, 36, 37].

Possible sources of mineral particles are precipitation of solids from the saturated solution and detachment of the minerals from the rock. Chakravarty et al. [38] suggested that the ion substitution of calcium by magnesium on the carbonate surface can result in significant increase of Ca^{2+} concentration in the brine and trigger precipitation of anhydrite forming mineral fines. Chakravarty et al. [28] speculated that fines interact with crude oil polar components, which results in a formation of the water-soluble stable oil emulsion.

1.1.2.4 Double layer expansion

This mechanism was suggested by Ligthelm et al. [39]. The thickness of the electric double layer between the rock surface and the formation brine is reduced during injection/imbibition of the seawater in a core. This is due to typically large ionic strength of the formation brines resulting in compaction of the counter-ions in the diffuse layer. When the electrolyte concentration in brine is reduced, the screening potential from the ions is lowered, which causes the electrical double layers surrounding the mineral surface and oil droplets to expand. The repulsion force between the surface and droplets increases, which provokes liberation of the oil droplets. The effect is expected to be more pronounced during the LSW.

1.2 Low Salinity Waterflooding (LSW) in Sandstones

The effect of water salinity on the recovery from the clay-bearing sandstone rocks was first reported in the 1960s [40]. However, this effect has not received proper attention in the subsequent years. The effect was later rediscovered by Morrow and co-workers [41-43], whose experiments demonstrated that oil recovery is influenced by the composition of the injected water. Further research in this area revealed the strong effect of brine salinity on the oil recovery [35, 44]. The interest in the low salinity waterflooding has increased drastically in the recent decades, resulting in a significant number of publications.

1.2.1 Conditions for the Low Salinity Effects

Based on the systematic experimental work of the different research groups, Rezaei Doust et al. [15] formulated the following conditions necessary for the low salinity effects in sandstones:

- Porous medium
  - Clay must be present in the formation. A type of the clay may also influence the effect.
- Oil
  - Oil must contain polar components (acid or base). No effects have been observed in experiments with the refined oil.
- Water
  - Initial formation water (FW) must be present.
  - The formation water must contain divalent cations such as Ca^{2+} and Mg^{2+}.
  - Salinity of the injected fluid should be in the range of 1000–2000 ppm.
  - Ionic composition of the injected fluid is important (Ca^{2+} vs Mg^{2+}).
- Production/migration of fines
  - In some cases, fines were produced during the LSW, but the effect of LSW was also demonstrated in the cases where no fines were observed.
- Permeability decrease
  - Pressure drop increased in the most experiments, which may be related to the migration of fines or formation of emulsions.
- Temperature
  - Temperature does not seem to play any clear role. However, the experiments were performed mostly at temperatures below 100°C.

Low salinity effects have been observed both in the secondary and the tertiary recovery modes. The oil recoveries from the two schemes are in general comparable.

1.2.2 Mechanisms of LSW

Though a large amount of experimental data is available to judge on the possible mechanisms behind the low salinity effects in sandstones the full understanding of the process has not been achieved yet. As a result, a large number of possible explanations have been proposed, but none of them has commonly been accepted. Probably, the reason is that the different mechanisms work and interact, and the contribution of each mechanism depends on a particular choice of the crude oil/brine/rock system. Thus, a dominant mechanism may vary from one experiment to another. Below we provide a brief overview on some of the proposed mechanisms.

1.2.2.1 Migration of fines

It was suggested by Tang and Morrow [35] that the decreased salinity of the injected water may affect stability of clays, which may disintegrate due to swelling. Release of clay fragments (fines) will produce the two important effects. First, release of oil-wet fines from the surface will increase its wetness; secondly, fines can migrate and block pore throats, damaging the permeability and diverting the flow.

1.2.2.2 IFT reduction

McGuire et al. [45] proposed that low salinity mechanism may work similarly to alkaline flooding, resulting in the increased pH and reduced interfacial tension (IFT). This is especially valid under high pH conditions, as organic acids in crude oil react to produce in situ surfactant, lowering the IFT. Such conditions are favorable for formation of oil/water or water/oil emulsion, which may improve the sweep efficiency.

1.2.2.3 Multicomponent ion exchange (MIE)

The mechanism of multicomponent ion exchange is based on an assumption that wetting properties of rocks are controlled by the ions that are adsorbed in the core on the clay patches. Lager et al. [24] proposed that divalent cations play a significant role in the interaction between the polar components in the oil and the clay minerals. In the proposed model Ca^{2+} acts as a ”bridge” between the negatively charged clay surface and the carboxylic material. Due to injection of the low salinity water Ca^{2+}–carboxyl complexes gain an ability to desorb from the surface.

1.2.2.4 The salting-in mechanism

This mechanism is an opposite to the known salting-out effect, according to which solubility of the organic material in the presence of salt decreases. Rezaei Doust et al. [15] proposed

that removing salt from the water may have an opposite effect. Therefore, decreasing salinity below a critical ionic strength increases solubility of the organic material in the brine, so that oil recovery is improved.

1.3 Modeling of the Smart Water Effects

The progress in the experimental investigation of the smart water effects demanded a development of an appropriate mathematical model to reproduce the experimental observations and to propose a quantitative description of these effects.

One of the first approaches was developed by Jerauld et al. [46] to describe the low salinity effect. Using the injected brine salinity as a governing parameter, Jerauld et al. performed an interpolation of the relative permeability and the capillary pressure curves as a weighted average of their values for high salinity (HS) and low salinity (LS) waterflooding. The weighting function was calculated according to

$$\theta = \frac{S_{orw} - S_{orw}^{LS}}{S_{orw}^{HS} - S_{orw}^{LS}} \tag{1.1}$$

where S_{orw} is the residual oil saturation for a given salinity, which in turn was linearly interpolated between the low salinity and the high salinity residual oil saturations.

Mahani et al. [47] used a similar approach based on the interpolation of the relative permeabilities. The main difference comes from the shape of the interpolation function; it was suggested that wettability changed abruptly as a threshold value of the mixing factor is achieved. The threshold mixing factor f was defined according to

$$f = \frac{TDS_{FW} - TDS^{*}}{TDS_{FW} - TDS_{LS}} \tag{1.2}$$

Where TDS_{FW} and TDS_{LS} are the salinities of the formation (high salinity) brine and the injected (low salinity) brine, while TDS^{*} is the threshold salinity. The estimated value for f was above 0.9 meaning that very high dilution of the HS formation water was required to induce the wettability alteration. The model was partly capable of reproducing the history of production.

Omekeh et al. [48, 49] introduced the effect of the multicomponent ion exchange to model the low salinity flooding in clay-bearing sandstone rocks. The model accounted for the adsorbed cationic surface species that were in equilibrium with the ions in the bulk solution. Omekeh et al. performed an interpolation of relative permeabilities based on the change in composition of the surface using the weight function H defined as follows:

$$H(\beta_{Ca},\beta_{Mg}) = \frac{1}{1 + r \sum_{i=Ca,Mg} \max(\beta_i^I - \beta_i, 0)} \tag{1.3}$$

where r is the constant determining the shape of the interpolating function, and β_i are the equivalent fractions of the adsorbed species. The model was applied in order to confirm the MIE mechanism and could reproduce some of the experimnetal data.

Dang et al. [50, 51] implemented multicomponent ion exchange in the compositional simulator GEM™, which also included various geochemical interactions and aqueous chemistry, together with the possibility to model the WAG displacement.

Hiorth et al. [52, 53] developed a mathematical model of the calcite surface in equilibrium with an aqueous solution. The model incorporated surface complexation and bulk chemistry. It was demonstrated that the model can be used to predict the surface charge of calcite in brine and the sulfate adsorption on calcite by modeling of the zeta potential data [14] and adsorption data [54]. The simulation results also indicated that variation of the surface charge could not explain the observed oil recovery increase with temperature, as observed under spontaneous seawater imbibition [5, 14], while the correlation between oil recovery and the chalk dissolution demonstrated a good agreement.

Brady et al. [55] developed a surface complexation model to study the equilibrium between a modeled oil, calcite surface and aqueous solution as a function of temperature and brine composition. Based on the performed modeling, it was concluded that the divalent potential determining ions: SO_4^{2-}, Ca^{2+}, and Mg^{2+} reduce electrostatic complexation between the negatively charged carboxyl groups present in the oil and the positively charged surface sites. The study focused on surface complexation and did not consider dissolution and precipitation processes. Nonetheless, the authors claimed a reasonable success in correlating their predictions of complexation to the recovery trends observed in the available body of spontaneous imbibition experiments.

Zaretskiy [56] developed a mathematical model of calcite in equilibrium with an aqueous solution, following the approach introduced by Hiorth et al. [52]. The main difference came from incorporation of a 1D single-phase flow model, which allowed to consider rate-dependent effects. The study successfully reproduced some of the coreflood experiments [5, 32, 57] and showed that both rock dissolution and ion adsorption should be considered in modeling the spontaneous imbibition experiments. Presence of the oil phase was not considered in this study.

1.4 Objectives

The overall objective of this work is to investigate how different mechanisms influence the oil recovery, pressure distribution and composition of the brine during the smart water flooding in oil saturated rocks. Based on the overview of the experimental work, it may be concluded that yet there is no complete understanding of the mechanisms underlying the smart water effects.

A general approach, used for the modeling of EOR processes, involves interpolation of the relative permeability functions and capillary pressure curves based on a governing parameter. A challenge in modeling of the smart water phenomena is that such parameters are difficult to identify, unlike in the conventional chemical waterflooding. As suggested by the different works on the smart water effect in carbonates, both surface complexation and mineral dissolution models could be successfully applied to the same experimental data. Therefore, it is necessary to consider not only ultimate recovery, but also other available experimental data, such as pressure distribution and ion concentrations in the effluent brine. Analysis of the produced brine composition should be performed in order to improve our knowledge of the thermodynamic parameters used to describe the crude oil/brine/rock interactions as in general there is a large uncertainty in such data.

An additional challenge comes from considering the tertiary flooding. It is known that oil trapped in the swept zones inside porous media is present in a form of disconnected oil drops, or oil ganglia. Therefore, the general modeling approach based on interpolation of relative permeability curves should be avoided or used with caution. Considering oil ganglia, it is important to understand the mechanisms that can cause their mobilization and the mechanisms that govern their transport in porous media. The macroscopic theory of multiphase flow assumes that fluid phases flow in their own pore networks and do not influence each other. It is doubtful that the same assumption may be applied for a flow of a single oil ganglion surrounded by water in the pore space. Therefore, an alternative description should be developed.

1.5 Outline

This rest of the thesis is structured as follows. Chapter 2 provides theory necessary for the development of the models of macroscopic multiphase flow in porous media accounting for the geochemical interactions. A specific attention is paid to the surface chemistry of chalks. Description of the numerical methods applied for modeling is given in Chapter 3. We stick to a general formulation of the system of conservation laws and flow equations for the reactive multiphase multicomponent transport applicable in multiple dimensions and describe numerical approaches that are implemented in our modeling. In Chapter 4 we present a study of the mineral dissolution and its possible effects on the waterflooding. The

study focuses on the porosity/permeability alteration due to dissolution and effects of mass transfer on pressure distribution. Chapter 5 presents the development of a micromodel for the two-phase flow on a level of the single pore represented by an angular capillary. In Chapter 6, we present a new formalism to take into account effects that might arise during tertiary waterflooding. We develop a description of the flow of the oil phase consisting of separate oil ganglia that can be mobilized and flow due to wettability alteration. We conclude the Chapter with numerical modeling of a tertiary recovery process to investigate the possible outcomes of the model. In Chapter 7 we revise available experimental data on the single- and two-phase flooding in chalk to understand what physicochemical effect(s) can explain these measurements. We develop a mathematical model that takes into account interaction between carbonate surface and the aqueous solution and perform numerical modeling to of the smart water flooding experiments. The Conclusions and Suggestions for Future Work are given in Chapter 8.

1.6 Publications

The work performed during this Ph.D. study has led to a two publications so far. The work presented in Chapter 4 on the modeling of dissolution effect on waterflooding resulted in the following article:

> Artem Alexeev, Alexander Shapiro, and Kaj Thomsen. Modeling of dissolution effects on waterflooding. *Transport in Porous Media*, 106(3):545–562, 2015.

Part of the work presented in Chapter 5 on the microscopic model for the two-phase flow and Chapter 6 on the mobility of oil ganglia led to a publication of the following article:

> Artem Alexeev, Alexander Shapiro, and Kaj Thomsen. Mathematical Model for Tertiary Recovery by Mobilization of Oil Ganglia. (*Submitted to Transport in Porous Media*)

2

Theory

This chapter covers the standard theory regarding two-phase flow in porous media. The structure of this Chapter is the following. In Section 2.1, we introduce basic concepts that describe crude oil/brine/rock (CBR) system. Next, in Section 2.2, we describe the most important geochemical interactions, relevant to the smart water flooding. In Section 2.3, we describe the Buckley-Leverett model for linear flooding and give an overview on some of the known analytical solutions.

2.1 Wettability

Wettability is defined as a tendency of one fluid to adhere to a solid surface in the presence of other immiscible fluids. As applied to the petroleum industry, it describes a preference of the reservoir rock to be in contact with either water, or oil, or both. This is illustrated in Figure 2.1. It is important to note that wettability only determines the wetting preference of the rock, but does not directly refer to the fluid that is in contact with the rock. Specific crude oil/brine/rock interactions may result in wettability ranging from strongly water-wet to strongly oil-wet. Intermediate (or neutral) wettability corresponds to a case when rock has no strong preference to any of the fluids.

Due to complex nature of the reservoir rocks, they can also develop fractional wettability. The internal surface of the rock is composed of many minerals with different chemical and adsorption properties. Thus, adsorption of crude oil components on some areas of the rock may result in heterogeneous or spotted wettability. Mixed wettability, as introduced by Salathiel [58], is a special case of the fractional wettability in which the oil-wet surfaces form continuous paths through larger pores. It is assumed that in mixed-wet rocks water has a tendency to occupy small pores, which remain water wet while oil occupies larger pores [59]. Wettability is one of the major factors that affects flow and distribution of fluids in porous media. Therefore, it is important to be able to ”measure” wettability and understand the mechanisms that may alter the wetting state of the rock.

A measure of wettability is the contact angle θ, which arises because of the action of the interfacial tension on the interphase boundaries, as illustrated in Figure 2.1b. General characterization of the rock wettability according to Anderson [59] is the following: for a water-wet rock $\theta < 75^{\circ}$, for an oil-wet rock $\theta > 105^{\circ}$, while the range $75^{\circ} < \theta < 105^{\circ}$ corresponds to neutral wet rocks. However, several factors limit the application of contact

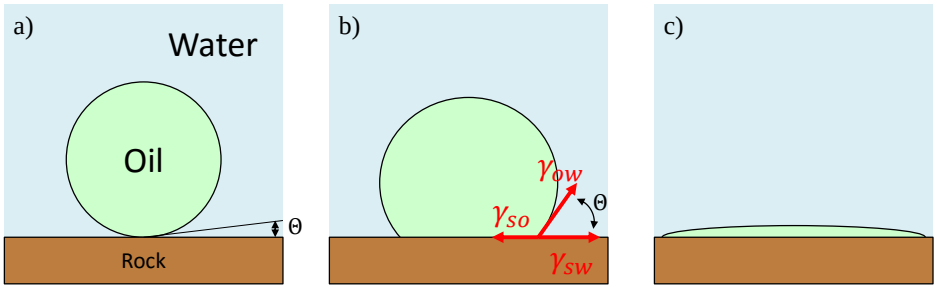

Figure 2.1: Examples of different wettability conditions: a) strongly water-wet; b) water-wet; c) strongly oil-wet. Reproduced after Abdallah et al. [61]

angle measurements to characterize wettability. First, the measurements are usually performed on a smooth surface, and cannot take into account roughness, heterogeneity and complex geometry of the reservoir rocks [60]. Second, the contact angle provides no information about the presence of permanently attached organic material on reservoir rocks. For the mentioned reasons, characterization of wettability of the core with the contact angles is not complete, and other techniques are to be considered.

2.1.1 Capillary pressure

The action of interfacial tension on the interface of the two immiscible liquids results in the pressure difference in the liquids, known as capillary pressure. The capillary pressure is calculated according to the Laplace equation:

$$P_c = P_{non-wetting} - P_{wetting} = \gamma_{ow}\left(\frac{1}{r_1} + \frac{1}{r_2}\right) \tag{2.1}$$

where γ_{ow} is the surface tension, and r_1, r_2 are the principal radii of the surface curvature. For a meniscus inside a cylindrical capillary, which may be considered as a representation of single pore, the capillary pressure is calculated according to the Young-Laplace equation

$$P_c = \frac{2\gamma_{ow}\cos\theta}{r} \tag{2.2}$$

where *r* is the capillary radius.

Considering the capillary pressure difference arising in porous media, one need to take into account the pore size distribution, interfacial tension, wetting conditions, and saturation. However, it turns out that capillary pressure is also determined by the saturation history [59]. This principle is illustrated in Figure 2.2: the three different displacement processes: primary

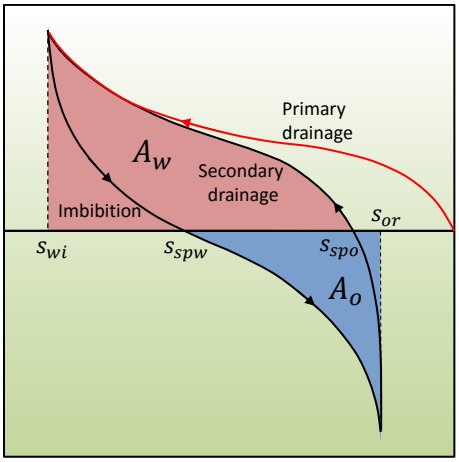

Figure 2.2: Capillary pressure curves. Reproduced after Abdallah et al. (2007) [61].

drainage, imbibition, and secondary drainage are characterized by the three different capillary pressure curves.

Usually, the capillary pressure in porous media is determined in terms of empirical Leverett function $J(s)$ in the form [62]:

$$P_c(s) = \frac{\gamma_{ow} \cdot \cos\theta}{\sqrt{k \,/\, \phi}} \cdot J(s) \tag{2.3}$$

where k is the absolute permeability, ϕ is porosity.

2.1.2 Wettability Characterization

The capillary pressure curves can be obtained experimentally and are utilized to quantify the wettability of the cores. The two most frequently used methods are the Amott-Harvey method and the USBM (United States Bureau of Mines) method [63]. Characterization of wettability according to different procedures is summarized in Table 2.1.

The Ammot-Harvey method combines imbibition and forced displacement to measure the average wettability of the core. It requires calculating the Amott indices of water I_w and oil I_o. The Amott index for water is defined as displacement-by-water ratio: the ratio of water displaced by spontaneous imbibition $V_{wsp} = s_{spw} - s_{wi}$ to the total volume of water displaced during imbibition $V_{wt} = 1 - s_{or} - s_{wi}$. Calculation of Amott index for oil is performed in a similar way, as a displacement-by-oil ratio. The complete Amott-Harvey index WI_{AH} is calculated as follows:

$$\mathrm{WI}_{AH} = I_w - I_o$$
$$I_w = \frac{s_{spw} - s_{wi}}{1 - s_{or} - s_{wi}}, \quad I_o = \frac{s_{or} - s_{spo}}{1 - s_{or} - s_{wi}} \tag{2.4}$$

where s_{spw} is the water saturation for zero capillary pressure during the imbibition process, and s_{spo} is the oil saturation for a zero capillary pressure during the secondary drainage, as shown in Figure 2.2. The Amott-Harvey index changes between +1 for strongly water-wet rocks and −1 for strongly oil-wet rocks. The main shortcoming of this method is its insensitivity close to neural wetting conditions [64]. In addition, there is no standard time allowing spontaneous imbibition to occur (it may proceed for several months) and if the imbibition is stopped after a short period of time, the resulting wettability index will underestimate the water or the oil-wetness of the rock.

Calculation of the USBM index is based on the work required to displace the non-wetting phase. It has been shown that this work is proportional to the area under the capillary pressure curves corresponding to imbibition and drainage [59]. These areas A_w and A_o are marked in Figure 2.2 for a combined Amott/USBM method. According to the procedure, the USBM index WI_{USBM} is calculated as

$$\mathrm{WI}_{USBM} = \ln(A_w \,/\, A_o) \tag{2.5}$$

The USBM wettability index is not bounded and can take any value between $-\infty$ and $+\infty$. Practically, WI_{USBM} is around 0 for neutral wet cores, and ± 1 for strongly water-wet and oil-wet cores correspondingly. The main advantage of the USBM test is its sensitivity near neutral wettability; however, it cannot determine whether a system has a fractional or mixed wettability, while the Amott test is sometimes sensitive to that [59].

Recently Strand et al. [54] proposed a new method to calculate the wettability index of carbonates based on chromatographic separation between sulfate and thiocyanate (SCN^-). Due to adsorption of sulfate on the surface of calcite, production of sulfate in the effluent is delayed compared to SCN^-. This adsorption takes place only on the water-wet pore surface and the fraction area covered by water is assumed to represent the new wettability index:

$$\mathrm{WI}_{New} = \frac{A_{\mathrm{Wett}}}{A_{\mathrm{Heptane}}} \tag{2.6}$$

where A_{Wett} and A_{Heptane} are the calculated areas between the SO_4^{2-} and SCN^- effluent concentration curves for a core in study and a reference core containing heptane, which is assumed to be completely water-wet. The range of this wetting index is from 0 for a completely oil-wet core to 1 for a completely water-wet core. An advantage of this method is good sensitivity of the wetting index in the total wetting range, and, in particular, its

Table 2.1: Approximate relationships between wettability, contact angle and the USBM and Amott-Harvey wettability indexes [65].

	Water-wet	Neutral wet	Oil-wet
θ	$0-75^{\circ}$	$75-105^{\circ}$	$105-180^{\circ}$
WI_{AH}	$0.3 \leq \mathrm{WI} \leq 1.0$	$-0.3 \leq \mathrm{WI} \leq 0.3$	$-1.0 \leq \mathrm{WI} \leq -0.3$
WI_{USBM}	≈ 1	≈ 0	≈ -1
WI_{New}	≈ 1	$\approx 1/2$	≈ 0

sensitivity close to neutral wetting conditions. Additionally, the method is robust as it does not involve long-term imbibition tests.

2.1.3 Effect on Displacement

According to the description given by Craig [66], in a strongly water-wet rock, water occupies smaller pores and forms a thin film covering the entire surface. Oil fills centers of the larger pores. During flooding, oil is displaced from the centers of some pores while in other pores it finds its way along the surface of the rock (e.g. corner filaments). This may result in considerable trapping, by a mechanism known as snap-off [67]. Consider water traveling around the exterior of a pore and bypassing the non-wetting oil phase in the center. On reaching the exit throat of the pore, capillary instability may result in cutting (snapping off) the oil connection in that pore throat. The trapped oil will remain immobile due to the action of capillary forces. The disconnected residual oil is present in the two different forms: (1) small oil drops in the centers of larger pores and (2) larger patches of oil extending over several pores, but disconnected from the effluent [68]. Thus, in strongly water-wet rocks, trapping is controlled by the capillary forces, and most of the trapping occurs immediately after passage of a displacement front. As a result, a large fraction of oil is produced before the water breakthrough, while very little additional oil is produced after the breakthrough [69].

In an oil-wet rock, oil covers the rock surface. During flooding, water flows through the larger pores bypassing the smaller ones. This displacement pattern results in an earlier breakthrough compared to the water-wet rock. Since oil phase remains connected, it can be displaced from the reservoir for a long time. However, efficiency of such displacement is low, since it is required to inject large amounts of water to reach a reasonable recovery. This makes waterflooding in the oil-wet systems less efficient than waterflooding in the water-wet systems [65].

Recovery both from water-wet and oil-wet rocks is challenging, and it is sometimes assumed that intermediate-wet conditions are more favorable for the waterflooding. The neutral wettability is expected to result in less trapping, compared to water-wet conditions and reduce

the tendency of water to bypass oil through large pores compared to oil-wet conditions. However, the real pattern is more complicated and as pointed out by Anderson [69] in some experiments the residual oil saturation was insensitive to the wetting conditions while in other strong water wet conditions resulted in lower residual oil saturation.

2.1.4 Change of Wettability

Most of the clean sedimentary rocks are strongly water-wet. For that reason, historically, it was assumed that water films prevent oil from touching the surface of the reservoir rock [59]. This turned out not to be true, as strong water-wetness can be altered by the adsorption of polar compounds from oil and deposition of organic matter. The surface active agents in oil contain both polar and hydrocarbon ends. When the polar compound is adsorbed, the hydrocarbon end is exposed, making the surface more oil-wet. The adsorption of polar compounds occurs preferentially on the surface of the opposite polarity: acidic compounds are adsorbed on the positively charged surface while basic compounds are adsorbed on the negatively charged surfaces.

Adsorption of polar compounds, which are sufficiently soluble in water, can occur through water films on the surface. Presence of wetting film may reduce but not completely inhibit this adsorption process [59]. Reduction of the water film thickness eventually results in the film rupture allowing oil to contact the rock. The water film is stabilized by the electric forces arising from the electric double layer at the oil/water and water/rock interfaces. Therefore, brine chemistry also affects the wettability of the rock. All the factors, inducing brine pH, salinity, and ionic composition have an effect on the properties of the electric double layer and are expected to affect the adsorption of polar compounds from oil. Specific ions from brine can also adsorb on the surface of the rock. These ions are called the potential determining ions due to their ability to change the surface potential. The potential determining ions for the carbonate surface are SO_4^{2-}, Ca^{2+} and Mg^{2+} [3].

To account for the possible change of wettability during waterflooding, it is important to understand what crude oil/brine/rock interactions occur in the system and what are their potential effects on the waterflooding process on the whole.

2.2 Crude Oil/Brine/Rock Interactions

As it was previously stated, the main difference between conventional flooding and the smart water flooding is that the latter is accompanied by various geochemical and fluid-fluid interactions, including intra-aqueous reactions, mineral dissolution and precipitation, adsorption of ions from the aqueous solution and polar components from oil on the surface of the rock.

2.2.1 Dissolution and Precipitation

Dissolution and precipitation processes are of major importance when considering the brine composition both in the smart water (high/low salinity) and conventional floodings. Even before smart waterflooding was introduced, the quality of water was analyzed in the industry. Precipitation could cause a risk of formation damage and scaling [70].

The effect of dissolution and precipitation was mostly studied in connection with changes of porosity, permeability and mechanical properties of the rock. For smart waterflooding, dissolution and precipitation may also be considered as an internal source/sink for the ions that contribute to the smart water effect.

Primary minerals comprising carbonate rocks are calcite and dolomite. Other important minerals are gypsum (at low temperatures) and anhydrite (at high temperatures), because Ca^{2+} and SO_4^{2-} are readily present in seawater.

2.2.1.1 Calcite

Calcite can dissolve according to the following dissolution equilibrium reaction

$$\mathrm{CaCO_3} \rightleftarrows \mathrm{Ca^{2+}} + \mathrm{CO_3^{2-}} \tag{2.7}$$

This equation describes the dissolution process in distilled water in the absence of carbon dioxide. However, a complete picture of calcite dissolution is more complicated, since one need to account for proper aqueous chemistry. The overall dissolution reaction, in this case, can be represented by

$$\mathrm{CaCO_3} + \mathrm{H_2O} + \mathrm{CO_2(g)} \rightleftarrows \mathrm{Ca^{2+}} + 2\mathrm{HCO_3^{2-}} \tag{2.8}$$

Equation (2.8) reflects the relation between the carbon dioxide and the calcite dissolution. Plummer et al. [71] developed a rate model for calcite dissolution based on three mechanisms of the dissolution reaction:

$$r_{calcite} = \underbrace{k_1[\mathrm{H^+}] + k_2[\mathrm{H_2CO_3}] + k_3[\mathrm{H_2O}]}_{r_f} - \underbrace{k_4[\mathrm{Ca^{2+}}][\mathrm{HCO_3^-}]}_{r_b} \tag{2.9}$$

where $r_{calcite}$ is the specific rate of calcite dissolution, [...] represent the activities of aqueous species and $k_i = k_i(T)$, are the rate constants fitted to experimental data. The effect of the first term is significant only at pH values lower than 3.5. While k_1, k_3 do not vary significantly is the range of temperatures used for smart water experiments, k_2 and k_4 increase significantly with temperature [72], and the corresponding terms in the kinetic equations are the most important in determining the rate of dissolution. The value $[\mathrm{H_2CO_3}]$ represents the activity of $\mathrm{CO_2}(aq)$ and is related to the carbon dioxide pressure. Thus, carbon

dioxide controls the calcite equilibria. Pokrovsky et al. [73], proposed the following polynomial empirical relation to estimate the calcite dissolution rate:

$$\log r_f = A + B \cdot P_{CO_2} + C \cdot (P_{CO_2})^2 \tag{2.10}$$

where P_{CO_2} is the carbon dioxide pressure and *A*, *B* and *C* are the temperature dependent parameters calculated from fitting the experimental data.

2.2.1.2 Dolomite

The following reaction describes the dissolution of dolomite in water:

$$CaMg(CO_3)_2 + 2CO_2(g) + 2H_2O \rightleftarrows Ca^{2+} + Mg^{2+} + 4HCO_3^- \tag{2.11}$$

Similarly to calcite, the pressure of carbon dioxide controls the process of dolomite dissolution. The dissolution rate of dolomite is an order of magnitude lower than the dissolution rate of calcite [72] and it is not expected to have any influence on the short-lasting waterflooding experiments.

2.2.1.3 Anhydrite

As mentioned earlier, formation of anhydrite may occur under seawater injection into a reservoir, especially at elevated temperatures. The reason is that solubility of anhydrite drastically decreases with temperature, as shown in Figure 2.3. The following reaction describes the anhydrite dissolution/precipitation process:

$$CaSO_4 \rightleftarrows Ca^{2+} + SO_4^{2-} \tag{2.12}$$

One should expect that increasing the temperature may result in anhydrite precipitation that will lower the concentrations of Ca^{2+} and SO_4^{2-}. Vice versa, during injection of a low salinity brine, one should expect anhydrite dissolution to occur and increase the concentrations of Ca^{2+} and SO_4^{2-}.

The rate of anhydrite precipitation is a difficult parameter to determine. A primary difference between calcite and anhydrite is their distribution within the porous media. Calcite is abundant, whereas anhydrite is not always present. Formation of a crystal starts with a nucleation, which is delayed by the so-called induction time dependent on the thermodynamic conditions [74]. Thus, concerning precipitation of anhydrite in a core or a reservoir it is hard to determine when and where it will start.

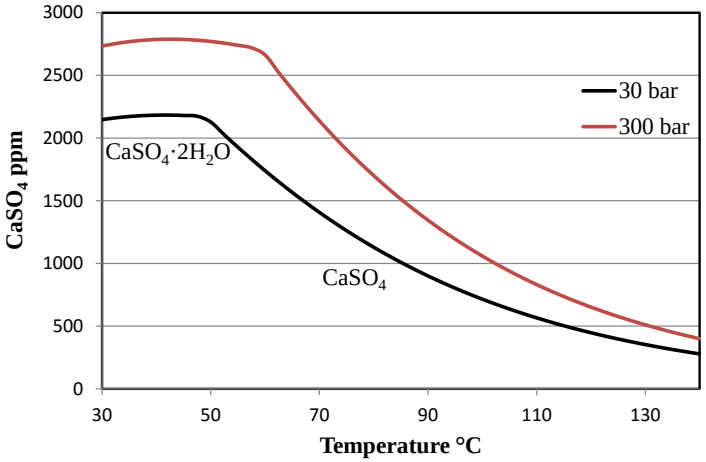

Figure 2.3: Solubility of $CaSO_4$ as a function of temperature at pressure of 30 bar (black) and 300 bar (red) according to Extended UNIQUAC model.

2.2.1.4 Rates of Non-Equilibrium Reactions

The following expression is usually applied to calculate the rate of mineral dissolution and precipitation reactions [75]:

$$\dot{r} = k_r \hat{A}(1 - \mathrm{SI})^n \tag{2.13}$$

Here k is the rate constant, $\hat{A}$ is the reactive specific surface area, SI is the saturation index $\mathrm{SI} = IAP/K^{sp}$, IAP stands for the ion activity product and K^{sp} is the solubility product, n is the parameter that is fitted in order to match the observed rates. These parameters are not unique as they indirectly include the effects of surface heterogeneity and competition between the convective and diffusive transport [75].

Alternatively, the rate law for the mineral dissolution/precipitation reaction may be determined in the same way as it was introduced for the calcite dissolution in (2.9):

$$\dot{r} = \hat{A}(k_f \cdot IAP^{+} - k_b \cdot IAP^{-})^n \tag{2.14}$$

Where k_f and k_b are the forward and backward reaction rate constants respectively. Consider the mineral reaction represented by

$$\sum_{a=1}^{n_{sp}} \nu_a \mathrm{X}_a = 0 \tag{2.15}$$

where ν_a are the stoichiometric coefficients for the species X_a. The stoichiometric coefficients are such that $\nu_a < 0$ for the reactants, and $\nu_a > 0$ for the products. Then the ion activity products are calculated as follows:

$$IAP^+ = \prod_{\nu_a<0}^{n_{sp}} [\mathrm{X}_a]^{\nu_a}, \quad IAP^- = \prod_{\nu_a>0}^{n_{sp}} [\mathrm{X}_a]^{\nu_a}$$
$$IAP = IAP^- \,/\, IAP^+ \tag{2.16}$$

The rate constant k used in equations (2.13) and k_f in equation (2.15) are not necessarily the same. In fact, the parameters used in (2.13), (2.15) may not be considered as tabulated constants. Most of the studies on the mineral dissolution rates are performed using the bulk powder experiments, and a large variation in the rate constants is observed in different experiments, especially where the different measurement techniques are applied [76].

2.2.2 Sorption

It is important to consider sorption of aqueous species on the surface of the rock. Due to large surface area and, usually, high reactivity of the surface, it can adsorb considerable amounts of the substances [77]. Below we consider several important models of sorption and ion exchange that find its application in the modeling of the smart water flooding.

2.2.2.1 Henry adsorption isotherm

The linear Henry adsorption isotherm is one of the most widely applied models in environmental geochemistry to predict sorption. It is also known as the distribution coefficient approach [75]. This sorption model is based on the assumption that the ratio of the sorbed to the dissolved mass of the component is determined by the Henry adsorption constant (or the distribution coefficient):

$$K_d = c^* \,/\, c \tag{2.17}$$

where c^* is the concentration per bulk volume in mol/l(core), c is the concentration in solution in mol/l(fluid), the distribution coefficient K_d is dimensionless.

The main disadvantage of this model is that it does not take into account the limited number of sorbing sites on the surface. This allows the solute to adsorb without limits and without being affected by the sorption of other species. For the mentioned reasons, the approach is broadly recognized to describe poorly the behavior of ionic species [78] and is mainly used for uncharged, weakly sorbing molecules [79]. Equation (2.17) is conventionally written in the form:

$$c^* = K_d \cdot c \tag{2.18}$$

2.2.2.2 Langmuir isotherms

The Langmuir model provides an improvement over the Henry model by maintaining the mole balance on the sorbing sites [80]. Since the number of sites in this model is limited, the species cannot adsorb in the infinite amounts. A model known as the competitive Langmuir sorption accounts for the competition of different species if more than one species can adsorb on the same surface sites.

Two parameters required by the Langmuir model are the equilibrium constants K and the sorption capacity (or exchange capacity) T_s, which is the maximum number of moles of adsorbed species per unit surface. Consider an equilibrium sorption reaction of the form

$$\mathrm{X} + \mathrm{A} \rightleftarrows \mathrm{XA} \tag{2.19}$$

where X stands for the surface site, A for the aqueous species, and XA for the occupied site. The mass action law reads

$$K = \frac{[\mathrm{XA}]}{[\mathrm{X}][\mathrm{A}]} \tag{2.20}$$

The sorption capacity is equal to the sum of surface species concentrations σ in $\mathrm{mol/m^2}$:

$$T_s = \sigma_X + \sigma_A \tag{2.21}$$

where we write σ_A instead of σ_{XA}. The activity coefficients for the surface species are equal to one so that $[\mathrm{X}] = \sigma_X$, $[\mathrm{XA}] = \sigma_A$. Combining (2.20) and (2.21) one obtain the Langmuir adsorption isotherm in the form:

$$\sigma_A = T_s \frac{K[\mathrm{A}]}{1 + K[\mathrm{A}]} \tag{2.22}$$

Surface fractions $\beta = \sigma / T_s$ may be used instead of the surface concentrations. For the competitive Langmuir adsorption, equation (2.22) is generalized according to:

$$\beta_A = \frac{\sigma_A}{T_s} =_s \frac{K_a[\mathrm{A}_a]}{1 + \sum_a K_a[\mathrm{A}_a]} \tag{2.23}$$

where the summation is performed over all species that can adsorb on the same surface sites.

2.2.2.3 Multicomponent ion exchange

The ion exchange model is commonly applied in geochemistry to describe the interaction of cationic species with clay minerals [75]. As can be understood from the name, the model does not treat the sorption and desorption of species, but replacement of one ion by another. The following equation represents a general substitution reaction on the surface

$$a\mathrm{X}_b\mathrm{B} + b\mathrm{A}^{a+} \rightleftarrows b\mathrm{X}_a\mathrm{A} + a\mathrm{B}^{b+} \tag{2.24}$$

where a and b are the valence of cations A and B respectively (commonly 1 or 2). Equation (2.24) implies that substitution on the surface occurs without changing the surface charge. Cation B occupies b sites while cation A occupies a sites. Therefore, in this model the condition for the limited number of sites is imposed on the equivalents $z_a\sigma_a$:

$$a\sigma_A + b\sigma_B = CEC \tag{2.25}$$

where CEC is the cation exchange capcity. It is important to point out that $\mathrm{X_bB}$ and $\mathrm{X_aA}$ do not represent real chemical species, therefore the particular form of equation (2.24) may vary depending on the convention used. Equation (2.24) is written according to the Gaines-Thomas convention [72]. The equilibrium condition for the reaction (2.24) reads

$$K^{GT} = \frac{(\beta_A^{GT})^b[\mathrm{B}]^a}{(\beta_B^{GT})^a[\mathrm{A}]^b} \tag{2.26}$$

where $\beta^{GT} = z_a\sigma_a/CEC$ represents the equivalent fractions. Equation (2.26) is supplemented with the requirement that the sum of equivalent fraction of surface species is one:

$$\beta_A^{GT} + \beta_B^{GT} = 1 \tag{2.27}$$

Generalization to a larger number of exchanging species is straightforward. Commonly the valence of the ions in consideration is 1 or 2, and it is possible to solve the above equations explicitly.

The main disadvantage of the ion exchange model is that it does not take into account the properties of the brine in contact with the surface. This requires different equilibrium constants K^{GT} to be used for the brines with the different ionic strengths. Also, the cation exchange capacity is known to vary with pH due to surface sites protonation/deprotonation reactions [81] which is no taken into account by the model.

2.2.3 Surface Complexation

The adsorption models described above may be too simplistic to mimic the interaction between the aqueous solution and the surface. The main disadvantage is that none of them takes into account the electric state of the surface, which is known to vary considerably with pH, ionic strength and ionic composition [82]. The application of the above models requires determining the equilibrium constants for specific conditions, unique for a given combination of rock and a fluid. A more general approach allowing to overcome these limitations is introduced by the surface complexation models [79, 80]. These models consider adsorption on the surface together with the formation of the electric double layer (EDL) [83], which is briefly introduced below.

At the interface between a charged surface and a solution electric potential is developed. The theory of double layer [79, 82] refers to two parallel layers surrounding the surface as illustrated in Figure 2.4. The first layer, known as the Stern layer, is comprised of the ions that are adsorbed on the surface and are fixed. In this layer, with a typical thickness of 1 nm, the major part of the potential drop occurs [84]. The second layer, a diffuse layer, has a thickness between 1 to 500 nm depending on the surface charge and the ionic strength of the solution. The ions in this layer are attracted to the surface via the Coulomb force. They are loosely associated with the surface and can move in the fluid under the influence of thermal motion and electric attraction. The ions with the charge of the opposite sign to those of the surface are attracted to the surface while the ions with the similar charge are repelled. This results in the screening of the surface charge. The diffuse layer is split into two separate regions based on the ability of ions to move (slip) along the surface:

(I) The region between the Stern plane and slipping plane. Ions are not affected by the tangential stress arising due to the flow of water along the surface.

(II) The region between slipping plane and the bulk fluid. Ions can move under the influence of tangential stress, meaning the flow of water affects the distribution of ions in this layer.

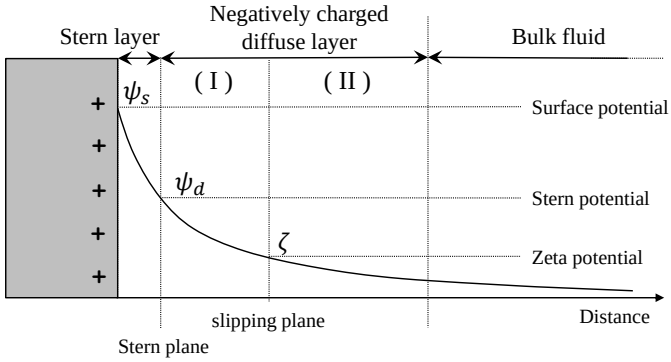

Figure 2.4: Illustration of the EDL structure and electric potential for a positively charged surface.

The value of the surface potential at the slipping plane is called Zeta potential.

It is also possible that more than one type of the sorbing sites is present on a single surface. On the calcite surface, two surface complexes with opposite charges: $>\mathrm{CaOH_2^+}$ and $>\mathrm{CO_3^-}$ are present in equal numbers [33]. If this surface is brought in contact with an aqueous solution containing the potential determining ions, the following exchange reactions are to be considered [55]:

$$\begin{aligned}
&(1)\quad >\mathrm{CO_3^-} + \mathrm{Mg^{2+}} \rightleftarrows >\mathrm{CO_3Mg^+}\\
&(2)\quad >\mathrm{CO_3^-} + \mathrm{Ca^{2+}} \rightleftarrows >\mathrm{CO_3Ca^+}\\
&(3)\quad >\mathrm{CaOH_2^+} + \mathrm{SO_4^{2-}} \rightleftarrows >\mathrm{CaSO_4^-} + \mathrm{H_2O}\\
&(4)\quad >\mathrm{CaOH^{2+}} \rightleftarrows >\mathrm{CaOH^0} + \mathrm{H^+}\\
&(5)\quad >\mathrm{CaOH_2^+} + \mathrm{HCO_3^-} \rightleftarrows >\mathrm{CaHCO_3^0} + \mathrm{H_2O}\\
&(6)\quad >\mathrm{CaOH_2^+} + \mathrm{CO_3^{2-}} \rightleftarrows >\mathrm{CaCO_3^-} + \mathrm{H_2O}\\
&(7)\quad >\mathrm{CO_3^-} + \mathrm{H^+} \rightleftarrows >\mathrm{CO_3H^0}
\end{aligned} \tag{2.28}$$

Each of these reactions has a corresponding mass-action equation. For example, consider the third reaction (2.28); the mass action equation reads:

$$K_3 = \frac{[>\mathrm{CaSO_4^-}]}{[>\mathrm{CaOH_2^+}][\mathrm{SO_4^{2-}}]\exp(2\mathcal{F}\psi_s \,/\, RT)} \tag{2.29}$$

where ψ_s is the surface potential, $\mathcal{F}$ is the Faraday constant, R is the universal gas constant and T is the absolute temperature. Introduction of the electrostatic term in equation (2.29) is explained by the dependence of aqueous specie activities on the surface potential. If the surface potential has a positive sign then negatively charged species, such as sulfate, will have a higher activity close to the surface and vice versa. The activity coefficient for the surface complexes is taken to be one. Similarly to Langmuir isotherms, the activities can be expressed in terms of either surface concentrations or surface fractions.

The surface potential is determined by the surface charge density δ^s , which is calculated as a combined charge of all the surface complexes:

$$\delta_s = \mathcal{F}\sum_{a_s} z_{a_s}\sigma_{a_s} \tag{2.30}$$

where z_{a_s} is the charge of the surface complex. The surface potential is calculated using the Gouy-Chapman theory [75, 82]:

$$\delta_s = \sqrt{8\varepsilon\varepsilon_0 RT\cdot I\times 10^3}\,\sinh\left(\frac{\mathcal{F}\psi_s}{2RT}\right) \tag{2.31}$$

where ε is the dielectric constant of water, ε_0 is the permittivity of free space and I is the (molal) ionic strength. Equation (2.31) is approximate as it was originally derived for a single symmetrical electrolyte, rather than for a mixed solution. A more accurate calculation of the surface potential can be performed with the Grahame equation [82].

The main advantage of the surface complexation model is its ability to account for:

- Electrostatic interaction between the aqueous ions and charged surface by introducing the electrostatic term $\chi = \exp(\mathcal{F}\psi_s/RT)$.
- Variation of the ionic strength, due to the dependence of surface potential on surface charge and ionic strength according to the equation (2.31).
- Variation of pH due to reactions (4) and (7) in (2.28).

Surface complexation models provide a bridge between the macro-scale surface charging, sorption properties of carbonate minerals, and the chemical structure of the surface sites. However, the double layer models suffer from uncertainties and data limitations. Values reported for the equilibrium constants and site densities can vary over a relatively broad range [33, 73].

As it was already discussed above, the wetting state of the rock depends on the presence and stability of the water films that prevent polar compounds in oil to adsorb on the surface. The stability and properties of the water films are related to the structure of the EDL. Therefore, surface complexation models can be used to provide a description of the change of the wetting properties of rocks during the smart water flooding.

2.3 The Buckley-Leverett Model

The Buckley-Leverett model was originally introduced to describe two-phase immiscible displacement in porous media [85]. It serves as a basis for the development of a mathematical model for any kind of liquid-liquid displacement in porous media. The original model was later extended and widely applied for the various types of waterflooding of petroleum reservoirs, including polymer flooding, carbonated waterflooding, miscible flooding, steam flooding, and various type of surfactant flooding (see [86] and references therein).

2.3.1 Basics

Consider the flow of immiscible fluids in porous media. The Buckley-Leverett approach is based on the macroscopic approximation of the mechanics of continuous medium, according to which fluid phases: water (subscript w) and oil (o), together with porous matrix, are all situated at the same macroscopic representative elementary volume (r.e.v.). From the microscopic point of view, each r.e.v. contains a large number of pores and should in general be characterized by complex pore geometry and different fluid distributions within it. The

state of each macroscopic point (volume element) is characterized by amounts of each phase, expressed in volumetric fractions. The volumetric fraction of the space accessible for fluids is porosity ϕ, the fractions of the pore space occupied by water and oil are saturations: $s_w = s$ and $s_o = 1 - s$ respectively.

The superficial flow velocities of the phases are introduced as the rates of flow per unit surface area. The velocities of water and oil are denoted by $\vec{u}_w$ and $\vec{u}_o$ respectively. The total flow velocity $\vec{u}_t$ is the sum of the phase flow velocities:

$$\vec{u}_t = \vec{u}_w + \vec{u}_o \tag{2.32}$$

The following equations express the mass conservation laws for the phases:

$$\partial_t(\rho_w \phi s_w) + \nabla \cdot (\rho_w \vec{u}_w) = 0 \tag{2.33}$$

$$\partial_t(\rho_o \phi s_o) + \nabla \cdot (\rho_o \vec{u}_o) = 0 \tag{2.34}$$

where ρ_w and ρ_o are the densities of water and oil phases, respectively.

2.3.2 Relative Permeabilities

In the macroscopic theory, it is assumed that each phase occupies its own pore system, and thus the flow of one fluid does not affect another. It may also be interpreted as if the viscous friction forces act only between the fluid phase and the porous matrix, but not between two fluid phases. Generalized Darcy laws relate the phase velocities $\vec{u}_w$, $\vec{u}_o$ and the forces driving the flow of the phasess by means of relative phase permeabilities $k_{rw}(s)$ and $k_{ro}(s)$.

$$\vec{u}_w = -\frac{k \cdot k_{rw}(s)}{\mu_w} \cdot (\nabla P_w - \rho_w \vec{g}) \tag{2.35}$$

$$\vec{u}_o = -\frac{k \cdot k_{ro}(s)}{\mu_o} \cdot (\nabla P_o - \rho_o \vec{g}) \tag{2.36}$$

where k is the absolute permeability, μ_w and μ_o are the oil and water viscosities, P_w and P_o are the pressures in the phases and $\vec{g}$ is the gravitational acceleration. The form of equations (2.35), (2.36) assumes the isotropy of the absolute permeability. In a more general case, the scalar absolute permeability should be replaced with the permeability tensor **k**. It is also convenient to introduce phase mobilities:

$$\lambda_\alpha = \frac{k_{r\alpha}}{\mu_\alpha}, \quad \alpha = w, o \tag{2.37}$$

Using the concept of phase mobilities, equations (2.35), (2.36) assume the form

$$\vec{u}_\alpha = -k \cdot \lambda_\alpha (\nabla P_\alpha - \rho_\alpha \vec{g}), \quad \alpha = w, o \tag{2.38}$$

There is no general way to calculate the phase relative permeabilities without conducting core flood experiments. Moreover, experiments on steady two-phase flow, required for the direct measurement of phase relative permeabilities, are laborious. In case direct measurements cannot be carried out, suitable approximations determine the relative permeability functions. One of the most widely applied models for the relative permeability functions is the Corey exponent representation [70, 87, 88]:

$$k_{rw} = k_{rwor} \left(\frac{s - s_{wi}}{1 - s_{wi} - s_{or}} \right)^{n_w} \tag{2.39}$$

$$k_{ro} = k_{rowi} \left(\frac{1 - s_{or} - s}{1 - s_{wi} - s_{or}} \right)^{n_o} \tag{2.40}$$

where s_{wi} and s_{or} are the irreducible water saturation and residual oil saturation respectively, k_{rowi} and k_{rwor} are the end point permeabilities and n_w, n_o are the Corey exponents. These parameters can be recovered by indirect experimental procedures such as Welge's or JBN methods [89, 90], involving certain manipulations with the experimental data from the flooding experiments. The typical shapes of the relative permeability curves corresponding to water-wet and oil-wet rocks are shown in Figure 2.5. The rule of thumb for the characteristic values of Corey parameters for a water-wet system is [91]:

- Endpoint saturations: s_{or} around 0.3 and higher; s_{wi} around 0.1.
- Corey exponents: n_o around 2 to 3; n_w around 4 to 6.
- End point relative permeabilities: k_{rowi} around 0.6 to 0.8; k_{rwor} around 0.1 to 0.4.

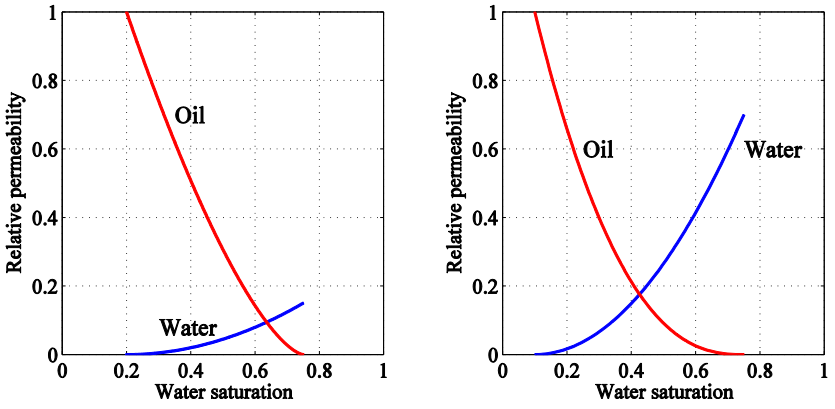

Figure 2.5: Typical oil/water relative permeability curves: (Left) strongly water-wet rock, (Right) strongly oil-wet rock. Reproduced after Craig [66].

For an oil-wet system, water and oil exchange places. The residual oil saturation of an oil-wet rock may be very low, however, due to high value of the Corey exponent (n_o around 4 to 6) the relative permeability of oil diminishes quickly with increasing water saturation.

A central concept for the Buckley-Leverett model is the fractional flow function $f_w(s)$ which is equal to the ratio of the mobility of water to the sum of the mobilities of water and oil:

$$f_w = \frac{\lambda_w}{\lambda_w + \lambda_o} = \frac{k_{rw} \,/\, \mu_w}{k_{rw} \,/\, \mu_w + k_{ro} \,/\, \mu_o} \tag{2.41}$$

The physical meaning of the fractional flow function is the volumetric fraction of water in the flow.

2.3.3 Transport of Chemicals

The scheme presented above is extended to describe displacement of oil by an aqueous chemical solution. A chemical substance such as a polymer or a surfactant is added to the injected water to improve the flooding efficiency. It is usually assumed that concentration of the chemical is relatively low and does not affect the densities [92].

The material balance equation for transport of the chemical is given by [93]

$$\partial_t(\phi s c) + \nabla \cdot (c\vec{u}_w - \mathbf{D}_w \cdot \nabla c) = -\partial_t c^* \tag{2.42}$$

where c is the concentration of the chemical in the solution, $\mathbf{D}_w$ is the diffusion/dispersion tensor, and the term in the right hand side of the equation represents the loss of chemical due to brine-rock interactions. The asterisk (*) is used to denote the difference between the aqueous concentrations c in mol/l(water) and losses c^* in mol/l(core).

2.3.4 Analytical Solutions for Linear Waterflooding

Below we present the original Buckley-Leverett solution, as well as the two important cases of the chemical flooding. These cases include secondary and tertiary waterflooding, to illustrate the general features of these classical solutions. The 1D Buckley-Leverett problem is usually associated with a displacement of oil by water from a horizontal reservoir developed by parallel lines of injection and production wells. The major assumptions behind the considered models are [86]:

- One dimensional flow in homogeneous, isotropic, isothermal porous medium.
- Fluids are incompressible.
- Gravity and capillary forces are negligible.
- The initial distribution of fluids is uniform.

Additional assumptions for the chemical flooding are:

- Local chemical equilibrium exists.
- The adsorption isotherm is a convex or linear function.
- Dispersion is negligible.
- The chemical cannot be dissolved in oil.

For the flow of incompressible fluids, combination of equations (2.33), (2.34) governing the flow of phases results in the incompressibility condition for the total flux:

$$\nabla \cdot \vec{u}_t = 0 \tag{2.43}$$

For the linear flood, equation (2.43) states the invariance of the overall flow velocity over distance: $u_t = u_t(t)$. In this case, pressure can be eliminated from the phase material balance equations. Under assumptions listed above, combining (2.32), (2.38), and (2.41) it may be obtained that:

$$u_w = f_w u_t, \quad u_o = (1 - f_w)u_t \tag{2.44}$$

Substitution of these velocities in the phase mass balance equations (2.33) and (2.34) results in the identical form of both equations:

$$\phi \partial_t s + u_t \partial_x f_w = 0 \tag{2.45}$$

Equation (2.45) is known as the Buckley-Leverett equation. It is a quasi-linear first-order hyperbolic equations in the unknown $s(t, x)$.

Consider now transport of the chemical. Under assumption about local chemical equilibrium $c^* = c^*(c)$, neglecting diffusion and using (2.44), the material balance equation for the chemical reads:

$$\partial_t(\phi s c + c^*(c)) + \partial_x(f_w c) = 0 \tag{2.46}$$

Equation (2.46) can be combined with the Buckley-Leverett equation (2.45) to obtain

$$(\phi s + (c^*)')\partial_t c + u_t f_w \partial_x c = 0 \tag{2.47}$$

For the original Buckley-Leverett problem, equation (2.45) is considered first to obtain the solution for water saturation. The solution for the tracer is obtained afterwards by solving (2.47). For chemical flooding, both equations are to be solved simultaneously, since the fractional flow function depends on both s and c. The governing system of equations (2.45), (2.47) is to be supplemented with initial and boundary condition that are discussed in corresponding sections.

The following transformation of variables is conventionally applied to bring the equations (2.45), (2.47) to dimensionless form

$$x_D = \frac{x}{L}, \qquad t_D = \frac{1}{\phi L}\int_0^t u_t(\tau)d\tau \tag{2.48}$$

where $U(\tau)$ is the linear velocity corresponding to a given injection rate. The newly defined time t_D correspond to the amount of pore volumes injected. Substitution in (2.45), (2.47) results in the following dimensionless system of equations:

$$\partial_{t_D} s + \partial_{x_D} f_w = 0 \tag{2.49}$$

$$(s + \phi^{-1}(c^*)')\partial_{t_D} c + f_w \partial_{x_D} c = 0 \tag{2.50}$$

2.3.4.1 The Buckley-Leverett solution

The conventional Buckley-Leverett solution is obtained for the problem of 1D waterflooding, which is described by a single equation (2.49). The boundary and initial conditions correspond to the injection of water in porous medium at irreducible water saturation:

$$s(0, x_D) = s_{wi}, \quad s(t_D, 0) = 1 - s_{or} \tag{2.51}$$

The chemical is assumed not to participate in any interactions, and $c^* = 0$. Therefore, the chemical is considered to be a tracer that is present only in the injected water with the molar concentration c^J. The corresponding initial and boundary conditions assume the form:

$$c(0, x_D) = 0, \quad c(t_D, 0) = c^J \tag{2.52}$$

The Buckley-Leverett solution for the problem (2.49) to (2.52) is shown in Figure 2.6. It consists of the three main parts [88, 92]:

1. Displacement front ($x = x_{wf}$). Saturation at the displacement front changes jumpwise from initial water saturation s_{wi} to s_f. The position of the displacement front can be determined from $x_{wf} = \xi_f t_D$, where ξ_f is the front velocity.
2. A region ahead of the displacement front ($x > x_{wf}$). Saturation is equal to the irreducible water saturation $s = s_{wi}$, and only oil is mobile.
3. A region behind the displacement front ($x < x_{wf}$). Both oil and water are mobile. The saturation is determined according to the following equation [92]:

$$f_w'(s) = \xi, \qquad \xi = x_D \,/\, t_D \tag{2.53}$$

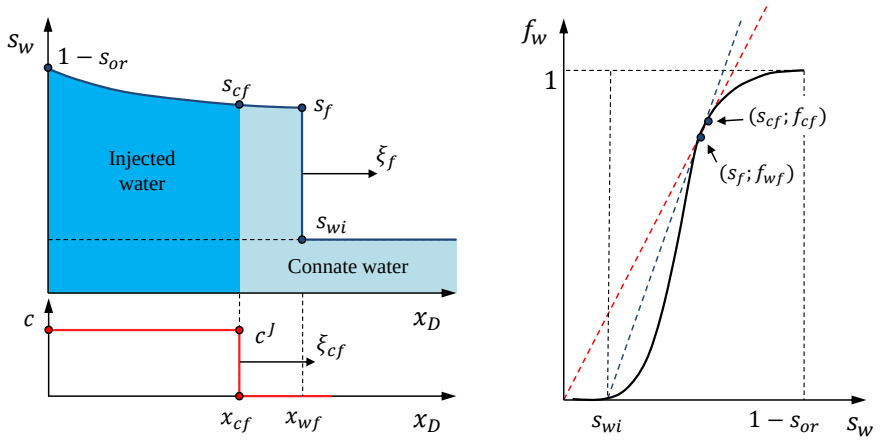

Figure 2.6: a) Saturation profile for the original Buckley-Leverett solution and concentration profile for the tracer. b) Fractional flow function.

The velocity of the displacement front is determined using the Rankine-Hugoniot condition [94]:

$$[\![f_w]\!] = \xi_f [\![s_w]\!] \tag{2.54}$$

where $[\![s]\!] = s^+ - s^-$ represent a jump in the value at the front. In order to determine the velocity of the displacement front, condition (2.54) is combined with (2.53) to obtain

$$f_w'(s_f) = \frac{f_w(s_f)}{s_f - s_{wi}} \tag{2.55}$$

The above equation allows to determine saturation at the front s_f, which is then used to calculate the displacement front velocity according to equation (2.54). Equations (2.54) and (2.55) allow a simple geometric interpretation on the plane of variables (s, f): velocity of the displacement front is determined by the tangent line to the fractional flow curve drawn from the point $(s_{wi}; 0)$ as shown in Figure 2.6b. More generally, a part of the solution corresponding to a shock is represented by a line on the (s, f) plane connecting two points (s_0, f_0) and (s_1, f_1). The velocity of the corresponding shock is determined by the Rankine-Hugoniot condition:

$$\xi_{12} = \frac{[\![f]\!]}{[\![s]\!]} = \frac{f_0 - f_1}{s_0 - s_1} \tag{2.56}$$

Solution for the tracer is described in a similar manner:

1. The concentration front ($x = x_{cf}$). Concentration at the front changes jumpwise from 0 (in the connate water) to c^J in the injected water. Position of the displacement front can be determined from $x_{cf} = \xi_{cf} t_D$, where ξ_{cf} is the front velocity.
2. Region with connate water ($x > x_{cf}$). Concentration of the tracer is 0.
3. Region with injected water ($x < x_{cf}$). Concentration of the tracer is equal to c^J.

The Rankine–Hugoniot condition is used to determine the velocity of the concentration front, similar to (2.54), (2.55):

$$f_w'(s_{cf}) = \frac{[\![f_w c]\!]}{[\![s_w c]\!]} = \frac{f_w(s_{cf})}{s_{cf}}, \quad \xi_{cf} = f_w'(s_{cf}) \tag{2.57}$$

Equation (2.57) allows simple geometric interpretation: velocity of the concentration front is determined by the tangent line to the fractional flow curve drawn from the point $(0; 0)$ as shown in Figure 2.6b.

The presented solution implies that in the absence of diffusion the injected brine does not mix with the formation water, which was also observed experimentally [95]. This means that displacement of oil is performed by the connate water bank rather than the injected water.

2.3.4.2 Chemical flooding

Under chemical flooding, a chemical like a polymer [96] or a surfactant [97, 98] are added to the injected water in order to improve the flooding efficiency. Effects of these chemicals are different: the polymer decreases water mobility by increasing its viscosity, while the surfactant reduces the interfacial tension (IFT). Reduction of the IFT allows to untrap oil, reducing the residual oil saturation. Physicochemical behavior of the injected chemical solutions is different in the two cases. However, its mathematical description in the framework of the fractional flow analysis is similar, and we do not specify the particular type of chemical.

The effect of chemical injection is introduced in the Buckley-Leverett model by an additional dependence of the fractional flow function on the concentration of the chemical $f_w = f_w(s, c)$. An assumption about the convex or linear shape of the adsorption isotherm results in dependence of the solution only on the fractional flow functions for the formation water $f_w(s, 0)$ and injected water $f_w(s, c^J)$ [92], while intermediate values $f_w(s, c)$ are not required. We introduce an additional simplification related to the particular form of the sorption isotherm $c^* = c^*(c)$ and consider the Henry adsorption isotherm of the form (2.18):

$$c^* = \phi \Gamma c \tag{2.58}$$

where Γ is constant and porosity ϕ is introduced to simplify notations. Analytical solutions for more complex sorption isotherms considering one or several species in the injected water can be found in the literature [86, 92]. For our purposes it is sufficient to illustrate the effect of chemical flooding based on the simple model (2.58). Solutions presented below do not cover all the possible analytical solutions of the Buckley-Leverett model for the chemical flooding and are chosen for illustrative purposes, in order to point out the features, which we consider to be important.

Secondary chemical flooding

First, we consider the secondary recovery, which means that injection of the chemical solution is performed under irreducible initial water saturation. The governing system of equations for the problem, accounting for the particular choice of sorption isotherm (2.58) is represented by [86]:

$$\partial_{t_D} s + \partial_{x_D} f_w = 0 \tag{2.59}$$

$$(s + \Gamma)\partial_{t_D} c + f_w \partial_{x_D} c = 0 \tag{2.60}$$

$$s(0, x_D) = s_{wi}, \qquad s(t_D, 0) = 1 - s_{orc} \tag{2.61}$$

$$c(0, x_D) = 0, \qquad c(t_D, 0) = c^J \tag{2.62}$$

where s_{orc} is the residual oil saturation achieved by the injection of chemical solution (in case of polymer injection $s_{orc} = s_{orw}$)

The fractional flow functions for the water $f_w(s, 0)$ and the chemical solution $f_w(s, c^J)$ are shown in Figure 2.7b. The chemical in the injected water decreases the fractional flow function which corresponds to an increased fraction of oil in the flow. The solution for the saturation, valid for relatively small adsorption of the chemical, is illustrated in Figure 2.7a. The most important feature of the solution is the formation of an oil bank ($x_{cf} < x < x_{w1}$), which occurs due to an increased displacement efficiency caused by the injection of chemical. After the water breakthrough, the fraction of oil in the flow will jump from 1 to f_{w1} and remain constant until the chemical shock (shown at $x = x_{cf}$) reaches the outlet.

The oil bank travels ahead of the concentration front where the chemical concentration changes from zero (ahead of the front) to c^J (behind the front). Hence, the chemical appears in the effluent only after the oil bank is produced. The denuded water zone in Figure 2.7a ($x_{cf} < x < x_{wb}$) arises due to adsorption of the chemical from the solution. The thickness of the denuded zone increases as it moves through porous media. The same happens to other zones.

Increasing Γ (large losses) results in less efficiency of the chemical flooding. This may be understood analyzing the fractional flow functions in Figure 2.7b. The displacement front of

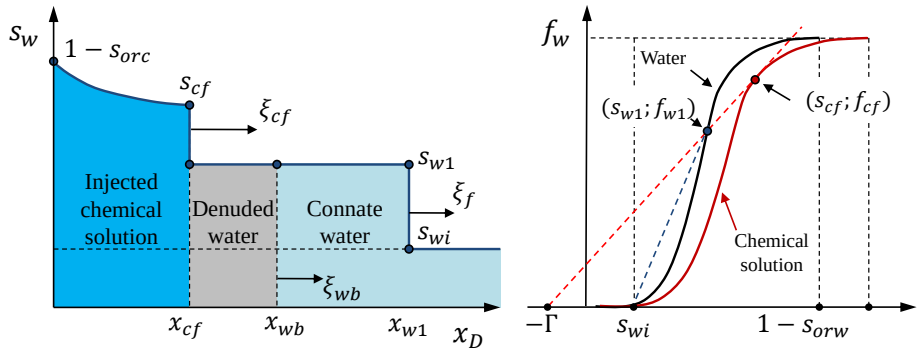

Figure 2.7: a) Saturation profile for the case of injection of the chemical solution into the reservoir at irreducible water saturation. b) Fractional flow functions for water and the injected chemical solution.

connate water is represented by the blue dashed line connecting the points $P_0 = (s_{wi}, 0)$ and $P_{w1} = (s_{w1}, f_{w1})$. The chemical shock is represented by the red dashed line connecting the points P_{w1} and $P_{wf} = (s_{cf}, f_{cf})$. As Γ is increased, the point P_{w1} moves up along the fractional flow function curve decreasing the fraction of oil in flow for the oil bank and decreasing the velocity of the chemical shock ξ_{cf}. Therefore, if adsorption is large, after the connate water breakthrough the solution predicts slow production at a constant rate during a long period of injection. For very large Γ the shape of the solution changes (not considered here).

Tertiary chemical flooding

During tertiary flooding, the chemical solution is injected into the porous medium at high initial water saturation. We assume this saturation to correspond to the residual oil saturation s_{orw} that can be achieved with the injection of water without chemical. A more precise analysis may be carried out assuming that the initial distribution of the saturation is non-uniform and corresponds to the saturation profile at a late stage of the secondary flooding (after the water breakthrough). This non-self-similar solution will not be discussed here. See [39] for details.

The only change to be introduced in the governing system of equations (2.59)–(2.62) is the initial condition (2.61) which is replaced with:

$$s(0, x_D) = 1 - s_{orw} \tag{2.63}$$

The fractional flow functions for the water $f_w(s, 0)$ and the chemical solution $f_w(s, c^J)$ are shown in Figure 2.8b. The solution for the saturation in this case is illustrated in Figure 2.8a. Similar to the secondary recovery process, the most important feature of the solution is

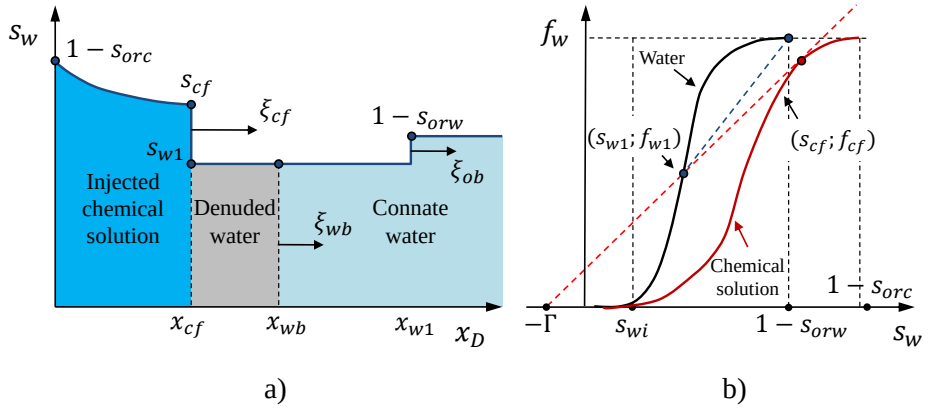

Figure 2.8: a) Saturation profile for the case of injection of the chemical solution into reservoir at large initial water saturation s_{orw}. b) Fractional flow functions for water and the injected chemical solution.

formation of an oil bank ($x_{cf} < x < x_{w1}$). This oil bank is formed by the mobilized oil; ahead of the oil bank ($x > x_{w1}$) oil is immobile. Solution for the concentration of the chemical is similar to that in the secondary flooding. Adsorption from the solution results in the occurrence of the denuded zone free of chemical. The oil bank travels ahead of the concentration front of the chemical.

Increasing Γ results in less efficiency of the chemical flooding. This may be understood by analyzing the fractional flow curves in Figure 2.8b. As Γ is increased, the point $P_{w1} = (s_{w1}, f_{w1})$ moves up along the fractional flow function curve decreasing the fraction of oil in the flow for the oil bank and decreasing the velocities of the forward and the backward fronts of the oil bank ξ_{ob} and ξ_{cf} respectively. Therefore, if retention of the chemical in the porous medium is large, the oil bank is produced after a long period of injection.

2.4 Conclusions

The effect of the smart water flooding is usually related to the change of the wetting state of the rock. To develop a macroscopic model that can account for the wettability alteration, it is necessary to relate wettability to the physicochemical processes on the rock surface. This can be achieved by considering adsorption of potential determining ions. Adsorption of the ions is expected to change the charge and, hence, the surface potential of the rock. Simple adsorption models cannot provide an accurate description of the sorption process. The main reason is that they do not account for the electrostatic interaction between ions in the solution and the surface. Therefore, more advanced surface complexation models are to be considered.

Change of the wetting state of the rock may affect transport properties of the fluids, resulting in increased efficiency of the flooding. The macroscopic model for the two-phase flow in porous media has been described in the literature, and analytical solutions are well known. It is important to introduce the described surface chemistry in the macroscopic models.

One of the difficulties is that there is no common knowledge of how exactly the transport properties will change by action of the surface effects, as there is no general way to evaluate the relative permeability functions. One should be especially careful when considering tertiary recovery. The extended Buckley-Leverett solution assumes that the ganglia of the trapped oil join the continuous phase and flow with it when mobilized. It is possible, however, that other mechanisms govern the flow of oil in this case.

3

Numerical Model

In this chapter, we describe the approach that was used to obtain the numerical scheme for the reactive two-phase flow in porous media. In Section 3.1, we introduce notations and general formalism based on the conservation laws. In Section 3.2, we explain an approach used to calculate the spatial differential operators and fluxes. Section 3.3 describes the integration of the discretized system of equations. The approach used to obtain discretization scheme of the second order of accuracy is described in the Section 3.4.

3.1 General System of Conservation Laws

We consider a spatial domain $\Omega \subset \mathbb{R}^3$ representing porous medium, which can be a petroleum reservoir or a core plug. The boundary of the spatial domain is $\partial\Omega \subset \mathbb{R}^3$. Latin indices i, j are reserved to denote the discrete grid cells.

The bulk phases considered are water (subscript *w*), oil (subscript *o*) and solid (subscript *s*). For a number of problems it is also important to consider surface phases that are indexed with subscript α_s. The phases are denoted with subscript $\alpha \in \{w, o, s, \alpha_s\}$. Chemical species are indexed with the subscript $a \in \mathrm{B}_{sp} = \{1, \ldots, n_{sp}\}$. The subset $\mathrm{B}_{sp}^{\alpha} \subset \mathrm{B}_{sp}$ represents species that belong to phase α. We also use $\mathrm{B}_{sp}^{bulk} \subset \mathrm{B}_{sp}$ which is a subset of the indices of the species in the bulk phases and $\mathrm{B}_{sp}^{surf} \in \mathrm{B}_{sp}$ is a subset of the indices of the surface species. If the two species represent the same chemical substance occurring in different phases it may be convenient to denote such species with two indexes: $\{b, \alpha\}$, b for the chemical substance and α for the phase in which it occurs.

We consider a set of material balance equations in the form

$$\partial_t \mathbf{U} + \nabla \cdot \vec{\mathbf{F}} = \mathbf{Q} + \mathbf{S} \tag{3.1}$$

where **U** is the accumulation term, $\vec{\mathbf{F}}$ is the flux. The source term **Q** in the right hand side of (3.1) corresponds to injection/production of the phases and species, while the source term **S** corresponds to material transfer due to physicochemical interactions in the system. Variables introduced in equation (3.1) are explained below.

3.1.1 Accumulation Term

Let $U_\alpha = U_\alpha(t, \vec{x}), \alpha = \{w, o, s\}$ be the mass concentrations of water, oil and solid phases per unit volume of the porous medium as functions of time t and position $\vec{x} \in \Omega$. According to this definition:

$$U_\alpha = \rho_\alpha \Theta_\alpha, \quad \alpha = w, o, s \tag{3.2}$$

where ρ_α is the phase density and Θ_α is the volumetric fraction of the porous medium occupied by the phase α. The volumetric fractions are determined by the porosity and fluid saturations:

$$\Theta_w = \phi s, \quad \Theta_o = \phi(1 - s), \quad \Theta_s = 1 - \phi \tag{3.3}$$

In a similar manner, we introduce the global concentrations (concentrations per unit volume of the porous medium) of the chemical species U_a in the bulk phases:

$$U_a = \Theta_\alpha c_a, \quad \alpha = w, o, s, \quad a \in \mathrm{B}_{sp}^{\alpha}, \tag{3.4}$$

and on the surface:

$$U_a = \hat{A}_{\alpha_s} \sigma_a, \quad a \in \mathrm{B}_{sp}^{\alpha_s} \tag{3.5}$$

where c_a is the molar concentration of species per unit volume of corresponding phase, $\hat{A}_{\alpha_s}$ is the specific surface area and σ_a is the surface molar concentration.

We now introduce a vector variable **U** representing the accumulation term, such that:

$$\mathbf{U} = \begin{bmatrix} U_\alpha \\ U_a \end{bmatrix}, \quad \alpha = w, o, s, \quad a = 1, \ldots, n_{sp} \tag{3.6}$$

This is not the only possible choice of the accumulation term. Arbitrary linear transformations may be applied to the system (3.1) resulting in different forms of conservation laws for the same problem. Such transformations are usually applied to provide a form of conservation laws convenient for numerical modeling.

3.1.2 Primitive Variables

Variables **U** are associated with the accumulation term. Even though this term identifies the state of the system, it is not always convenient for calculation of other parameters. The reason is that most of the closure relations determining densities, relative permeabilities, and rates of chemical reactions, used in the model, are not described in terms of conservative variables

U; instead, *primitive* or *physical* variables **W** are usually considered [99]. The choice of primitive variables may be arbitrary and depends on the problem formulation. A possible choice of primitive variables is:

$$\mathbf{W} = \begin{bmatrix} P \\ s \\ \phi \\ c_a \\ \sigma_b \end{bmatrix}, \quad a \in \mathrm{B}_{sp}^{bulk}, \quad b \in \mathrm{B}_{sp}^{surf} \tag{3.7}$$

where P is pressure. As it was previously discussed in Chapter 3, we do not account for capillary effects; hence, pressures in the fluid phases are equal: $P = P_w = P_o$. This particular choice of primitive variables is convenient, since transport properties of the fluids are primarily calculated based on saturation, while chemical interactions are calculated in terms of concentrations. However, the set of primitive variables given by (3.7) may be excessive for some problems. For example, calculation of pressure is not required for a flow of incompressible fluids in one dimension; porosity may be constant; presence of equilibrium chemical reactions allows for establishing relations between species concentrations and reduction of the number of independent variables. Therefore, a particular choice of the primitive variables is to be discussed separately for each specific problem. The accumulation term **U** can be calculated given the set of primary variables, so that $\mathbf{U} = \mathbf{U}(\mathbf{W})$.

3.1.3 Flux Term

The components of the flux term $\vec{F}_\alpha = \vec{F}_\alpha(t, \vec{x})$ determine the flow of the fluid phases and are calculated according to the generalized Darcy laws:

$$\vec{F}_\alpha = \rho_\alpha \lambda_\alpha \mathbf{k} \cdot \nabla P, \quad \alpha = w, o \tag{3.8}$$

where λ_α is the phase mobility and **k** is the absolute permeability tensor. Similarly, the fluxes of chemical species in the fluids $\vec{F}_a = \vec{F}_a(t, \vec{x})$ are defined as

$$\vec{F}_a = c_a \lambda_\alpha \mathbf{k} \cdot \nabla P, \quad \alpha = w, o, \quad a \in \mathrm{B}_{sp}^{\alpha} \tag{3.9}$$

The fluxes for the solid phase and its components are zero. In general, the fluxes of surface species may be non-zero. However, we are mainly concerned with the fluid-rock interface that is static and does not allow for surface transport:

$$\vec{F}_s = 0, \quad \vec{F}_a = 0, \quad a \in B_{sp}^{s} \cup B_{sp}^{surf} \tag{3.10}$$

The components of the flux term are calculated based on primitive variables **W**. We now introduce an array of fluxes $\vec{\mathbf{F}} = \vec{\mathbf{F}}(\mathbf{W})$ such that

$$\vec{\mathbf{F}} = \begin{bmatrix} \vec{F}_{\alpha} \\ \vec{F}_{a} \end{bmatrix}, \quad \alpha = w, o, s, \quad a = 1, \ldots, n_{sp} \tag{3.11}$$

3.1.4 Source Terms

The source term **Q** arises in the reservoir modeling, where injection and production is performed through injection and production wells that are located inside the domain Ω. For the numerical model of a laboratory experiment, the domain Ω is a cylinder representing a core plug. In this case, injection and production of fluids are performed at the core plug facets and are expressed by appropriate boundary conditions.

The reactive source term **S** arises due to physicochemical interactions in the system (e.g. chemical reactions, sorption). It is responsible for mass transfer between phases and transformation of species. Similarly to the previously introduced variables, the source term has the form:

$$\mathbf{S} = \begin{bmatrix} S_{\alpha} \\ S_{a} \end{bmatrix}, \quad \alpha = w, o, s, \quad a = 1, \ldots, n_{sp} \tag{3.12}$$

The source term for the phases is related to the chemical species source terms via:

$$S_{\alpha} = \sum_{a \in \mathrm{B}_{sp}^{\alpha}} M_a S_a \tag{3.13}$$

where M_a is the molar weight of component. Equation (3.13) states that the change of the phase mass is due to the change of species concentrations.

The source term for the species S_a is calculated based on reaction rates and the matrix of stoichiometric coefficients ν_a^n, where superscript n is used to denote the reaction. For a system containing n_{sp} species undergoing n_{react} reactions, the stoichiometric matrix has the size of $n_{react} \times n_{sp}$ and defines reactions according to

$$\sum_{a=1}^{n_{sp}} \nu_a^n \mathrm{X}_a = 0, \quad n = 1, \ldots, n_{react} \tag{3.14}$$

where X_a denotes chemical species. The stoichiometric coefficients are determined in the following manner: $\nu_a^n > 0$ for the products, and $\nu_a^n < 0$ for reactiants. Given the reaction rate $\dot{r}_n$ for each of the reactions, the source term S_a is calculated according to

$$S_a = \sum_{n=1}^{n_{react}} \nu_a^n \dot{r}_n, \quad a = 1,...,n_{sp} \tag{3.15}$$

As discussed in Chapter 2, the rates of reactions are typically calculated based on the species activities, which are the functions of species concentrations. According to the law of mass action, the reaction rate is given by the following equation:

$$\dot{r}_n = k_n(IAP_n^+ - IAP_n^- \,/\, K_n), \quad n = 1,...,n_{react} \tag{3.16}$$

where k_n is the rate constant and K_n is the equilibrium constant, IAP stands for the ion activity product for the forward and backward reactions:

$$IAP_n^+ = \prod_{a=1}^{n_{sp}} [\mathrm{X}_a]^{(|\nu_a^n| - \nu_a^n)/2} \tag{3.17}$$

$$IAP_n^- = \prod_{a=1}^{n_{sp}} [\mathrm{X}_a]^{(|\nu_a^n| + \nu_a^n)/2} \tag{3.18}$$

where $[\mathrm{X}_a]$ is used to denote the species activities. According to equations (3.17) and (3.18) the ion activity product for the forward reaction is calculated based on the activities of species with $\nu_a^n < 0$ (reactants), while the ion activity product for the backward reaction is calculated based on the activities of species with $\nu_a^n > 0$ (products).

The rate law (3.16) cannot be applied directly to take into account equilibrium reactions, as such reactions are assumed to be infinitely fast requiring $k_n \to \infty$. Therefore, infinitely large terms appear in the right hand side of material balance equations for the species involved in the equilibrium reactions. A general way to handle this asymptotic terms is to apply a linear transformation to a system of conservation laws (3.1). The required transformation is expressed by the *Equilibrium-Rate-Annihilation* (ERA) matrix [100]. It can be shown that application of the linear transformation given by the ERA matrix reduces the number of equations in the system of conservation laws by the number of equilibrium reactions n^{eq}. The new system does not contain rates corresponding to equilibrium reactions. The excluded n^{eq} equations are substituted with the equilibrium conditions:

$$K_n = IAP_n, \quad n = 1,...,n^{eq} \tag{3.19}$$

Thus, the concentrations of n^{eq} *secondary species* can be determined through concentrations of $n_p = n_{sp} - n^{eq}$ *primary species* using the equilibrium conditions (3.19).

To illustrate this approach, we consider the flow of solute in water that can adsorb on the rock surface. The two species that are to be considered represent the same chemical substance

and, therefore, can be introduced as $X_{1,w}$ and $X_{1,surf}$ (instead of X_1 and X_2). According to (3.14) the adsorption reaction is expressed as

$$-X_{1,w} + X_{1,surf} = 0 \tag{3.20}$$

with $\nu = [-1; 1]$ (if no other reactions take place). According to the description introduced above, the conservation laws for the solute in water and for the surface species in the absence of convective sources are:

$$\partial_t U_{1,w} + \nabla \cdot F_{1,w} = -\dot{r}_{sorb} \tag{3.21}$$

$$\partial_t U_{1,surf} = \dot{r}_{sorb} \tag{3.22}$$

The linear transformation matrix, in this case, is $E = [1, 1]$, which corresponds to the summation of the two equations resulting in

$$\partial_t (U_{1,w} + U_{1,surf}) + \nabla \cdot F_{1,w} = 0 \tag{3.23}$$

In terms of primitive variables $c_{1,w}$ and $\sigma_{1,surf}$, the material balance becomes

$$\partial_t (\phi s c_{1,w} + \hat{A}_{surf} \sigma_{1,surf}) + \nabla \cdot (\vec{u}_w c_{1,w}) = 0 \tag{3.24}$$

In the case of equilibrium sorption, the material balance for the surface species (3.22) is to be substituted by the equilibrium condition $\dot{r}_{sorb} = 0$. This consideration demonstrates that in many cases it is easy to determine in which way material balance equations should be combined in order to eliminate the rates of chemical reactions. For the problems where species participate in multiple chemical reactions, the general approach that involves the ERA matrix may be more practical.

A similar transformation can be applied to eliminate the kinetic reaction rates on the right-hand side of equation (3.1). This transformation does not decrease the order of the governing system of equations. However, it makes it possible to obtain a form of conservation laws that can be conveniently solved by the splitting approach introduced in Section 3.3.

3.1.5 Initial and Boundary Conditions

Assuming that all the closure relations required to calculate accumulation term, fluxes and reactive source term are given, it is only necessary to formulate initial and boundary conditions to close the system of conservation laws (3.1). The initial conditions are set by an appropriate choice of primitive variables at the initial time moment $\mathbf{W}(0, \vec{x})$. A typical choice of the initial conditions representing a laboratory water flood experiment is homogeneous initial saturation, pressure and concentrations of species

$$\mathbf{W}(0,\vec{x}) = \mathbf{W}^{(0)} \tag{3.25}$$

The boundary conditions are specified at the boundary $\partial\Omega$. For a laboratory flood domain Ω has a cylindrical shape, such that one facet corresponds to the injection surface (inlet) $\partial\Omega_{in}$, while another corresponds to the production surface (outlet) $\partial\Omega_{out}$. The side surface $\partial\Omega_{nf}$ is impermeable. The boundary conditions at the inlet and the side surface read

$$\vec{\mathbf{F}} = -\vec{n}\cdot(\mathbf{q}^{inj}(t)) \,/\, A_{\partial\Omega_{in}} \quad \vec{x} \in \partial\Omega_{in} \tag{3.26}$$

$$\vec{\mathbf{F}} = \vec{\mathbf{0}} \quad \vec{x} \in \partial\Omega_{nf} \tag{3.27}$$

where $\vec{n}$ is the outward normal vector to the surface $\partial\Omega_{in}$ and $\mathbf{q}^{inj} = [\mathbf{q}_\alpha, \mathbf{q}_a]^T$ is the specified injection rate with the following components:

$$\begin{aligned} q_\alpha &= \rho_\alpha q_\alpha^{inj}, \quad \alpha = w,o, \\ q_s &= 0, \\ q_a &= c_a^{inj} q_\alpha^{inj}, \quad \alpha = w,o, \quad a \in \mathrm{B}_{sp}^{\alpha}, \\ q_a &= 0, \qquad\qquad a \in B_{sp}^{s} \cup B_{sp}^{surf}, \end{aligned} \tag{3.28}$$

$q_\alpha^{inj} = q_\alpha^{inj}(t)$ is the variable volumetric injection rate of fluids, and $c_a^{inj} = c_a^{inj}(t)$ is the injected fluid composition.

The boundary condition at the outlet $\partial\Omega_{out}$ is usually given by the outlet pressure:

$$P(t,\vec{x}) = P_{out}(t) \quad \vec{x} \in \partial\Omega_{out} \tag{3.29}$$

This is sufficient to calculate the outgoing flux and to close the system (3.1), (3.25), (3.26), (3.27), provided that all necessary closure relations are given.

3.1.6 Pressure Equation

A general form of the pressure equation is obtained by combining the material balance equations for the bulk phases

$$\sum_\alpha \rho_\alpha^{-1}\partial_t U_\alpha + \sum_\alpha \rho_\alpha^{-1}\nabla\cdot\vec{F}_\alpha = \sum_\alpha \rho_\alpha^{-1} Q_\alpha + \sum_\alpha \rho_\alpha^{-1} S_\alpha \tag{3.30}$$

Taking into account (3.2) and volumetric constraint $\sum_\alpha \Theta_\alpha = 1$ one obtains

$$\sum_{\alpha}\Theta_{\alpha}\rho_{\alpha}^{-1}\partial_{t}\rho_{\alpha}+\sum_{\alpha}\rho_{\alpha}^{-1}\nabla\cdot\vec{F}_{\alpha}=\sum_{\alpha}\rho_{\alpha}^{-1}Q_{\alpha}+\sum_{\alpha}\rho_{\alpha}^{-1}S_{\alpha} \tag{3.31}$$

In many applications (like immiscible flooding by a compressible fluid), the fluid density is considered to be a function of pressure only. Therefore, equation (3.31) contains only pressure under the time derivative, which explains the reason to call it the pressure equation and to consider separately. In the cases where density also depends on fluid composition c_a, the time derivative of concentration will arise on the left-hand side of the equation. This will affect the choice of the solution scheme, as discussed later.

Another feature of equation (3.31) is that the last term on the right-hand side $\sum_{\alpha}\rho_{\alpha}^{-1}S_{\alpha}$ may be non-zero. The combined mass of the phases cannot change due to reactions between them (assuming that the surface mass transfer is negligible) and $\sum_{\alpha}S_{\alpha}=0$. However, $\sum_{\alpha}\rho_{\alpha}^{-1}S_{\alpha}$ is not equal to zero, which means that there is no volumetric balance associated with the interphase mass transfer. Therefore, a considerable mass transfer is expected to have an effect on pressure in the system.

3.2 Spatial Discretization

Below we describe the numerical representation of the spatial derivative operators in the general system of conservation laws (3.1). Different approaches may be used for this purpose. Most of them are variations and combinations of the three basic methods: the finite difference method (FDM), the finite volume method (FVM) and the finite element method (FEM) [101-103].

In our work FVM has been chosen for the spatial discretization. It is based on the control volume formulation. This method is extensively used in fluid mechanics, heat and mass transfer, and the associated problems of chemical and petroleum engineering [102]. The FVM can be applied for arbitrary geometries and both structured and unstructured grids. A physical domain is represented as an union of smaller domains called control volumes. The solution is approximated on an element by the cell average at the center of each element. The flux term is reduced to a surface integral by using the divergence theorem, which results in the conservative scheme. Computation of the boundary fluxes is usually performed using the two-point flux approximation (TPFA) [104], which is of the first order of accuracy in space. Higher order schemes based on multi-point flux approximations (MPFA) are not easy to obtain in the case of complex geometries; additionally, they also experience stability issues in cases where shocks are present in the solutions. One of the possibilities to overcome this difficulty is to use the flux limiters [99, 101]. The main idea behind this approach is to use linear piece-wise approximations of variables at the cell boundaries. In this approach, the accuracy of discretization degrades to the first order in the neighborhood of the shock but tends to the second order over smooth parts of the solution.

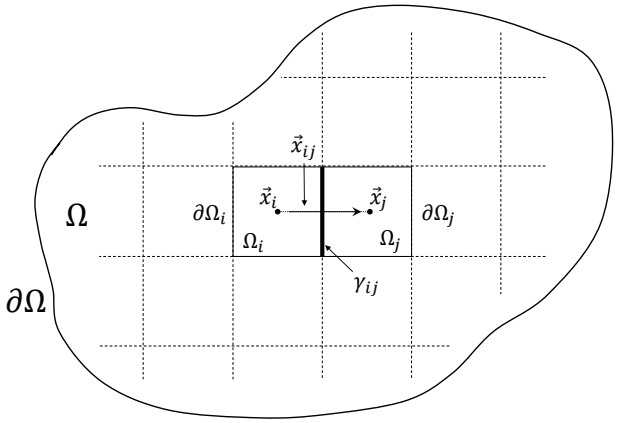

Figure 3.1: Discretized domain

The numerical models that were implemented in this work relied mainly on the TPFA (Chapters 5 and 7). A numerical scheme of the second order of accuracy was used for computations reported in Chapter 6 and will be discussed separately in Section 3.4. In this thesis, we report only our results for 1D simulations. However, the numerical models were implemented with a possibility to consider the reactive transport problem in multiple dimensions.

3.2.1 Finite Volume Approach

In this section, we present a general form of the finite volume discretization approach. According to the finite volume formulation, the physical domain Ω is divided into N non-intersecting subdomains Ω_i as schematically illustrated in Figure 3.1. Additionally, we identify as $\partial\Omega_{in}$ and $\partial\Omega_{out}$ the boundaries of the domain Ω through which injection and production occur, and introduce the inlet and the outlet subdomains Ω_0 and Ω_{N+1} respectively.

Boundaries γ_{ij} of the subdomains $\partial\Omega_i$, $i \in \mathcal{N} = \{1,2,\ldots,N\}$ are numbered according to

$$\gamma_{ij} = \Omega_i \cap \Omega_j, \quad i \in \mathcal{N}, \quad j \in \bar{\mathcal{N}}, \quad i \neq j \tag{3.32}$$

where $\bar{\mathcal{N}} = \mathcal{N} \cup \{0, N+1\}$. Let $\mathcal{N}^{(i)} \subset \mathcal{N}$ and $\bar{\mathcal{N}}^{(i)} \subset \bar{\mathcal{N}}$ be the sets of indices for the neighboring subdomains for the i^{th} control volume.

Each control volume contains a nodal point. All the dynamic variables such as saturation, pressure, and concentrations are represented by their values at the nodal point, calculated as

the averages over the corresponding control volume. The location of the i^{th} control volume is denoted by $\vec{x}_i$, and we define the internode connection vector

$$\vec{x}_{ij} = \vec{x}_i - \vec{x}_j, \quad |\vec{x}_{ij}| = \Delta x_{ij}, \quad i \in \mathcal{N}, j \in \mathcal{N}^{(i)} \tag{3.33}$$

For all the discretized variables used below, designation u_i means that the value of u is evaluated at the nodal point $\vec{x}_i$, while u_{ij} means that this value is evaluated at the interface γ_{ij}. The volume of the i^{th} control element is denoted by V_i .

Consider a general advection-reaction equation (3.1). The discretized equation is obtained by performing integration of (3.1) over the control volume Ω_i

$$\partial_t \int_{\Omega_i} \mathbf{U} dV = -\int_{\Omega_i} \nabla \cdot \vec{\mathbf{F}} dV + \int_{\Omega_i} (\mathbf{Q} + \mathbf{S}) dV, \quad i \in \mathcal{N} \tag{3.34}$$

The volume integral of the accumulation term is discretized using the average value of **U** over the control volume:

$$\int_{\Omega_i} \mathbf{U} dV = (\mathbf{U}V)_i, \quad i \in \mathcal{N} \tag{3.35}$$

Similarly, the volume integral of the source terms on the right-hand side is substituted by

$$\int_{\Omega_i} (\mathbf{Q} + \mathbf{S}) dV = ((\mathbf{Q} + \mathbf{S})V)_i, \quad i \in \mathcal{N} \tag{3.36}$$

The volume integral of the convective flux divergence is transformed into surface integral using the Gauss' divergence theorem:

$$\int_{\Omega_i} \nabla \cdot \vec{\mathbf{F}} = \int_{\partial\Omega_i} \vec{n}_i \cdot \vec{\mathbf{F}} dS = \sum_{j \in \bar{\mathcal{N}}^{(i)}} \int_{\gamma_{ij}} \vec{n}_i \cdot \vec{\mathbf{F}} dS, \quad i \in \mathcal{N} \tag{3.37}$$

where $\vec{n}_i$ is the outward normal vector to the subdomain boundary $\partial\Omega_i$. An approximation of the integral over the cell boundary γ_{ij} is obtained using the midpoint rule:

$$\int_{\gamma_{ij}} \vec{n}_i \cdot \vec{\mathbf{F}} dS = (\vec{n} \cdot \vec{\mathbf{F}} A)_{ij}, \quad i \in \mathcal{N}, j \in \bar{\mathcal{N}}^{(i)} \tag{3.38}$$

where $\vec{n}_{ij}$ is the normal vector of interface γ_{ij}, $\vec{\mathbf{F}}_{ij}$ is the flux across interface, and A_{ij} is the interface area. Substitution of the discrete representations of the volume integrals (3.35), (3.36) and (3.38) into (3.34) gives the discrete system of conservation laws in the form:

$$V_i \frac{d}{dt} \mathbf{U}_i = \sum_{j \in \bar{\mathcal{N}}^{(i)}} (\vec{n} \cdot \vec{\mathbf{F}} A)_{ij} + (\mathbf{Q}_i + \mathbf{S}_i) V_i \quad i \in \mathcal{N} \tag{3.39}$$

For the phase mass transport and transport of the chemical species, the fluxes between two subdomains are given by the following expressions:

$$\vec{\mathbf{F}}_{\alpha,ij} = (\rho_\alpha \vec{u}_\alpha)_{ij} = -(\rho_\alpha \lambda_\alpha \mathbf{k} \cdot \nabla P)_{ij}, \quad i \in \mathcal{N}, j \in \mathcal{N}^{(i)}, \quad \alpha = w, o \tag{3.40}$$

$$\vec{\mathbf{F}}_{a,ij} = (c_a \vec{u}_\alpha)_{ij} = -(c_a \lambda_\alpha \mathbf{k} \cdot \nabla P)_{ij}, \ i \in \mathcal{N}, j \in \mathcal{N}^{(i)}; \alpha = w, o; \ a \in \mathrm{B}_{sp}^{\alpha} \tag{3.41}$$

Due to apparent similarity of equations (3.40) and (3.41), we perform transformations only with the phase flux while the result for the flux of chemical species is obtained by analogy. Substitution of (3.40) into (3.38) yields

$$(\vec{n} \cdot \vec{\mathbf{F}} A)_{ij} = \vec{n}_{ij} \cdot (A\mathbf{k})_{ij} (\rho_\alpha \lambda_\alpha)_{ij} \cdot \nabla P_{ij}, \quad i \in \mathcal{N}, j \in \mathcal{N}^{(i)} \tag{3.42}$$

For the TPFA a first order approximation of the pressure gradient ∇P_{ij} is used:

$$\nabla P_{ij} = \left(\frac{\Delta P}{\Delta x} \frac{\vec{x}}{\Delta x} \right)_{ij} = \left(\frac{\Delta P}{\Delta x} \right)_{ij} \vec{e}_{ij}, \quad i \in \mathcal{N}, j \in \mathcal{N}^{(i)} \tag{3.43}$$

Where $\Delta P_{ij} = P_j - P_i$, $\vec{e}_{ij} = \vec{x}_{ij}/\Delta x_{ij}$ is the unit vector along the internode connection. Substitution of (3.43) in (3.42) yields

$$(\vec{n} \cdot \vec{\mathbf{F}} A)_{ij} = \vec{n}_{ij} \cdot \left(\frac{A\mathbf{k}}{\Delta x} \right)_{ij} \cdot \vec{e}_{ij} \cdot (\rho_\alpha \lambda_\alpha)_{ij} \Delta P_{ij}, \quad i \in \mathcal{N}, j \in \mathcal{N}^{(i)} \tag{3.44}$$

The transmissibility is usually introduced according to [105, 106]

$$\Upsilon_{\alpha,ij} = \begin{cases} \left(\vec{n} \cdot \mathbf{k} \cdot \vec{e} \, \frac{A}{\Delta x} \right)_{ij} \cdot (\rho_\alpha \lambda_\alpha)_{ij}, & j \in \mathcal{N}^{(i)} \\ 0, & j \notin \mathcal{N}^{(i)} \end{cases} \quad i \in \mathcal{N} \tag{3.45}$$

Transmissibilities for the component fluxes are obtained by substituting ρ_α with c_a in equation (3.45). More details are given in the next subsection.

Using the transmissibility one may write

$$\sum_{j \in \mathcal{N}^{(i)}} (\vec{n} \cdot \vec{\mathbf{F}} A)_{ij} = \sum_{j \in \mathcal{N}} (\Upsilon \Delta P)_{ij} \quad i \in \mathcal{N} \tag{3.46}$$

For the subdomains in contact with the inlet and outlet subdomains equation (3.39) contains additional terms corresponding to the flux through the external boundary $\partial\Omega$. According to the formulated boundary conditions, injection flux is specified at the inlet according to (3.26) , and pressure is specified at the outlet according to (3.29). The external boundary fluxes are then calculated as follows

$$\int_{\gamma_{i,0}} \vec{n}_i \cdot \vec{\mathbf{F}} dS = (\vec{n} \cdot \vec{\mathbf{F}}^{inj} A)_{i,0}, \quad i \in \mathcal{N}^{(0)} \tag{3.47}$$

$$\int_{\gamma_{i,N+1}} \vec{n}_i \cdot \vec{\mathbf{F}} dS = (\Upsilon \Delta P)_{i,N+1}, \quad i \in \mathcal{N}^{(N+1)} \tag{3.48}$$

where $P_{N+1} = P_{out}$.

To simplify the notations we define

$$(\mathbf{Q}^{BC} V)_i = \begin{cases} (\vec{n} \cdot \vec{\mathbf{F}}^{inj} A)_{0,i}, & i \in \mathcal{N}^{(0)} \\ (\Upsilon \Delta P)_{i,N+1}, & i \in \mathcal{N}^{(N+1)} \\ 0, & \text{otherwise} \end{cases} \tag{3.49}$$

Substituting relations (3.46) and (3.49) in the discrete system of conservation laws (3.39) yields

$$V_i \frac{d}{dt} \mathbf{U}_i = \sum_{j \in \mathcal{N}} (\Upsilon \Delta P)_{ij} + (\mathbf{Q}_i^{BC} + \mathbf{Q}_i + \mathbf{S}_i) V_i, \quad i \in \mathcal{N} \tag{3.50}$$

The discrete formulation of the system of conservation laws makes it possible to account for the boundary conditions by introducing an additional source term $\mathbf{Q}_i^{BC}$ defined according to equation (3.49). The form of conservation laws represented by equation (3.39) is more general than those given by equation (3.50) as, in general, different approaches may be used to calculate boundary fluxes.

3.2.2 Calculation of Transmissibilities

A common approach to calculate transmissibility is to consider it as a product of the geometric and the fluid parts [105]. The first term in the brackets in equation (3.45) represents the geometric part Γ_{ij} which depends only on reservoir properties and the grid:

$$\Gamma_{ij} = \left(\vec{n} \cdot \mathbf{k} \cdot \vec{e} \frac{A}{\Delta x} \right)_{ij}, \quad i \in \mathcal{N}, j \in \mathcal{N}^{(i)} \tag{3.51}$$

The fluid part $H_{\alpha,ij}$ is determined by the fluid density ρ_α and mobility λ_α

$$H_{\alpha,ij} = (\rho_\alpha \lambda_\alpha)_{ij}, \quad i \in \mathcal{N}, j \in \mathcal{N}^{(i)} \tag{3.52}$$

Calculation of the geometric part of the transmissibility is not straightforward for a heterogeneous porous medium in the case of arbitrary grid geometry, especially if the cell boundaries are not coincident [107]. In this work we apply the Cartesian grids and the

diagonal permeability tensor $\mathbf{k} = diag(k_{xx}, k_{yy}, k_{zz})$. For the Cartesian grid, the normal vector at the cell interface is codirected with the internode vector $\vec{e}_{ij} = \vec{n}_{ij}$. Therefore, the product $\vec{n} \cdot \mathbf{k} \cdot \vec{e}$ is equal to k_{xx}, k_{yy} or k_{zz} depending on the location of a neighboring cell. A subdomain with a lower permeability controls the flow between the adjacent subdomains, and the transmissibility is calculated as a harmonic average [106]. For example, if i and j are the neighbors in x direction, calculation of the geometric part Γ_{ij} is performed according to

$$\Gamma_{ij} = \left(k_{xx} \frac{A}{\Delta x} \right)_{ij} \qquad i \in \mathcal{N}, j \in \mathcal{N}^{(i)} \tag{3.53}$$

$$(k_{xx})_{ij} = \frac{\Delta x_{ij}}{\Delta x_i \,/\, k_{xx,i} + \Delta x_j \,/\, k_{xx,j}} \tag{3.54}$$

where Δx_i is the distance between the nodal center $\vec{x}_i$ and the boundary γ_{ij}, so that $\Delta x_{ij} = \Delta x_i + \Delta x_j$. In the case of uniform grid spacing such that $\Delta x_i = \Delta x_j, \forall i, j$, the average (3.54) becomes

$$(k_{xx})_{ij} = \frac{(k_{xx})_i (k_{xx})_j}{(k_{xx})_i + (k_{xx})_j} \tag{3.55}$$

For the calculation of the geometric part at an interface between the domain and the outlet $\Gamma_{i,N+1}$, it is assumed that the flow is determined only by permeability inside the domain and that $\mathbf{k}_{i,N+1} = \mathbf{k}_i$.

The fluid part of transmissibility is calculated using the single point upwind (SPU) scheme [101]. In the absence of gravity, diffusion, and capillary pressure difference, the direction of flow at the interface is determined only by the pressure difference:

$$H_{\alpha,ij} = \begin{cases} (\rho_\alpha \lambda_\alpha)_i & \Delta P_{ij} < 0 \\ (\rho_\alpha \lambda_\alpha)_j & \Delta P_{ij} > 0 \end{cases} \quad i \in \mathcal{N}, j \in \mathcal{N}^{(i)} \tag{3.56}$$

One of the reasons to split the transmissibility into the geometric and fluid parts is that for inert porous medium, where porosity and absolute permeability are constant, calculation of the geometric part is performed once at the initialization step. For the simulations where properties of porous medium vary with time, calculation of both geometric and fluid parts is performed at each time instant.

3.3 Solution Procedure

A proper method should be chosen in order to solve the discrete system of conservation laws for the reactive transport described by system (3.39). There are essentially two different approaches that might be used. The first approach is to preserve coupling between advection and reaction terms, which means no modifications to be introduced in the system of the conservation laws. This approach was used for our computations presented in Chapter 4, where equations were strongly coupled. Another approach is to split the system (3.39) into the pure advection problem, where only convective terms are considered, and the source problem, where only reactive source terms are considered [99]. A main advantage of splitting is that independent methods may be applied to solve each of the subproblems separately. The computations performed in Chapters 6 and 7 were based on the splitting approach.

Equation (3.39) can be rewritten in the following form:

$$\frac{d}{dt}\mathbf{U}_i = \mathbf{f}_i^{advect}(\mathbf{W}_j, t) + \mathbf{S}_i(\mathbf{W}_j) \equiv \mathbf{f}_i(\mathbf{W}_j, t), \quad i, j \in \mathcal{N} \tag{3.57}$$

$$\mathbf{f}_i^{advect} = V_i^{-1} \sum_{j \in \bar{\mathcal{N}}^{(i)}} (\vec{n} \cdot \vec{\mathbf{F}} A)_{ij} + \mathbf{Q}_i, \quad i \in \mathcal{N} \tag{3.58}$$

where $\mathbf{f}_i^{advect}$ is the convective term that combines the surface fluxes and the convective sources. According to the coupling approach, the solution is obtained by integrating the full system of equations (3.57). Splitting of the problem (3.57) is performed in the following way. For each time interval $t \in [t^n, t^{n+1}]$, the solution of the problem is obtained by the successive integration of the following advection problem

$$\frac{d}{dt}\mathbf{U}_i = \mathbf{f}_i^{advect}, \quad i \in \mathcal{N}, \quad t \in [t^n, t^{n+1}], \tag{3.59}$$

and the source problem

$$\frac{d}{dt}\mathbf{U}_i = \mathbf{S}_i, \quad i \in \mathcal{N}, \quad t \in [t^n, t^{n+1}] \tag{3.60}$$

Each of the equations (3.57), (3.59), (3.60) represents a system of ordinary differential equations which can be solved using common integration techniques. In our work, we make use of explicit and implicit Euler methods. A particular integration scheme may vary depending on, what variables **W** are treated implicitly and what are treated explicitly. The commonly applied approaches are [108]: the fully explicit method; implicit pressure, explicit saturations and explicit compositions (IMPESC) method; the fully implicit method (FIM). These approaches are explained below.

3.3.1 Temporal Integration

In our computations, we used explicit and implicit Euler methods to carry out the time integration of the ordinary differential equations representing the conservation laws. Both methods are first order accurate in time. The forward (or explicit) Euler method can be numerically unstable, especially in the case of stiff equations, which may result in unlimited growth of the numerical solution and oscillatory behavior [109].

Consider an ordinary differential equation for a vector variable **w** of the form

$$\frac{d}{dt}\mathbf{u}(\mathbf{w}) = \mathbf{f}(\mathbf{w}, t) \tag{3.61}$$

Variable **w** may represent the cell average values of a single primitive variable W or of a set of primitive variables. We assume that **w** has m components, the same number as the vector functions **u**: $\mathbb{R}^m \to \mathbb{R}^m$ and **f**: $\mathbb{R}^m \to \mathbb{R}^m$. Integration of equation (3.61) over time between the time instants $t = t^n$ and $t = t^{n+1} = t^n + \Delta t$ results in

$$\mathbf{u}^{n+1} - \mathbf{u}^n = \int_{t^n}^{t^{n+1}} \mathbf{f}(\mathbf{w}(t), t)dt \tag{3.62}$$

where $\mathbf{u}^n = \mathbf{u}(\mathbf{w}^n)$, $\mathbf{w}^n = \mathbf{w}(t^n)$.

3.3.1.1 Explicit Euler method

According to the forward, or the explicit Euler method, calculation of the time integral on the right-hand side of equation (3.62) is performed using the value of the vector function **f** at a time instant $t = t^n$:

$$\mathbf{u}^{n+1} - \mathbf{u}^n = \Delta t \cdot \mathbf{f}(\mathbf{w}^n, t^n) \tag{3.63}$$

The value of the primitive variable **w** at the time instant $t = t^{n+1}$ can then be determined from the set of algebraic equations

$$\mathbf{u}(\mathbf{w}^{n+1}) = \mathbf{u}^{n+1} \tag{3.64}$$

The forward Euler method should be applied with precautions. In the cases where the right-hand side of equation (3.63) is large, the value of $\mathbf{u}^{n+1}$ may change significantly and go beyond the physical limits. In order to prevent this behavior, it is required to decrease the time step Δt. This may limit the application of the explicit Euler method, as it becomes computationally ineffective if the time step is too small.

3.3.1.2 Implicit Euler method

According to the backward, or the implicit Euler method, calculation of the time integral on the right hand side of equation (3.62) is performed using the value of the vector function **f** at a time instant $t = t^{n+1}$:

$$\mathbf{u}(\mathbf{w}^{n+1}) - \mathbf{u}^n = \Delta t \cdot \mathbf{f}(\mathbf{w}^{n+1}, t^{n+1}) \tag{3.65}$$

In general, (3.65) represents a system of non-linear algebraic equations for the variable $\mathbf{w}^{n+1}$. Solution for the system (3.65) can be obtained using an iterative procedure. In our computations presented in Chapter 4 we implemented the multivariate Newton's method [110] to solve the governing system of equations that had the form of (3.65) (see description in the next subsection). A main advantage of the implicit Euler method is its stability. However, it is characterized by high numerical diffusion [109]. For this reason, even for fine grids the resulting solution does not reproduce sharp saturation and concentration fronts.

Multivariate Newton method

The multivariate Newton method is a generalization of the Newton-Raphson method onto multiple dimensions. In order to solve system (3.65), the residual function **g**: $\mathbb{R}^m \to \mathbb{R}^m$ is introduced:

$$\mathbf{g}(\mathbf{w}) \equiv \mathbf{u}(\mathbf{w}) - \mathbf{u}^n - \Delta t \cdot \mathbf{f}(\mathbf{w}, t^{n+1}) = 0 \tag{3.66}$$

The solution of the system (3.66) is obtained recursively. In our computations, the seed value $\mathbf{w}^{[0]}$ was given by $\mathbf{w}^n$ which is the value of variable at the time instant $t = t^n$. The solution approximation $\mathbf{w}^{[k+1]}$ at iteration k is obtained using

$$\mathbf{w}^{[k+1]} = \mathbf{w}^{[k]} - \mathbf{J}^{-1} \cdot \mathbf{g}(\mathbf{w}^{[k]}) \tag{3.67}$$

The iterations are repeated until the convergence criterion $\left\|\mathbf{w}^{[k+1]} - \mathbf{w}^{[k]}\right\| < \varepsilon_{tot}$ is fulfilled. The Jacobian matrix **J** of function $\mathbf{g}(\mathbf{w})$ is defined as

$$J(\mathbf{w})_{kl} = \frac{\partial g_k(\mathbf{w})}{\partial w_l}, \quad k,l = 1,\ldots,m \tag{3.68}$$

Calculation of the Jacobian **J** can be performed numerically. This is time costly, but allows more flexibility, so that numerical method can be applied to different problems without modification. Computation of the numeric Jacobian is performed according to

$$J(\mathbf{w})_{kl} = \frac{g_k(\mathbf{w} + \mathbf{e}_l) - g_k(\mathbf{w})}{\epsilon_l} \tag{3.69}$$

where $\mathbf{e}_l$ is the vector that introduces a small perturbation of the variables $\mathbf{w}$ such that the l^{th} component of $\mathbf{e}_l$ equal to ϵ_l and the rest are zero.

3.3.1.3 IMPESC method

The IMPES (and IMPESC) method is motivated by the observation that pressure waves travel much faster than saturation or concentration waves. The equation governing the evolution of pressure is elliptic or parabolic, and pressure propagates almost instantaneously through the domain. In the limiting case of incompressible fluids, the pressure wave travels with infinite velocity. Equations governing transport of fluids and species are hyperbolic, and corresponding saturation and concentration waves travel with finite velocities.

According to the IMPESC method, saturation and compositions are considered constant within the time step. Under this assumption, the material balance equations for the bulk phases are combined to obtain the pressure equation (3.30) that is used to compute pressure implicitly. The solution for the pressure is then used to calculate fluxes and perform an explicit update of the saturation and species concentrations.

3.3.2 Coupling Approach

In this section, we consider the coupling approach that was used for computations in Chapter 4. The system of discretized equations for the coupled reactive transport is given by (3.57). Simulations of the flow of compressible fluids in porous media, which properties vary in time and space, were performed in one dimension. The densities of the phases were considered to be functions of pressure and composition. Additionally, the compositions of the phases were affected by the undergoing chemical kinetic reactions with sufficiently high reaction rates. The best performance was achieved using the FIM.

Integration of the system (3.57) was performed using the backward Euler method, so that all the physical variables: pressure, saturation and compositions were updated implicitly. The matrix variable $\mathbf{W}_i$ of the size $n_{\mathbf{W}} \times N$ (N is the number of grid cells and $n_{\mathbf{W}}$ is the number of primitive variables) was transformed into the vector variable $\mathbf{w}$ with $m = n_{\mathbf{W}} \cdot N$ components by reordering:

$$\mathbf{w}\{(i-1)\cdot n_{\mathbf{W}} + 1,\ldots,i\cdot n_{\mathbf{W}}\} = \mathbf{W}_i, \quad i = 1,\ldots,N \tag{3.70}$$

The same applies to the matrix functions $\mathbf{U}_i$ and $\mathbf{f}_i$. As a result, the matrix equation (3.57) is transformed into a vector equation that has the form of (3.65) and is solved using the multivariate Newton's iterations.

The size of the Jacobian $\mathbf{J}$ is $m^2 = n_{\mathbf{W}}^2 \cdot N^2$. Most of the computations are performed during Newton's iterations, in order to calculate the inverse of the Jacobian. This limits direct

application of the backward Euler method in the case of a large number of variables and fine grids.

3.3.3 Splitting Approach

A motivation behind splitting, represented by equations (3.59), (3.60), is a possibility for optimal application of the developed integration schemes for each of the subproblems. Consider the reaction-advection problem on a time interval $t \in [t^n, t^{n+1}]$. The sequential approach can be illustrated as follows. First, a pure advection problem is considered and an intermediate solution $\bar{\mathbf{W}}_i^n$ is obtained:

$$\left.\begin{array}{l} \frac{d}{dt}\mathbf{U}_i(\mathbf{W}_j) = \mathbf{f}_i^{advect}(\mathbf{W}_j) \\ \mathbf{W}_i(t^n) = \mathbf{W}_i^n \end{array}\right\} \Rightarrow \bar{\mathbf{W}}_i^n = \mathbf{W}_i(t^{n+1}) \tag{3.71}$$

The initial condition for the advection problem is given by the values of primitive variables at the time instant $t = t^n$. The numerical solution for the advection problem is commonly obtained using the FIM, IMPESC or the fully explicit method. The fully explicit method can only be applied if calculation of the pressure is not required: for example, in the case of flow of incompressible fluids in one dimension.

As a second step, the source problem is considered and the solution $\mathbf{W}^{n+1}$ is obtained:

$$\left.\begin{array}{l} \frac{d}{dt}\mathbf{U}_i(\mathbf{W}_j) = \mathbf{S}_i(\mathbf{W}_j) \\ \mathbf{W}_i(t^n) = \bar{\mathbf{W}}_i^n \end{array}\right\} \Rightarrow \mathbf{W}_i^{n+1} \tag{3.72}$$

The intermediate solution $\bar{\mathbf{W}}_i^n$ for the advection problem is used as the new initial condition for problem (3.72). Computation of the reaction step represented by (3.72) can be performed using the explicit or the implicit method. The choice depends on the intensity of physicochemical interactions. For reactions characterized by slow reaction rates, the explicit method can be used, while for fast reactions one should choose the implicit method. In our computations, we have used the implicit method by means of Matlab® *fsolve* function (Chapter 6) and a solver from the Fortran *minpack* library [111] (Chapter 7).

A main drawback of the splitting approach is that even though it is possible to construct high order schemes, the method does not guarantee convergence to the exact solution [99]. However, the benefits of the methods prevail, so that it is widely applied in the reactive transport modeling.

3.4 Shock Capturing Numerical Scheme

In this section, we describe the second order accurate scheme that was used for the numerical modeling in Chapter 6. Below we consider for demonstration the flow of the incompressible fluids in one dimension.

3.4.1 Flow in One Dimension

The two-phase flow in one dimension represents a special case of the formalism introduced in Section 3.2. Each subdomain (cell) Ω_i is connected to the two neighboring cells Ω_{i-1} and Ω_{i+1}. Injection is performed into cell Ω_1 and production occurs from cell Ω_N. We assume that all the cell boundaries are coincident and $A_{ij} = const$. In the 1D case it is convenient to denote the boundary values $u_{i,i\pm1}$ as $u_{i\pm1/2}$. The advection-reaction problem reads:

$$\partial_t \mathbf{U}(\mathbf{W}) + \partial_x \mathbf{F}(\mathbf{W}) = \mathbf{S} \tag{3.73}$$

Discretized system of conservation laws (3.39) assumes the form

$$\frac{d\mathbf{U}_i}{dt} = -\frac{\mathbf{F}_{i+1/2} - \mathbf{F}_{i-1/2}}{\Delta x_i} + \mathbf{S}_i, \quad i \in \mathcal{N} \tag{3.74}$$

where $\mathbf{F}_{1/2}$ is the external flux to the first cell, and $\mathbf{F}_{N+1/2}$ is the outgoing flux from the last cell. For the flow of incompressible fluids in one dimension, the linear flow velocity u_t is constant and phase velocities are determined in terms of the fractional flow function:

$$u_\alpha = f_\alpha u_t \qquad u_a = c_a f_\alpha u_t \tag{3.75}$$

Pressure can be eliminated from the set primitive variables and $\mathbf{W} = [s, c_a, \sigma_b]^T$, $a \in \mathrm{B}_{sp}^{w}$, $b \in \mathrm{B}_{sp}^{surf}$.

3.4.2 MUSCL-Hancock Scheme

Construction of the high-order accurate schemes for the conservation laws is a subject of numerous books and publications [99, 101] and we cannot fully cover its application. Therefore, we briefly introduce the numerical technique applied in this work without going deeply into details. It is required to split the reactive transport model represented by (3.73) into pure advection problem:

$$\partial_t \mathbf{U}(\mathbf{W}) + \partial_x \mathbf{F}(\mathbf{W}) = 0 \tag{3.76}$$

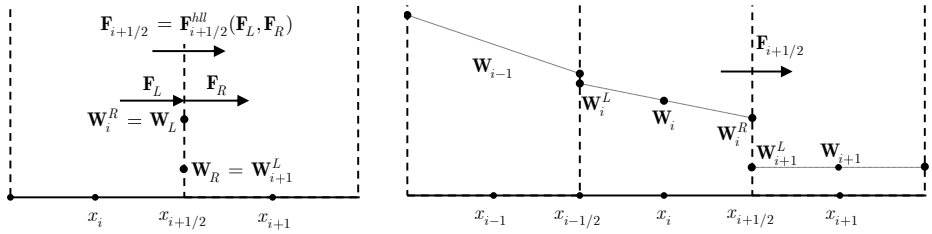

Figure 3.2: a) Schematic illustration of the flux calculation at the boundary according to HLL solver b) Schematic illustration of the reconstructed boundary values according to the MUSCL scheme.

and the source problem:

$$\partial_t \mathbf{U}(\mathbf{W}) = \mathbf{S}(\mathbf{W}) \tag{3.77}$$

The high order spatial accuracy is achieved by advanced calculation of the intercell fluxes, while the source problem is considered in the usual way. Hence, below we consider only the pure advection problem (3.76) and its discrete representation:

$$\frac{d\mathbf{U}_i}{dt} = -\frac{\mathbf{F}_{i+1/2} - \mathbf{F}_{i-1/2}}{\Delta x_i}, \quad i \in \mathcal{N} \tag{3.78}$$

In order to integrate (3.78) we use the Monotonic Upstream-Centered Scheme for Conservation Laws (MUSCL) in terms of primitive variables, known as the MUSCL-Hancock scheme. The numerical flux at the cell face $\mathbf{F}_{i+1/2}$ is calculated by solving the Riemann problem using the Harten, Lax, van Leer (HLL) approximate solver [99]:

$$\mathbf{F}^{hll}_{i+1/2} = \frac{S_R\mathbf{F}_L - S_L\mathbf{F}_R + S_L S_R(\mathbf{W}_R - \mathbf{W}_L)}{S_R - S_L} \tag{3.79}$$

Where $\mathbf{F}_L = \mathbf{F}(\mathbf{W}_L)$, $\mathbf{F}_R = \mathbf{F}(\mathbf{W}_R)$ and L and R indicate the state in the cell to the left and right of the cell face $x_{i+1/2}$ as shown in Figure 3.2a. S_L and S_R are the highest left and right wave speeds that are determined by the eigenvalues Λ_k of the flux Jacobian $\partial\mathbf{F}/\partial\mathbf{W}$.

$$S_L = \min_k(0, \Lambda_k^L, \Lambda_k^R), \quad S_R = \max_k(0, \Lambda_k^L, \Lambda_k^R) \tag{3.80}$$

In order to compute the numerical flux according to (3.79) it is necessary to reconstruct the left and the right states of the primitive variables at the cell faces: $\mathbf{W}_L$ and $\mathbf{W}_R$, respectively. This is achieved by considering the non-conservative form of the equation (3.76):

$$\partial_t \mathbf{W} + \mathbf{A}(\mathbf{W})\partial_x \mathbf{W} = 0 \tag{3.81}$$

where $\mathbf{A}(\mathbf{W}) = (\partial \mathbf{U}/\partial \mathbf{W})^{-1}(\partial \mathbf{F}/\partial \mathbf{W})$. Computation of $\mathbf{W}_L$ and $\mathbf{W}_R$ is performed in two steps:

- Step I: Data reconstruction. The values of primitive variables $\mathbf{W}$ are linearly extrapolated to the cell faces using limited slopes Δ_i:

$$\mathbf{W}_i^L = \mathbf{W}_i^n - 2^{-1}\Delta_i, \quad \mathbf{W}_i^R = \mathbf{W}_i^n + 2^{-1}\Delta_i \tag{3.82}$$

  where Δ_i is the slope vector of $\mathbf{W}_i(x)$ in cell i, and $\mathbf{W}_i^L$ and $\mathbf{W}_i^R$ are the values of the primary variables at the left and right faces of the cell (Figure 3.2b). The slope limiter Δ_i can be calculated using different slope limiter functions (e.g. *minmod*, *superbee*, *van Leer*) [99]. Its value is determined by the ratio of the successive gradients $\mathbf{r}_i$:

$$\mathbf{r}_i = \frac{\mathbf{W}_i^n - \mathbf{W}_{i-1}^n}{\mathbf{W}_{i+1}^n - \mathbf{W}_i^n} \tag{3.83}$$

- Step II: Evolution. For each cell, the boundary extrapolated values are explicitly evolved by the time $2^{-1}\Delta t$ according to the non-conservative equation (3.81)

$$\begin{aligned} \bar{\mathbf{W}}_i^L &= \mathbf{W}_i^L + \frac{1}{2}\frac{\Delta t}{\Delta x}\mathbf{A}(\mathbf{W}_i^n)[\mathbf{W}_i^L - \mathbf{W}_i^R] \\ \bar{\mathbf{W}}_i^R &= \mathbf{W}_i^R + \frac{1}{2}\frac{\Delta t}{\Delta x}\mathbf{A}(\mathbf{W}_i^n)[\mathbf{W}_i^L - \mathbf{W}_i^R] \end{aligned} \tag{3.84}$$

Algebraic manipulations allow combining Step I and Step II and write the left and the right states as follows [112]:

$$\begin{aligned} \mathbf{W}_L &= \bar{\mathbf{W}}_i^R = \mathbf{W}_i^n + \frac{1}{2}[\mathbf{I} - \frac{\Delta t}{\Delta x}\mathbf{A}(\mathbf{W}_i^n)]\Delta_i \\ \mathbf{W}_R &= \bar{\mathbf{W}}_{i+1}^L = \mathbf{W}_{i+1}^n - \frac{1}{2}[\mathbf{I} + \frac{\Delta t}{\Delta x}\mathbf{A}(\mathbf{W}_i^n)]\Delta_{i+1} \end{aligned} \tag{3.85}$$

where $\mathbf{I}$ is the identity matrix. These values are used to calculate the wave speeds S_L, S_R, and the numerical flux at the cell face according to equation (3.79). Finally, the fluxes $\mathbf{F}_{i+1/2}^{hll}$ are used to update the conserved variables $\mathbf{U}_i$ explicitly according to equation (3.78). It should be pointed out that, although primitive variables are used in the reconstruction and evolution steps (steps I and II), the final update is performed with the conservative variables, so that the resulting scheme is conservative.

We demonstrate the application of the MUSCL-Hancock scheme to the two test problems related to chemical flooding; continuous injection of chemical, and the slug injection. Comparison between the analytical solution for continuous injection (Chapter 2) and the two numerical solutions obtained using the upwind first order scheme and the MUSCL scheme

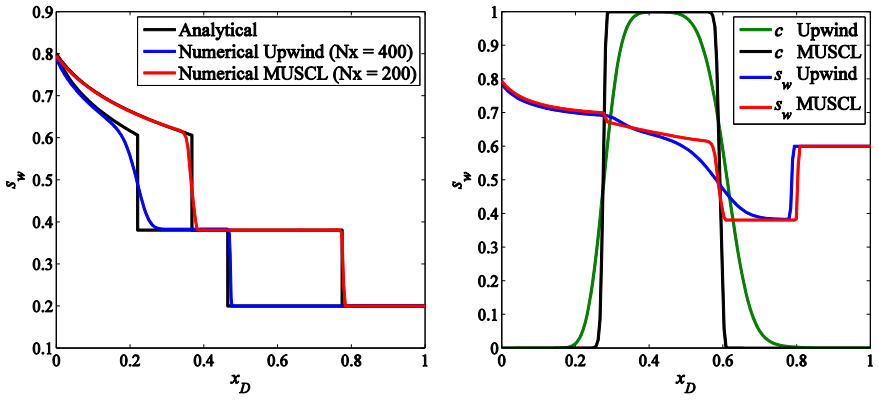

Figure 3.3: a) Comparison between analytical solution for the chemical flooding and numerical solution obtained with upwind scheme (Nx = 400 cells) and the MUSCL scheme (Nx = 200 cells). b) Comparison between the two numerical solutions for the chemical slug injection (Nx = 200 cells)

is shown in Figure 3.3a. The MUSCL scheme with $N = 200$ grid cells reproduces the analytical solution more accurately compared to the upwind scheme with $N = 400$. In Figure 3.3b we present the two numerical solutions for the problem of the chemical slug injection with equal numbers of gird cells $N = 200$ for the upwind and MUSCL schemes. Application of the MUSCL scheme is justified if computation of the source problem is time costly, since the scheme accurately reproduces shocks using a relatively small number of grid cells.

3.5 Conclusions

This chapter presents the approaches used for numerical modeling of the problems involving the coupled multiphase transport and geochemical interactions. The governing system of equations is represented by a set of material balance equations for the phases and chemical species. This system of conservation laws is discretized using the finite volume method. Spatial accuracy of the numeric scheme is determined by an approach used to calculate fluxes. The first order accurate schemes are easy to obtain using the two point flux approximation and the upwind scheme. The schemes of the second order of accuracy can be obtained as a result of sophisticated calculation of the cell fluxes. An advantage of the high order methods is their ability to reproduce accurately shocks using a small number of discrete elements.

Integration of the ordinary differential equations representing the discrete formulation of the conservation laws can be performed in two ways: by preserving coupling between the advection and reaction terms, and by the splitting approach. Application of the splitting approach is convenient, since it simplifies the numerical model and makes computations more efficient by applying appropriate independent numerical methods to describe the flow and the production mechanisms.

4

Modeling of Dissolution Effects on Waterflooding

4.1 Introduction

Analysis of coupling of flow and chemical reactions between fluids and porous medium is an area of interest for many scientific, industrial and engineering processes. A considerable research is currently focused around injection of the chemistry optimized water by tuning the salinity and ionic composition in order to increase the recovery [5, 113, 114]. This process involves a large number of physicochemical interactions, which were partially covered in Chapter 2. Among others, dissolution and precipitation are two important processes affecting brine chemistry as they can significantly modify the physical and chemical properties of porous media [115-118]. Some of the experimental data [36, 119] support the fact that mineral dissolution takes place during smart water floods and, therefore, its effect should be quantified.

Similar studies have previously been carried out under the assumption that the fluid was incompressible [120]. The compressibility of the crude oil-brine-rock system might, however, be of importance. Both pressure and brine composition (salinity) affect the brine density. The compositional compressibility may be larger than pressure compressibility. At the same time, the dissolution may occur under the condition of volumetric disbalance (the individual volumes of dissolved species will be different from those in the solid state). Thus, dissolution of a mineral is accompanied by a volume change and a corresponding pressure adjustment. These changes are probably small, but they may play some role in a confined space. To account for this effect an equation of state for brine is required. It can be obtained from the experimental data on the density of electrolyte solutions, available for the specific ion content of the brine [121, 122].

In this Chapter, a 1D numerical model for two-phase compressible flows with chemical reactions is presented. An example of such a process is an injection of a weak acid or carbonated water in a reservoir. A key feature of the model is its capacity to account for the strong coupling between the fluid flow and mineral reactions that cannot be analyzed separately. It has turned out that volumetric non-additivity and considerable mass transfer between phases represent a problem for numerical simulations. Only a fully implicit scheme seems to be capable of accounting for this effect in the full scale. Therefore, this study was

an important step for us to establish a reliable numeric scheme for further applications in our research.

The structure of this Chapter is as follows. In the first section, we formulate the modifications that were introduced to the general model for reactive transport described in Chapter 3 and present the closed system of governing equations. The second section is devoted to the numerical model and its implementation. In the third section, we describe the results of numerical simulations. We analyze the changes in reservoir properties introduced by dissolution, together with the composition of produced water, pressure distribution, and saturation profiles.

4.2 Model Description

The approach applied in this work is based on the macroscopic approximation of mechanics of continuous medium, as described in Chapter 2. We consider porous medium initially saturated with oil and connate water in thermodynamic equilibrium. The rock may be composed of a number of minerals, which are sensitive to the injected brine composition. Injection of brine is performed to displace oil, which disturbs the thermodynamic equilibrium. Namely, the presence of active components in brine causes dissolution and/or precipitation of minerals. If these processes are intense, they are expected to influence both flow and reservoir parameters, such as porosity, absolute permeability, residual oil saturation and, possibly, relative permeability curves. An important difference from similar approaches used in other studies (e.g. Aharonov et al. [120]) is that we consider a two-phase flow of compressible fluids. Below we describe the modifications that were introduced in the general reactive transport model, based on the system of conservation laws presented in Chapter 3.

4.2.1 Mineral Dissolution and Precipitation Reactions

We study non-equilibrium mineral dissolution and precipitation reactions that take place at the interface between the water and mineral surface. According to classification introduced by Rubin [123] these reactions are referred as “insufficiently fast” heterogeneous surface reactions. The general form of dissolution/precipitation reactions of mineral m is represented by:

$$\mathrm{X}_m \rightleftarrows \sum_{a=1}^{n_{aq}} \nu_a^m \mathrm{X}_a \qquad m = 1,\dots,n_m \tag{4.1}$$

Variations of molar amounts of aqueous species are related to the mineral reaction rate $\dot{r}_m$ via the matrix of the stoichiometric coefficients ν_a^m:

$$S_a = \sum_{m=1}^{n_m} \nu_a^m \dot{r}_m \quad a = 1,\ldots,n_{aq} \tag{4.2}$$

The rate law for mineral dissolution and precipitation reaction is given by [49]:

$$-\partial_t C_m = \dot{r}_m = \hat{A}_m \; k_m^f \prod_{a=1}^{n_{aq}} (c_a')^{(|\nu_a^m| - \nu_a^m)/2} - k_m^b \prod_{a=1}^{n_{aq}} (c_a')^{(\nu_a^m + |\nu_a^m|)/2} \tag{4.3}$$

where $\hat{A}_m$ is the reactive specific surface for mineral reaction, k_m^f, k_m^b include rate constants and activity coefficients, C_m is the global mineral molar concentration (per bulk volume of the rock) and c_a' are the molar concentrations of the aqueous components divided by some reference concentrations c_a^{ref}.

4.2.2 Fluid Properties

Dissolution of external species in water affects its density. Moreover, the individual molar volumes of these species may change leading to the forced expansion/contraction of the aqueous phase. Variation of the aqueous phase density due to change in composition is commonly much larger compared with compressibility due to pressure change. Thus, certain pressure effects may arise to adjust for the change in density caused by physical-chemical interactions between the rock and aqueous phase. The model of weakly compressible fluid for water phase is modified by introducing an additional dependence of density on the composition of water. A problem of constituting the equation of state for brines was discussed in [121], where the data for modeling densities of electrolyte solutions is provided. In accordance with this data, we introduce a linearized equation of state for brine in the following form:

$$\rho_w(P, \mathbf{c}) = \rho_w^0 \; 1 + \hat{c}_{P,w}(P - P^0) + \sum_{a=1}^{n_{aq}} \hat{c}_{wc,a}(c_a - c_a^0) \tag{4.4}$$

with constant compressibilities $\hat{c}_{P,w}$, $\hat{c}_{wc,a}$ with regard to pressure and composition correspondingly, P^0 and c_a^0 represent the chosen reference state.

The dependence of the density on the amount of solute at constant pressure can be established using the following simple model. Consider a single mineral m of mass m_m, dissolved in pure water of a mass m_w. If the individual volumes are additive, the volume of the solution is calculated according to

$$V_{add} = V_w + V_m = \rho_w^{-1} m_w + \rho_m^{-1} m_m \tag{4.5}$$

Assuming that the mass of the mineral in much less than the mass of water, $m_w \ll m_w$, the density of the solution is calculated according to

$$\rho_{add} = \frac{m_m + m_w}{V_{add}} = \rho_w^0 \frac{1 + m_m / m_w}{1 + (\rho_w^0 m_m) / (\rho_m m_w)} \approx \rho_w^0 \left(1 + (1 - \frac{\rho_w^0}{\rho_m}) \frac{m_m}{m_w} \right) \quad (4.6)$$

Non-additivity of individual volumes may be accounted via parameter γ reflecting the change of the volume of mineral in dissolution: when volume V_m gets dissolved it becomes $V_m(aq) = (1+\gamma)V_m$. Thus, $\gamma < 0$ corresponds to overall decrease and $\gamma > 0$ to an increase in the volume of the mixture compared to the sums of initial volumes:

$$V_{non-add} = V_{add} + \gamma V_m \quad (4.7)$$

$$\rho_{non-add} = \frac{m_m + m_w}{V_{non-add}} \approx \rho_w^0 \left(1 + (1 - (1+\gamma) \frac{\rho_w^0}{\rho_m}) \frac{m_m}{m_w} \right) \quad (4.8)$$

This simple consideration shows that for small concentrations of solute, compressibility due to change in composition of the brine can be successfully calculated by the following dependence

$$\hat{c}_{wc,a} = 1 - (1 + \gamma_m) \rho_w / \rho_m \quad (4.9)$$

where coefficient γ_m is the relative change in molar volume on the dissolution of mineral m.

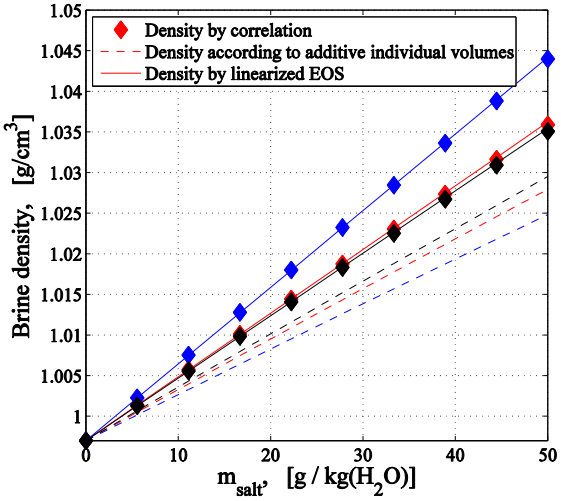

Figure 4.1: Comparison of densities of brine with dissolved $CaCO_3$ (red), $MgCO_3$ (black) and $CaSO_4$ (blue) calculated from correlations [122], additive mixing and linearized EOS (4.4)

Comparison of the brine density correlations from the work of Lam et al. [122] and the additive mixing rule (4.6) for calcite ($CaCO_3$), magnesite ($MgCO_3$) and anhydrite ($CaSO_4$) is shown in Figure 4.1. The difference between the densities according to additive mixing and correlations exceed 10% for all the substances and is around 40% for $CaSO_4$. We calculated the parameters γ_m by fitting the brine density correlations [122] with the linearized EOS (4.4). The calculated values were found to be: $\gamma_{CaCO_3} = -0.42$, $\gamma_{MgCO_3} = -0.32$, $\gamma_{CaSO_4} = -0.875$. Thus, the negative excess volumes are observed.

Finally, the density of oil was set to be a function of pressure only:

$$\rho_o(P) = \rho_o^0 \ 1 + \hat{c}_{P,o}(P - P^0) \tag{4.10}$$

4.2.3 Rock Properties

The properties of the rock, such as porosity, permeability, and specific surface, are to be related to reservoir pressure and mineral content. If the reservoir pressure has a significant effect on the state of the rock then an appropriate geomechanical model should be included in the reactive transport [124]. Most of the models use the pressure-dependent compressibility of rock to approximate the geomechanical effects on porosity and permeability. The water-weakening of the rock may also result in fracturing. The question of the appropriate geomechanical model is to be considered for each type for the rock separately and is beyond the scope of this study. We limit consideration only to the variation of porosity and permeability.

With the assumption that pressure does not affect the state of the rock it is possible to relate the porosity and the amounts of mineral species present:

$$\phi = \phi^0 - \sum_{m=1}^{n_m} \rho_m^{-1} M_m (C_m - C_m^0) \tag{4.11}$$

where ϕ^0 is homogeneous initial porosity, ρ_m is the mineral density and M_m is the molar weight.

The relation between the absolute permeability k and the microgeometry of pore space is important for modeling nonlinear processes involved in the study. Permeability is commonly assumed to be a power law function of the porosity and specific surface $\hat{A}$ in $\mathrm{m}^2/\mathrm{l(core)}$. In our study, we use the conventional Kozeny-Carman equation [125], which is successfully applied to predict permeability of chalks [126]

$$k = c_K \frac{1}{\hat{A}^2} \frac{\phi^3}{(1-\phi)^2} \tag{4.12}$$

where c_K is constant. The specific surface $\hat{A}$ is, in general, a complex function that depends on the porosity ϕ, pore-size distribution and whether a mineral is dissolving or depositing. However, due to the lack of general models of this kind of dependence the specific surface $\hat{A}$ is approximated as constant.

Aside from porosity and permeability, reactive surface $\hat{A}_m$ is another important parameter in the calculation of the rate of mineral dissolution and precipitation. The following equation is used to calculate the reactive surface are with the change of moles of minerals:

$$\hat{A}_m = \hat{A} \cdot (C_m \,/\, C_m^0) \tag{4.13}$$

This dependence describes a layer of mineral on the surface, and, therefore, the reactive area decreases as the mineral is dissolved and vice versa. The real dependence is expected to be more complicated and also includes relation to the saturation of the porous media as, in general, only part of the rock surface is in direct contact with water while the other part is covered with oil. Thus, using equation (4.13) we assume that porous media is completely water-wet, and invading water has access to the whole surface of the rock, including oil filled pores. This can be achieved if the invading water can effectively penetrate the wetting films on the surface of the rock. Alternatively, the dependence of the effective area on saturation may be introduced. We do not consider it in this study.

We also assume that while the rock is getting dissolved, the total amount of residual oil does not change. This automatically implies the variation of the residual oil saturation s_{or}, as it is related to the pore volume. One can deduce, therefore, that

$$s_{or} = s_{or}^0 \cdot (\phi^0 \,/\, \phi) \tag{4.14}$$

Therefore the residual oil saturation decreases on dissolution and increases during precipitation process, whereas the total mass of the trapped oil per bulk volume $\phi s_{or} \rho_o$ remains the same.

4.2.4 Closed System of Material Balance Equations

The modification of the reservoir and fluid parameters described in the preceding sections are introduced in the general system of the conservation laws presented in Chapter 3. The transport of phases is governed by the generalized Darcy laws with Corey-type relative permeabilities introduced in Chapter 2. Therefore, it is possible to formulate the system of equations governing the reactive transport in one dimension, which includes the material balance equations for the phases

water: $$\partial_t(\phi s\rho_w) - \partial_x(k\rho_w\lambda_w\partial_x P) = \sum_{a=1}^{n_{aq}} M_a S_a \ , \tag{4.15}$$

oil: $$\partial_t(\phi(1-s)\rho_o) - \partial_x(k\rho_o\lambda_o\partial_x P) = 0 \ , \tag{4.16}$$

rock: $$\partial_t((1-\phi)\rho_s) = -\sum_{m=1}^{n_m} M_m \dot{r}_m \ , \tag{4.17}$$

aqueous species:

$$\partial_t(\phi s c_a) - \partial_x(k c_a \lambda_w \partial_x P) = S_a \quad a = 1,...,n_{aq} \ , \tag{4.18}$$

and mineral species:

$$\partial_t C_m = -\dot{r}_m \quad m = 1,...,n_m \ . \tag{4.19}$$

where $\lambda_\alpha = k_{r\alpha}/\mu_\alpha$ are the phase mobilities relating the pressure gradient and the linear flow velocity according to the following equation

$$u_t = -k(\lambda_w + \lambda_o)\partial_x P \tag{4.20}$$

Material balance equation for the rock (4.17) may be omitted, due to the fact that porosity is uniquely related to mineral concentrations via the equation (4.11). Thus, the set of primary variables includes pressure P, saturation s, concentrations of aqueous and mineral species c_a and C_m respectively. Equations (4.15)–(4.19) are combined with the closure relations obtained in preceding sections, namely (4.2) and (4.3) for the mass transfer rates, (4.4) and (4.10) for densities of the brine and oil, equation (4.11) for porosity and equation (4.12) for absolute permeability. Finally, the mobilities λ_α are determined through Corey-type relative permeability functions that account for the change in residual oil saturation according to the equation (4.14).

The system of material balance equations is to be supplemented with the initial and boundary conditions. We assume initially homogeneous porous medium saturated with oil at formation water (FW) at irreducible water saturation, so that initial values of primary variables are:

$$s(t=0,x) = s_{wi}, \quad P(t=0,x) = P^0, \tag{4.21}$$

$$c_a(t=0,x) = c_a^{FW} \quad a = 1,...,n_{aq}, \tag{4.22}$$

$$C_m(t=0,x) = C_m^0 \quad m = 1,...,n_m \tag{4.23}$$

Our choice of boundary conditions at the inlet corresponds to the injection of brine with fixed composition at a constant injection rate:

$$u_t(t, x = 0) = u_t^0 \,, \tag{4.24}$$

$$c_a(t, x = 0) = c_a^{INJ} \quad a = 1,...,n_{aq} \,, \tag{4.25}$$

while at the outlet it is sufficient to specify pressure

$$P(t, L) = P^0 \tag{4.26}$$

4.2.5 Bringing the Equations to a Dimensionless Form

In order to obtain a dimensionless form of the system, we introduce the characteristic length of between the inlet and outlet L. The characteristic pressure drop is determined via the approximate Darcy law:$\Delta P = \mu_w u_t^0 L/k^0$. The dimensionless variables are defined as follows:

$$x_D = \frac{x}{L}, \quad t_D = \frac{U^0}{L\phi^0} t \tag{4.27}$$

$$P' = \frac{P}{\Delta P}, \quad c_a' = \frac{c_a}{c_a^{ref}}, \quad C_m' = \frac{C_m}{C_m^0} \tag{4.28}$$

$$\rho_\alpha' = \frac{\rho_\alpha}{\rho_w^0}, \quad \mu_\alpha' = \frac{\mu_\alpha}{\mu_w}, \quad \phi' = \frac{\phi}{\phi^0}, \quad k' = \frac{k(\phi)}{k(\phi^0)} \tag{4.29}$$

$$r_m' = \frac{\dot{r}_m}{\hat{A} k_m^f} \quad m = 1,...,n_m \tag{4.30}$$

The reference values for the molality of aqueous components are usually taken to be 1 mol/kg(H_2O) which is approximately the same as c^{ref} = 1 mol/l. We use this value for all the aqueous components. The dimensionless time t_D is measured in multiples of pore volumes injected, determined with regard to the initial pore volume, as the pore volume will change with dissolution/precipitation.

The resulting dimensionless system of equations to be solved assumes the form:

$$\partial_{t_D}(\phi' s \rho_w') - \partial_{x_D}(k' \rho_w' \lambda_w \partial_{x_D} P') = \sum_{m=1}^{n_m} \mathrm{Da}_m \cdot C_m' r_m' \,, \tag{4.31}$$

$$\partial_{t_D}(\phi'(1-s)\rho_o') - \partial_{x_D}(k'\rho_o'\lambda_o\partial_{x_D}P') = 0 \ , \tag{4.32}$$

$$\partial_{t_D}(\phi' s c_a') - \partial_{x_D}(k' c_a'\lambda_w\partial_{x_D}P') = \sum_{m=1}^{n_m} \mathrm{Da}_m \cdot \nu_{am} \frac{\rho_w^0}{c_a^{ref} M_m} \cdot C_m' r_m' \ , \tag{4.33}$$

$$\partial_{t_D} C_m' = -\mathrm{Da}_m \frac{\phi^0 \rho_w^0}{M_m C_m^0} C_m' r_m' \quad m = 1,...,n_m \, . \tag{4.34}$$

where Da_m is the Damköhler number, a dimensionless control parameter for the advection-reaction problem which we define as

$$\mathrm{Da}_m = \frac{L k_m M_m \hat{A}_m^0}{\rho_w^0 u_t^0} \quad m = 1,...,n_m \tag{4.35}$$

There are different ways in the literature to define the Damköhler number [120]. However, the introduced value has a similar physical meaning: it compares the characteristic times of the convective flow and the chemical equilibration. This ratio is useful to determine whether the advection rates or reaction rates determine the distribution of aqueous components in the system. For very small Damköhler numbers ($\mathrm{Da} \ll 1$), advection occurs much faster than reaction and thus the distribution of components is very similar with the distribution of inert tracer in water. At very high Damköhler numbers ($\mathrm{Da} \gg 1$) the reaction in almost instantaneous, the equilibrium concentrations are achieved before the flux redistributes the components. The intermediate values of Damköhler number are of particular interest, as they represent the behavior of non-idealized systems. It should also be noted that for intermediate values of Da the reaction terms on the right-hand side of the material balance equation for water cannot be neglected.

Comparing the Damköhler number for the same reaction taking place during reservoir flooding and core flood experiments in a similar rock, it can be seen from the equation (4.35) that the only parameters to change are the length and the linear flow velocity. Applying the characteristic values we obtain:

$$\frac{\mathrm{Da}_{m\ \ res}}{\mathrm{Da}_{m\ \ lab}} = \frac{L_{res}}{L_{lab}} \times \frac{u_{t,lab}^0}{u_{t,res}^0} \approx \frac{100\ [\mathrm{m}]}{0.1\ [\mathrm{m}]} \times \frac{10^{-5}\ [\mathrm{m/s}]}{10^{-6}\ [\mathrm{m/s}]} = 10^4 \tag{4.36}$$

This simple estimation indicates that at reservoir conditions reactions will exhibit behavior more similar to equilibrium chemical reactions while under laboratory conditions chemical kinetics is usually to be taken into account.

4.3 Numerical Model

In order to establish a numerical scheme for the presented model, we use the finite volume formulation as it was described in Chapter 3. The flux between the two neighboring elements is computed using the two point flux approximation (TPFA). In this case, it is required to compute geometric parts of the transmissibilities at each time step due to changing absolute permeability.

4.3.1 Solution Procedure

Initially, our approach was based on the usage of the fully explicit method. Masses of phases and components were updated at the first step, and the subsequent step was to calculate the pressure and saturation using the constraint that the sum of all phase volumetric fractions should be equal to one. However, this approach demanded an extremely small time step, in order to avoid large changes in pressure. We also tried several other ways of discretization, making the different variables or their combinations implicit. However, only the fully implicit scheme seems to really work and produce stable results. This method is computationally costly per unit step. However, due to better stability it allows for significantly larger time stepping, making time integration more efficient. We believe that the conventionally used operator splitting method allowing splitting the integration of the equations into two steps is not applicable because of the dependence of density on both pressure and composition.

One of the disadvantages of the fully explicit method is the high numerical diffusion. For this reason, even for fine grids the resulting solution does not reproduce sharp saturation and concentration fronts. For this study, we considered 300 finite volume cells, which produced sufficient resolution for comparison between simulations with different parameters.

4.4 Simulation Results

The described model was used to study waterflooding with mineral dissolution. In this simulation dissolution of a single mineral component and two aqueous components were considered. The two aqueous components represent the active solute X_S in the water, causing the dissolution, and a complex X_C which is a combined excess of dissolution reaction so that stoichiometry of the reaction can be represented by

$$X_m + X_S \rightleftarrows X_C \tag{4.37}$$

The necessary fluid properties are listed in table Table 4.1.

Table 4.1: Fluid properties for the sample study on mineral dissolution.

Density	Viscosity	Residual saturation	Endpoint rel. perm.	Corey exponent
$\rho_w^0 = 1.0\,\mathrm{kg/l}$	$\mu_w = 1\,\mathrm{cP}$	$s_{wi} = 0.2$	$k_{rwor} = 0.8$	$n_w = 2.0$
$\rho_o^0 = 0.8\,\mathrm{kg/l}$	$\mu_o = 3\,\mathrm{cP}$	$s_{or}^0 = 0.3$	$k_{rowi} = 0.5$	$n_o = 1.5$

The initial amount of the mineral in place C_m^0 determines the ultimate change in porosity. In our simulation, we assumed that the initial porosity $\phi^0 = 0.2$, and the dissolution of the mineral can result in porosity increase up to $\phi_{\max} = 0.3$, when all the mineral is dissolved. The corresponding volumetric fraction of the dissolvable mineral can be estimated as 12.5% of the initial reservoir rock. The model was tested for a number of control parameters:

$$\begin{aligned} \mathrm{Da} &= (0.01;\ 0.03;\ 0.1;\ 1.0;\ 10.0) \\ \gamma_m &= (0;\ \ \pm 0.25;\ \ \pm 0.4) \\ \hat{c}_{P,\alpha} &= (0.5\times 10^{-10};\ 0.5\times 10^{-8})[\mathrm{Pa}^{-1}] \end{aligned}$$

Our results indicate that rock dissolution affects mainly porosity, absolute permeability and, hence, pressure drop over the region of dissolution. Porosity and permeability variation with time are shown in Figure 4.2 for slow reactions and in Figure 4.3 for fast reactions. Varying the Damköhler number Da, we were able to observe different scenarios. The main difference between the two scenarios is that for slow reactions the chemical equilibration length is larger than the system size so that dissolution spans over the whole system (Figure 4.2). Meanwhile, for fast reactions the reaction is localized in a narrow region of dissolution with the formation of the dissolution front (Figure 4.3). Qualitative behavior of porosity and permeability is similar, and the main difference is in the magnitude of variation.

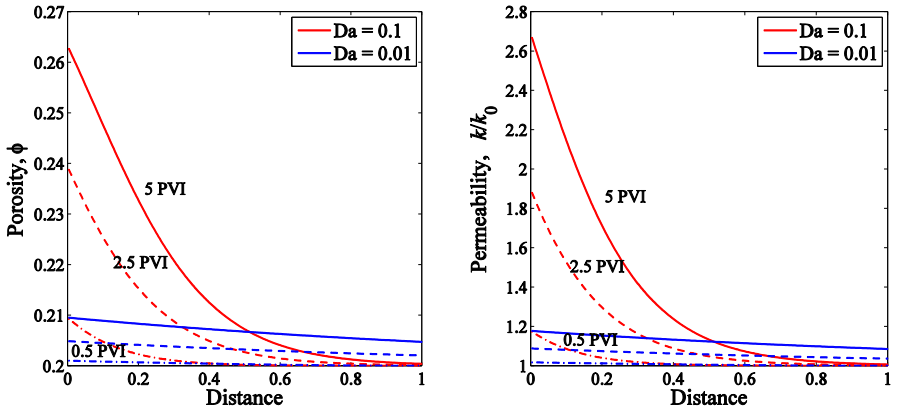

Figure 4.2: Porosity and permeability profiles for slow dissolution at different injection times.

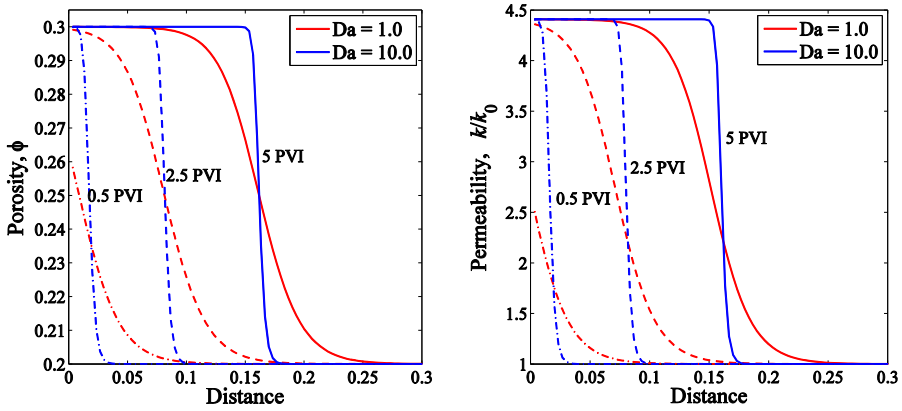

Figure 4.3: Porosity and permeability profiles for fast dissolution at different injection times.

The pressure distribution is visualized in Figure 4.4. The pressure drop is visibly altered behind the dissolution front. No additional effects on pressure due to volumetric non-additivity of dissolution process were observed. For a homogeneous reservoir at late times the pressure distribution is almost linear. For slow reaction rates the pressure distribution is represented by a smooth convex curve, in correspondence with the gradually varying permeability of the rock. For fast reaction rates, the pressure distribution is nearly piecewise-linear, corresponding to the heterogeneity of reservoir permeability on the different sides of the dissolution front.

The behavior of porosity, permeability, and pressure for high reaction rates is shown in Figures 4.3, 4.4. It may be interpreted as formation of wormholes close to the inlet. However, the evidence for this process, based solely on porosity and permeability variation, is indirect. A more detailed study of wormhole formation would require three-dimensional simulations.

Dissolution also affects saturation profiles in the reservoir rock. The most noticeable effect is an increase in water saturation close to the inlet caused by the fact that dissolution provides additional porous space for the injected fluid. Figure 4.5 illustrates that residual oil saturation s_{or} changes during the dissolution. This, however, does not imply any increment in recovery, as residual saturation is a volumetric factor, which changes solely due to increasing pore volume while the overall volume and mass of the trapped oil remain the same.

The displacement fronts propagate with slightly different rates in the cases of fast or slow dissolution. This effect is very small and occurs due to volumetric non-additivity (see Figure 4.5). In the case of negative volumetric effect ($\gamma_m < 0$), the combined volume of water plus dissolved species is smaller than the combined volume of water plus original mineral. Hence, dissolution creates additional volume for the brine to occupy and requires injecting more fluid in order to compensate for this additional volume. This results in a lower displacement

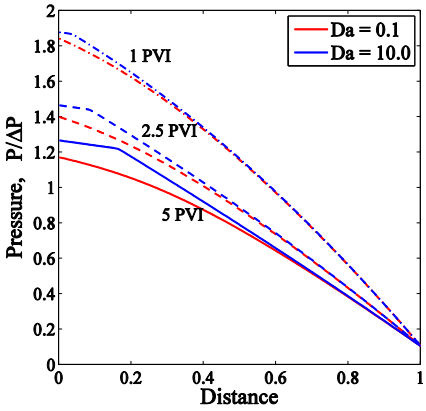

Figure 4.4: Pressure profiles in case of fast and slow dissolution reactions at different injection times.

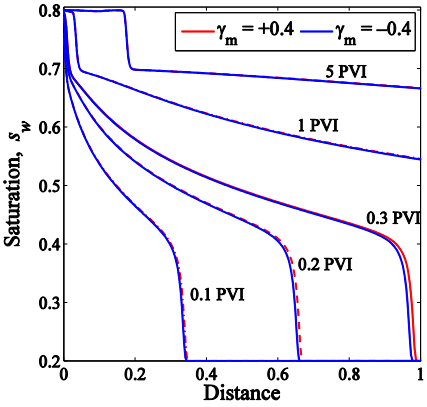

Figure 4.5: Saturation profiles in case of fast dissolution with positive and negative volumetric effects at different injection times.

front velocity. In the opposite case ($\gamma_m > 0$) velocity of the displacement front slightly increases.

Propagation of concentration fronts of aqueous components is shown in Figures 4.6, 4.7. The solute is gradually consumed as it propagates through the porous medium. Depending on the rates of this consumption, determined by the Damköhler number, the effluent concentration at the component breakthrough (the time when the components in the injected water will reach the effluent) will vary as illustrated in Figure 4.8. For higher reaction rates, the solute will be retarded at the effluent and produced only after many pore volumes of injection (Figure 4.6c, d). It will not be able to penetrate far from the inlet until complete dissolution of the mineral. Thus, almost all the injected solute is consumed during the dissolution.

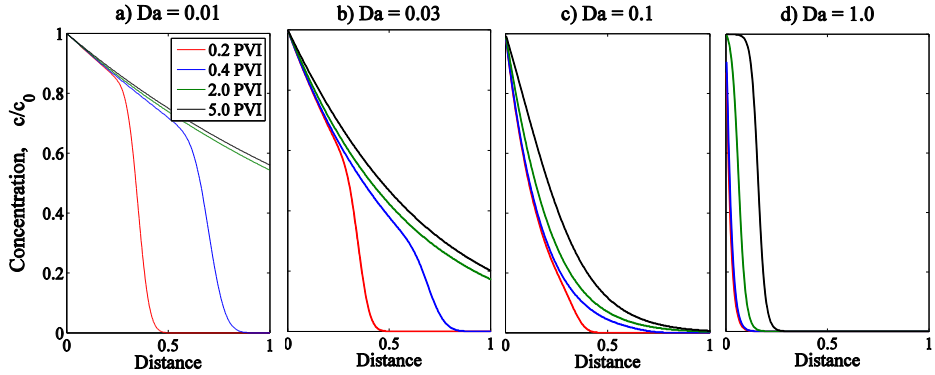

Figure 4.6: Active solute concentration profiles for different Damköhler numbers.

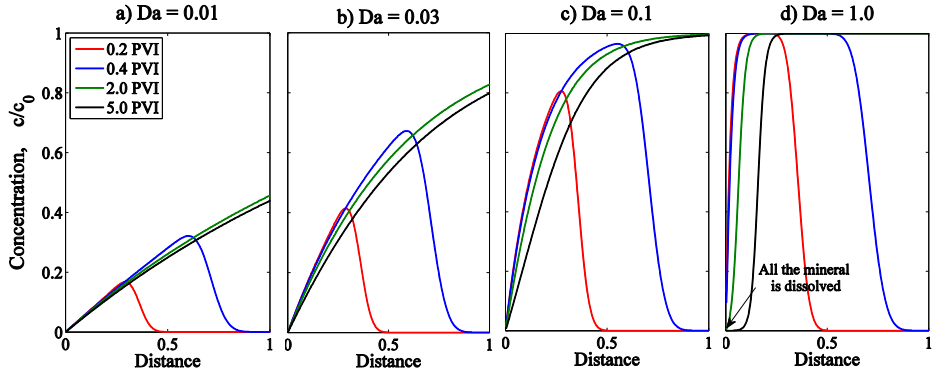

Figure 4.7: Complex concentration profiles for different Damköhler numbers.

Figure 4.7 illustrates how the complex is produced and washed away by the injected water. Similarly to the solute, the concentration of complex at the effluent will be determined by the value of the Damköhler number. Due to the absence of diffusion and other possible interactions, the sum of the two concentrations is equal to 1. At large Da we can also observe that the entire available mineral was dissolved in a region close to the inlet after 5 PVI of injection. The effluent concentrations of the solute for low Da are illustrated in Figure 4.8. For larger Da, the effluent concentration will be identical, showing itself in a rapid increase from 0 to 1 at the component breakthrough.

4.5 Conclusions

We developed a 1D numerical model for two-phase multicomponent flow in porous media accounting for non-equilibrium dissolution and pressure-compositional compressibility of

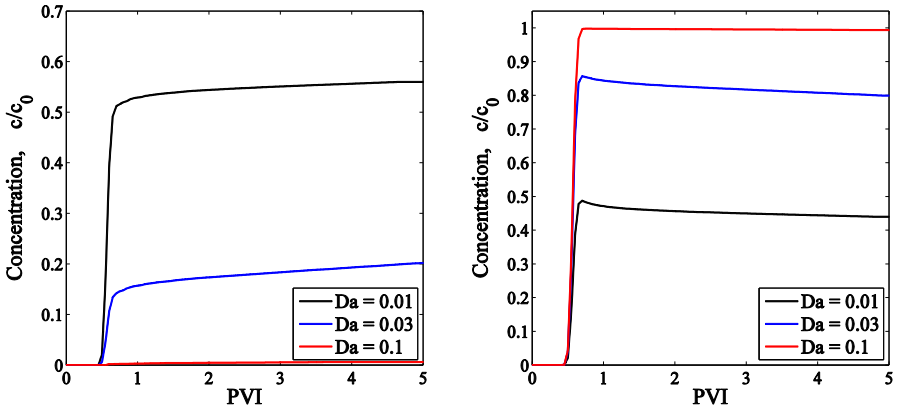

Figure 4.8: Effluent concentrations of (Left) active solute and (Right) complex in the produced brine for different Damköhler numbers.

the fluids. Study of the volumetric disbalance in the course of rock dissolution indicates that the effect may be rather large (the disbalance ratio γ_m is negative and is down to -0.8). The governing continuum-scale equations are solved using a fully implicit scheme. The governing equations are strongly coupled and need to be solved simultaneously, which excludes a possibility for application of explicit or time-splitting methods. Only the fully implicit scheme is capable of solving such a system.

The results of numerical modeling provide a qualitative description of the effect of mineral dissolution on waterflooding. Volumetric non-additivity affects the displacement process. The effect is that the velocity of the displacement front is slightly changed. We can see an increase in the front velocity in case of the positive volumetric effect (volume of mineral on dissolution increases) and decrease in the velocity for the negative volumetric effect. The change of mineral volume on dissolution does not affect the pressure in the system but affects the local pressure gradient.

If the reaction rates are sufficiently high, the variation of permeability and porosity close to the injection site resembles wormhole formation. Stronger effects are expected to be observed in the multidimensional flows, which are a subject of a separate study.

We conclude that non-additivity of volumes and compositional dependence of brine density does not have a significant effect on the flow. Dissolution and precipitation of minerals seem to be more important by their effect on the absolute values of concentrations of aqueous components during their propagation through the porous medium. Higher reaction rates and lower injection rates (higher reaction to advection mass transfer ratio) are likely to have a strong effect on the change of the brine composition during its flow in porous media.

5

Micromodel for Two-Phase Flow in Porous Media

5.1 Introduction

In this Chapter, we address the micromodel for simultaneous flow of water and oil on the pore scale. The pore space of the rock is characterized by a complex geometry. In order to take into account its effect on the flow of fluids in porous media, pore-network models may be used [127]. According to this approach, the porous medium can be effectively represented as a disordered 3D network constructed of pore bodies.

Pore-network models may be considered as a bridge between the flow at the microscale and macroscopic displacement. These models take into account the geometry of the pore space and flow patterns obtained for separate pore bodies depending on the different fluid configurations [128, 129]. Based on this data pore-network models allow predicting the transport properties of the rocks and retaining relative permeability curves [130]. The obtained relative permeability curves can then be applied to describe two-phase flow on the macroscale. This scheme is, of course, idealized. However, we think that establishing relations between micro- and macroscale phenomena is important to improve our understanding of flow in porous media.

In this study, we consider two-phase flow in angular capillaries. This choice of the shape allows both fluids to be present simultaneously in a capillary [131]. Therefore, it is expected that the fluids will mutually influence each other during the flow. We consider several governing parameters to see its effect on the flow; among them are the ratio of fluid viscosities, boundary conditions at the interphase boundary, and different pressure gradients in the fluids driving the flow. Of particular interest is the possibility for the flow of one fluid to induce the flow of another due to action of viscous forces at the interface between the phases. For a strongly water-wet system, it is also possible that a water film is formed on the surface of the pore body, and its effect on the flow should also be estimated.

The structure of this Chapter is as follows. In the next section, we present the general description of triangular capillary and possible fluid configurations. In Section 5.3 we present the equations governing the two-phase flow in the capillary. Section 5.4 describes the solution for a single phase problem. In Section 5.5 we consider different possible configurations of the two-phase flow obtained by different choice of boundary conditions

and different pressure gradients in the fluids. The effect of appearance of the wetting films is also considered. We present the results by establishing correlation between the flow velocities of the fluids and wetting fluid saturation. Conclusions and key findings of the study are presented in Section 0.

5.2 Two-Phase Configurations in Triangular Pores

We consider a two-phase flow in a single triangular capillary. If the non-wetting fluid is introduced in such a capillary, filaments of the wetting phase (corner films) are formed along its corners. These filaments are separated from the non-wetting fluid by the arc-menisci [131]. In this study we assume that the rock is water wet; therefore, oil (non-wetting phase) occupies the center of the angular capillary, while water resides in the corners. It is also possible that oil is completely detached from the surface of the rock due to formation of the water films spreading over entire pore surface.

5.2.1 Characteristics of a Capillary

The geometry of an angular capillary is determined by its length l, two corner half-angles β_1, β_2, and the hydraulic radius r_h defined as ratio between the capillary cross section area $\mathcal{A}$ and its perimeter Π:

$$r_h = \frac{\mathcal{A}}{\Pi} \tag{5.1}$$

For a triangular capillary, the hydraulic radius is equal to the half of the radius of inscribed circle r_0. A schematic representation of a triangular pore cross-section is shown in Figure 5.1. For a pore of a more complex shape, defining the corner half-angles may be problematic, and its shape is generally characterized in terms of the dimensionless shape factor G [132]:

$$G = \frac{\mathcal{A}}{\Pi^2} = \frac{r_h^2}{\mathcal{A}} = \frac{r_0^2}{4\mathcal{A}} \tag{5.2}$$

For a triangular pore shape factor may be related to its actual shape according to

$$G = \frac{1}{4}\left(\sum_{i=1}^{3} \cot\beta_i\right)^{-1} \tag{5.3}$$

The typical values of the shape factor are the following. The shape factor for a circle $G_{circ} = 1/4\pi \approx 0.079$, for a square $G_{sq} = 0.0625$, while for triangles it can take values between $G_{max} = \sqrt{3}/36 \approx 0.048$ for equilateral triangles and $G_{min} = 0$ for a slit-like pores.

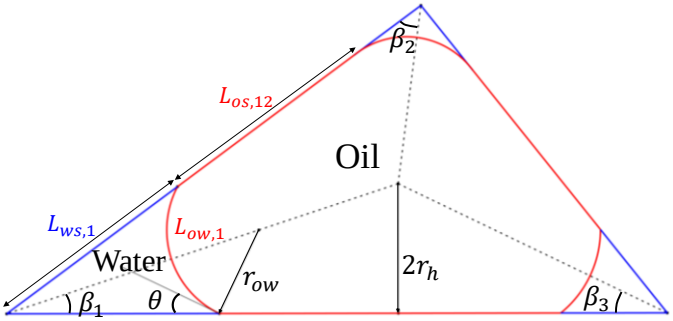

Figure 5.1: Cross section of a triangular capillary saturated with two immiscible fluids. Oil (non-wetting fluid) occupies the center of the capillary, water (wetting fluid) forms corner filaments.

Therefore, representation of pore bodies with triangular capillaries allows accounting for a range of different shapes that constitute the model of porous medium. Tetragon and more complex shapes are also considered in several pore network models [133].

5.2.2 Fluid Distribution

The radius of a meniscus between the fluids is given by the Laplace equation:

$$r_{ow} = \frac{\gamma_{ow}}{P_c} \tag{5.4}$$

where γ_{ow} is the surface tension.

If capillary equilibrium is established, the area of a corner filament formed by the wetting fluid is given by [134]:

$$\mathcal{A}_{w,i} = \begin{cases} r_{ow}^2 \left(\dfrac{\cos\theta \cos(\theta + \beta_i)}{\sin\beta_i} + \theta + \beta_i - \dfrac{\pi}{2} \right), & \text{if } \beta_i + \theta \leq \pi / 2 \\ 0 & \text{otherwise} \end{cases} \tag{5.5}$$

Here θ is the contact angle between water and oil on the surface of the rock. Equation (5.5) states that the area occupied by water is independent of the size of the capillary and is determined by the capillary pressure and the capillary shape. For that reason, the wetting fluid saturation ω_w

$$\omega_w = \frac{1}{\mathcal{A}} \sum_{i=1}^{3} \mathcal{A}_w(\theta, \beta_i) \tag{5.6}$$

is lower for large pores as it is inversely proportional to the full cross-section area $\mathcal{A}$. The total area of the interface between phases (water-oil, water-solid, oil-solid) is proportional to the length of the interphase boundary in the cross section and capillary length l. The lengths of the interphase boundaries are determined from elementary geometry [134]:

$$L_{ow} = \sum_{i=1}^{3} L_{ow,i} = 2r_{ow} \sum_{i=1}^{3} \left(\frac{\pi}{2} - \theta - \beta_i \right) \tag{5.7}$$

$$L_{ws} = 2\sum_{i=1}^{3} L_{ws,i} = 2r_{ow} \sum_{i=1}^{3} \frac{\cos(\theta + \beta_i)}{\sin \beta_i} \tag{5.8}$$

$$L_{os} = \frac{r_h^2}{G} - L_{ws} \tag{5.9}$$

Equations (5.5), (5.7), and (5.8) are combined to relate the area occupied by water and the length of the oil-water interface:

$$\mathcal{A}_{w,i} = \frac{L_{ow,i}^2}{\pi - 2(\theta + \beta_i)} \left(\frac{\cos\theta \cos(\theta + \beta_i)}{\sin\beta(\pi - 2(\theta + \beta_i))} - 1 \right) = L_{ow,i}^2 S_1(\theta, \beta_i) \tag{5.10}$$

The function $S_1(\theta, \beta)$ increases monotonically with increasing θ. Thus, equation (5.10) states that the area of the interface between oil and water is higher for low values of the contact angle.

Equations (5.4) to (5.6) indicate that saturation of water in the capillary is dependent on the capillary pressure. This saturation is very small at the initial stage of injection, where the capillary pressure is large. Further, when the capillary pressure decreases, the filaments swell. At some threshold capillary pressure, the configuration inside the capillary becomes unstable, resulting in the displacement of oil from the center of the capillary. It is possible, however, that water already invaded all the surrounding pores, which prevents penetration of oil into them. If the contact angle changes due to change of wettability towards increased water-wetness, a thin water film is formed over the entire surface of the capillary, disjoining oil from the rock surface (Figure 5.2b). Then the oil drops, surrounded by continuous water, acquire a possibility to move together with the water flow.

5.3 Flow Equations in a Capillary

The flow of the two liquids in a capillary is described as creeping isothermal flow of incompressible Newtonian fluids with constant viscosities. The flow equations to determine the velocity field in the cross section of a capillary are the continuity and the Stokes equations:

$$\mu_\alpha \Delta v_\alpha = \nabla P_\alpha, \quad \text{in } \Omega_\alpha, \quad \alpha = w, o \tag{5.11}$$

where μ_α is viscosity, v_α is the fluid velocity, ∇P is the pressure gradient. We assume that a constant pressure gradient exists within the fluids $\nabla P_\alpha = -\Delta P_\alpha / l$ with z axis directed along the length of capillary. $\Delta v = \partial_x^2 v + \partial_y^2 v$; x and y represent coordinates in the cross-section of the capillary. The domain occupied by the phase α is denoted with Ω_α, as shown in Figure 5.2.

The no-slip boundary conditions are imposed along the walls of the capillary:

BC0: $$v_\alpha = 0, \quad \text{on } \Gamma_{\alpha s}, \quad \alpha = w, o \tag{5.12}$$

We shall consider two different boundary conditions along the water-oil interface Γ_{ow}. The first boundary condition requires infinite surface shear viscosity and corresponds to the case of immobile non-wetting phase:

BC1: $$v_\alpha = 0, \quad \text{on } \Gamma_{ow} \tag{5.13}$$

The second boundary condition describes the simultaneous flow of two immiscible liquids separated by an interface, with no momentum transfer across it, as expressed by continuity in velocity and shear stress:

BC2: $$\begin{aligned} v_w &= v_o \\ \mu_w \nabla v_w \cdot \vec{n}_w &= \mu_o \nabla v_o \cdot \vec{n}_o \end{aligned}, \quad \text{on } \Gamma_{ow} \tag{5.14}$$

where $\vec{n}_\alpha$ is the unit outward normal vector along Γ_{ow}.

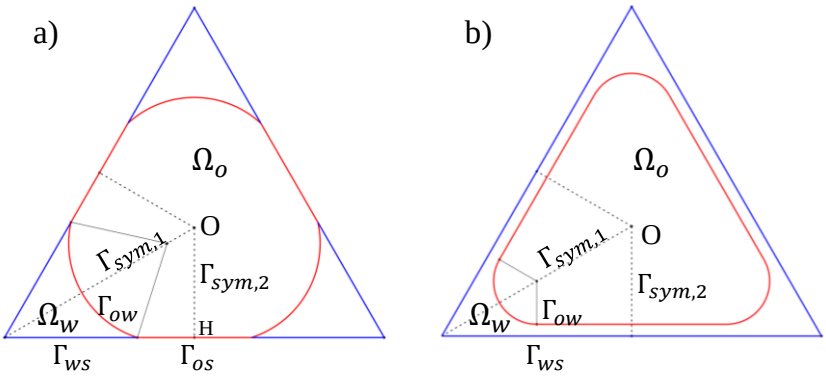

Figure 5.2: Cross section of a triangular capillary saturated with two immiscible fluids. a) Water-wet with no wetting film present b) Completely water-wet with thin wetting film.

Solving the flow equations (5.11), together with the formulated boundary conditions makes it possible to calculate average fluid velocities:

$$\langle v_\alpha \rangle = \frac{1}{\mathcal{A}_\alpha} \int_{\Omega_\alpha} v_\alpha d\mathcal{A} \quad \alpha = w, o \tag{5.15}$$

Hydraulic conductances $g_{\alpha\beta}$ are introduced as the proportionality coefficients between the volumetric flow rate q_α of the phase and the pressure gradient $\Xi_\alpha = \partial_z P_\alpha$, according to

$$q_\alpha = \int_{\Omega_\alpha} v_\alpha d\mathcal{A} = \mathcal{A}\omega_\alpha \langle v_\alpha \rangle = \sum_{\beta=w,o} g_{\alpha\beta} \cdot \Xi_\beta, \quad \alpha = w, o \tag{5.16}$$

The form of (5.16) implies that the cross terms are also taken into account for the transport within the capillary [135, 136].

We consider a dimensionless form of the problem by scaling the spatial coordinates:

$$\tilde{x} = \frac{x}{r_0}, \quad \tilde{y} = \frac{y}{r_0}, \quad \tilde{v}_\alpha = \frac{v_\alpha \mu_w}{r_0^2 \Xi_w} \tag{5.17}$$

Substitution into (5.11) results in the following system of equations:

$$\tilde{\mu}_\alpha \Delta \tilde{v}_\alpha + \tilde{\Xi}_\alpha = 0, \quad \alpha = w, o \tag{5.18}$$

$$\tilde{\mu}_w = 1, \quad \tilde{\mu}_o = \frac{\mu_o}{\mu_w}, \quad \tilde{\Xi}_w = 1, \quad \tilde{\Xi}_o = \frac{\Xi_o}{\Xi_w} \tag{5.19}$$

The solution of this dimensionless problem depends only on viscosity ratio $\tilde{\mu}_o$, the ratio of the pressure gradients $\tilde{\Xi}_o$, the geometry of the water menisci determined by θ and P_c, and the choice of the boundary conditions (BC0 and BC1, or BC0 and BC2). Using the dimensionless variables, it possible to rewrite equation (5.16) in the form:

$$q_\alpha = \frac{r_0^4 \Xi_w}{4G\mu_w} \cdot \omega_\alpha \langle \tilde{v}_\alpha \rangle = \frac{r_0^4 \Xi_w}{4G\mu_w} \sum_{\beta=w,o} \tilde{g}_{\alpha\beta} \tilde{\Xi}_\beta, \quad \alpha = w, o \tag{5.20}$$

where $\tilde{q}_\alpha = \omega_\alpha \langle \tilde{v}_\alpha \rangle$ is the dimensionless volumetric flux.

As mentioned above, the solution of the flow equations depends on the shape of the capillary. We limit our study to capillaries which cross-sections are equilateral triangles. Symmetry of an equilateral triangle allows narrowing the domain by imposing boundary conditions across the lines of symmetry (Figure 5.2):

BCs: $$\nabla v_\alpha \cdot \vec{n}_\alpha = 0, \quad \text{on } \Gamma_{sym,1}, \Gamma_{sym,2} \tag{5.21}$$

The driving force (pressure gradient) of the flow can differ for the two phases. If the oil is connected to the oil phase at the capillary faces, then we assume that the pressure drops are equal in the phases. In this case oil in the pore body is a part of an oil cluster and we refer to it as "active oil". Another possibility is that oil is disconnected from the oil cluster if neighboring pores do not contain oil. For such a system oil is present in the pore bodies in a form of disjoint drops, which we will refer to as "oil ganglia". The action of capillary forces at the ends of the capillary can compensate the pressure drop in the oil drop, making ganglia immobile. However, in the case of a strongly wet surface, formation of wetting films on the surface of the pore may result in mobilization of oil the drops, so that their flow is driven by the viscous forces on the oil-water interface.

In order to calculate hydraulic conductances according to equation (5.20), we implemented a numerical code for the flows in an equilateral triangle into the FlexPDE software [137]. Only strongly water-wet conditions were investigated ($\theta < 60°$). According to equation (5.5), water is always present in the corner filaments. We study several important cases, as described below.

5.4 Single-Phase Flow

For the single-phase problem, the domain Ω_w fills up the whole capillary. This case is described by a single equation (5.18) for water with the no-slip boundary condition BC0 (5.12) (We do not mention the symmetry boundary conditions (5.21) hereinafter in the text as they are just a useful tool to simplify the solution procedure):

$$\begin{aligned} \Delta \tilde{v}_w &= -1, \\ \tilde{v}_w &= 0, \quad \text{on } \Gamma_{ws} \end{aligned} \tag{5.22}$$

The resulting average dimensionless velocity is

$$\langle \tilde{v}_w \rangle \equiv \tilde{v}_0 = \frac{3}{20} \tag{5.23}$$

The volumetric flux calculated according to equation (5.20) is given by

$$q_w = \frac{3G}{5} \frac{\mathcal{A}^2 \Xi_w}{\mu_w} \tag{5.24}$$

Equation (5.23) is generalized for the flow of a fluid with arbitrary viscosity as follows:

$$\langle \tilde{v}_\alpha \rangle = \frac{\tilde{v}_0}{\tilde{\mu}_\alpha} \tag{5.25}$$

This result is in agreement with the single-phase conductance calculated by Patzek and Silin [132]. Their study supports the conclusion that dependence (5.24) provides a good approximation for the capillary conductance of triangular capillaries with arbitrary shape factors G.

5.5 Two Phase Flow

In this Section, we present the results for several flow configurations in pore bodies occupied by the two phases. Flow equations (5.18) and no-slip boundary condition on the surface of the rock BC0 (5.12) are valid for each configuration. The cases differ from each other by the choice of boundary condition at the oil-water interface: either BC1 (5.13) or BC2 (5.14); and by the different pressure gradient across the oil phase: either $\tilde{\Xi}_o = 0$ or $\tilde{\Xi}_o = 1$. This results in four different problems. We do not consider a combination of BC1 and $\tilde{\Xi}_o = 1$ since this implies that both phases are mobile and can flow, while the boundary between them remain immobile, which is an obvious contradiction. The rest three cases are discussed below. As above, we will refer to an oil phase as "active oil" in the cases where the pressure drops in both fluids are equal, and as "ganglia", in the cases where the pressure drop in oil is zero.

5.5.1 Flow in the Corner Filaments. Immobile Ganglia

Consider the case of immobile oil phase with the corner flow of the wetting fluid (Figure 5.2a), this may occur due to action of the capillary forces acting at the inlet and outlet of the capillary. No flow occurs in Ω_o and $\tilde{v}_o = 0$. Thus, properties of the oil do not have any influence on the flow in the corner filaments, and the average water velocity $\langle \tilde{v}_w \rangle$ may only depend on θ and P_c. The formulated problem is described by the following system of equations:

$$\begin{aligned} \Delta \tilde{v}_w &= -1, \quad \text{in } \Omega_w \\ \tilde{v}_w &= 0, \quad \text{on } \Gamma_{ws},\ \Gamma_{ow} \end{aligned} \tag{5.26}$$

Varying the contact angle θ in the range between 0° and 60°, and ω_w from 0.05 to $\omega_w^{\max}$ (determined by the highest radius of interface when water menisci do not intersect), we obtain a correlation for average dimensionless velocity for the flow in corner filaments, shown in Figure 5.3. The maxiumum wetting fluid saturation $\omega_w^{\max}$ depends on the contact angle θ and may be understood by the following consideration. If we fix the endpoints of the meniscus

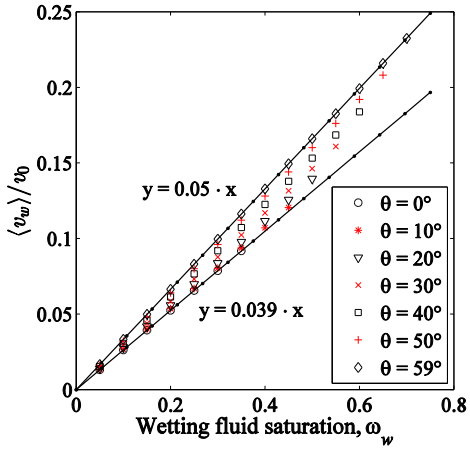

Figure 5.3: Average flow velocity of water in the corner in the case of no-slip boundary condition at the interface between two fluids for different values of contact angle θ.

Table 5.1: Proportionality coefficients for an average velocity of wetting films and ganglia for the case of mobile ganglia

θ	0°	10°	20°	30°	40°	50°	59°	average
$C_1(\theta)$	0.039	0.040	0.042	0.044	0.046	0.048	0.050	0.046

in the corner and start increasing contact angle θ the area occupied by the water $\mathcal{A}_w$ will also increase. The limiting position of menisci, where they meet, is the middle point of the side of the triangle, the same for all contact angles θ. Hence, the capillary saturation $\omega_w^{\max}(\theta)$ is higher for larger values of the contact angle.

It can be seen from Figure 5.3 that a linear dependence can be established between the average flow velocity $\langle \tilde{v}_w \rangle$ and wetting fluid saturation ω_w for each given value of the contact angle θ:

$$\langle \tilde{v}_w \rangle = C_1(\theta) \cdot \omega_w \tag{5.27}$$

The average flow velocity is slightly lower if the system is more water-wet. This is explained by a larger length of the oil-water interface according to equation (5.10). A larger immobile boundary results in enlarged flow resistance, as illustrated in Figure 5.4.

We apply the average value of C_1 to relate the flow velocity to the water saturation, which does not introduce a significant error:

$$\langle \tilde{v}_w \rangle = \bar{C}_1 \cdot \omega_w \tag{5.28}$$

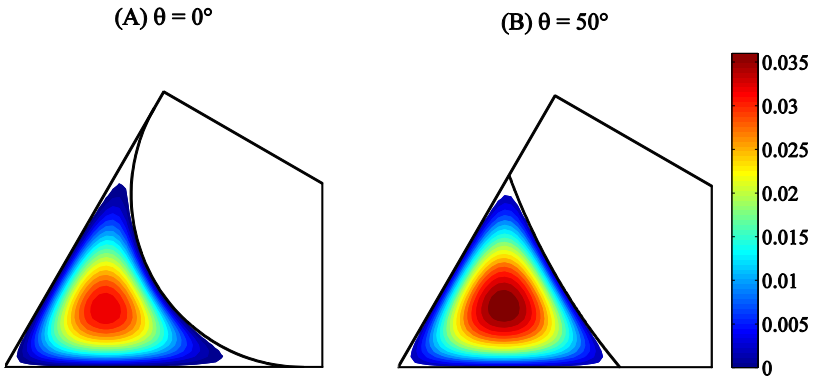

Figure 5.4: Dimensionless velocity profiles for corner flow in contact with immobile oil phase for contact angle of (A) 0° and (B) 50°. Saturation of the wetting phase is equal to 0.35 in both cases.

The average value $\bar{C}_1 = 0.046$ was calculated based on all the simulation data presented in Figure 5.3. The error introduced by averaging in equation (5.28) is admissible, for the three main reasons:

1. We consider only one possible shape of the triangle.
2. The triangular shape is only an approximation to the real pore shapes.
3. Surface roughness is expected to have an effect on the shape of the corner filaments.

Similar considerations apply to the rest of the presented results.

5.5.2 Flow of Water and Active Oil

The following calculation represents the case when both water and oil can flow subjected to equal pressure gradients. The flow of water in the corner filaments is expected to have an influence on the flow of oil and vice versa. For very viscous oil $\tilde{\mu}_o \gg 1$, the result should be similar to the calculated corner flow of water in contact with immobile oil. The governing system of equations is given by:

$$\begin{aligned} \Delta \tilde{v}_w &= -1, && \text{in } \Omega_w, \\ \tilde{\mu}_o \Delta \tilde{v}_o &= -1, && \text{in } \Omega_o, \\ \tilde{v}_\alpha &= 0, && \text{on } \Gamma_{\alpha s}, \\ \tilde{v}_w &= \tilde{v}_o, && \text{on } \Gamma_{ow}, \\ \nabla \tilde{v}_w \cdot \vec{n}_w &= \tilde{\mu}_o \nabla \tilde{v}_o \cdot \vec{n}_o, && \text{on } \Gamma_{ow} \end{aligned} \tag{5.29}$$

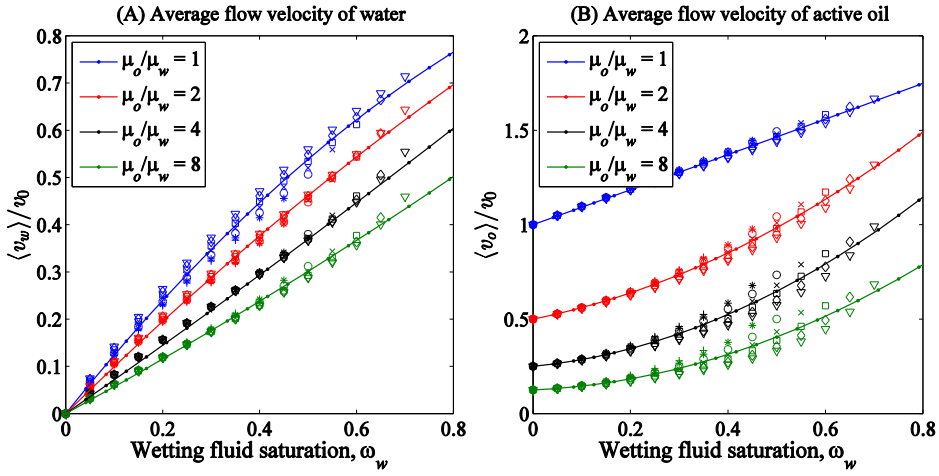

Figure 5.5: Average flow velocity of (A) water and (B) active oil for different viscosity ratios. Solid lines represent proposed approximations, markers represent simulation data: (plus) $\theta = 0°$, (star) $\theta = 10°$, (circle) $\theta = 20°$, (cross) $\theta = 30°$, (square) $\theta = 40°$, (diamond) $\theta = 50°$, (triangle) $\theta = 59°$.

The contact angle in the computations varied between 0° and 60°. Figure 5.5 shows the average velocities of fluids; different markers are used for the different contact angles. It can be seen that variation of the contact angle has stronger effect on the velocity of oil in the case of high viscosity ratios (Figure 5.5B).

The velocity of the oil phase increases faster with saturation at low values of contact angle. This is again an effect of the length of the oil-water interface area, which is higher for low contact angles. As saturation increases, oil is substituted by water in the corners, which can flow much easier due to lower viscosity. The flow of water facilitates the flow of oil by increasing the flow velocity at the oil-water interface.

Data shown in Figure 5.5 can be approximated with polynomials:

$$\langle \tilde{v}_\alpha \rangle = P_n^\alpha(\tilde{\mu}_o, \omega_w) = \sum_{k=0}^{n} a_k^\alpha(\tilde{\mu}_o)\omega_w^k \tag{5.30}$$

The second-order polynomial approximation provides a sufficient accuracy:

$$\begin{aligned} \langle \tilde{v}_w \rangle &= a_1^w \omega_w + a_2^w \omega_w^2 \\ \langle \tilde{v}_o \rangle &= \frac{\tilde{v}_0}{\tilde{\mu}_o} + a_1^o \omega_w + a_2^o \omega_w^2 \end{aligned} \tag{5.31}$$

The second equation in (5.31) accounts for the fact that in the case of fully oil saturated pore the flow velocity is determined by the solution for the single phase problem (5.25). Correlations (5.31) are plotted in Figure 5.5. The polynomial coefficients based on the

Table 5.2: Coefficients a_k^α for the polynomial approximation of the average velocity of the corner flow of water and active oil

	$\tilde{\mu}_o = 1$	$\tilde{\mu}_o = 2$	$\tilde{\mu}_o = 4$	$\tilde{\mu}_o = 8$
a_1^w	0.193	0.152	0.107	0.084
a_2^w	−0.060	−0.026	0.0084	0.0125
a_1^o	0.138	0.077	0.038	0.017
a_2^o	0.0032	0.136	0.163	0.134

Table 5.3: Coefficients for the rational function approximation of a_k^α as function of viscosity

	Q_0	Q_1	Q_2	Q_3	R_0	R_1	R_2	R_3
a_1^w	0.312	0.041	–	–	1.0	0.835	–	–
a_2^w	−0.086	0.026	–	–	1.0	–	–	0.0175
a_1^o	0.557	−0.019	–	–	1.0	2.89	–	–
a_2^o	–	–	–	0.0016	1.0	0.811	0.179	–

simulation data for four different viscosity ratios $\tilde{\mu}_o = 1, 2, 4, 8$ are given in Table 5.2. It can be seen from the table that deviation from linear behavior for the velocity of water is relatively low ($a_2^w \ll a_1^w$) and is observed only at high saturations. The dependence of the oil flow velocity is more complicated. For the considered viscosity ratios $\tilde{\mu}_o = 2, 4, 8$, the effects of increasing wetting fluid saturation are similar (as a_2^o has similar values) and comes mostly from the second term in the approximation (5.31).

The dependences of the polynomial coefficients a_k^α on the viscosity ratio were established by applying approximation based on rational functions:

$$a = \frac{\sum_{k=0}^{n} Q_k \tilde{\mu}_o^k}{\sum_{k=0}^{m} R_k \tilde{\mu}_o^k} \tag{5.32}$$

The results of this fitting are presented in Table 5.3. They allow calculating the polynomial coefficients for the phase flow velocity in the range of viscosity ratios from 1 to 8.

The average velocity of the oil phase may exceed its average velocity in the single-phase case. The reason is that the corner water occupies the regions where velocity is low due to proximity to the surface of the capillary. Thus, calculation of the average velocity of oil includes integration over smaller domains with higher velocities resulting in increased average velocity.

To illustrate the effect of the wetting films on the flow of oil we present the calculated dimensionless flux of oil. Figure 5.6 illustrates the effect. It can be seen that the volumetric flux of oil decreases only at low viscosity ratios. At high viscosity ratios, it remains the same or can even increase, as explained above. In Figure 5.7 this effect is illustrated by the plot of the velocity field in the capillary cross-section.

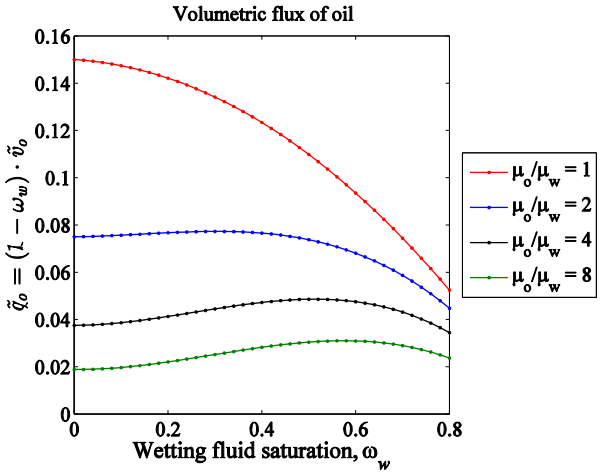

Figure 5.6: Change of dimensionless volumetric flux of active oil with varying wetting fluid saturation for different viscosity ratios.

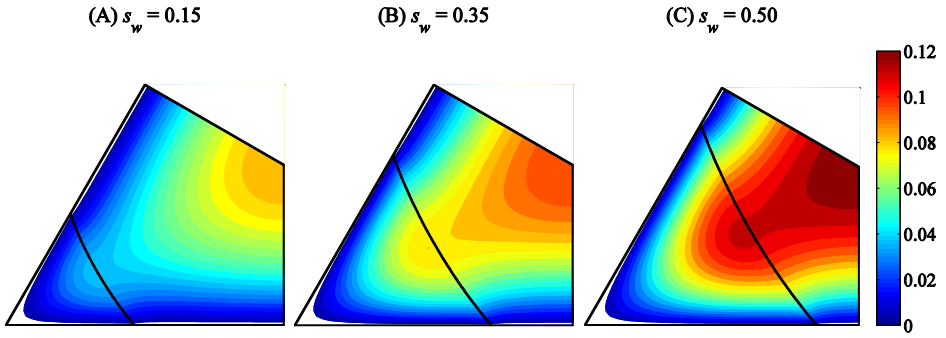

Figure 5.7: Flow velocity profile for water and active oil with increasing water saturation. Oil is accelerated by the moving oil-water interface (black arc). Contact angle $\theta = 50°$, viscosity ratio $\tilde{\mu}_o = 4$.

5.5.3 Flow of Water and Mobile Oil Ganglia

The following calculation represents the case of an oil ganglion, with no pressure drop across the oil phase. The ganglion may flow carried by the flow of water in the corner filaments due to continuity of velocity and shear stress at the oil-water interface. The formulated problem is described by the following system of equations:

$$\begin{aligned} \Delta\tilde{v}_w &= -1, && \text{in } \Omega_w, \\ \tilde{\mu}_o \Delta\tilde{v}_o &= 0, && \text{in } \Omega_o, \\ \tilde{v}_\alpha &= 0, && \text{on } \Gamma_{\alpha s}, \\ \tilde{v}_w &= \tilde{v}_o, && \text{on } \Gamma_{ow}, \\ \nabla\tilde{v}_w \cdot \vec{n}_w &= \tilde{\mu}_o \nabla\tilde{v}_o \cdot \vec{n}_o, && \text{on } \Gamma_{ow}, \end{aligned} \tag{5.33}$$

As discussed above, the flow may occur when the system is strongly water wet and there are water films, which cover the whole surface of the pore body as illustrated in Figure 5.2b. Therefore, we consider a single contact angle $\theta = 0°$ and infinitesimally thin wetting film on the rock surface. The computed average velocities of phases are shown in Figure 5.8.

For this case we make use of the following approximations, which are also illustrated in Figure 5.8:

$$\begin{aligned} \langle\tilde{v}_w\rangle &= c_1^w \omega_w \\ \langle\tilde{v}_o\rangle &= c_2^o \omega_w^2 \end{aligned} \tag{5.34}$$

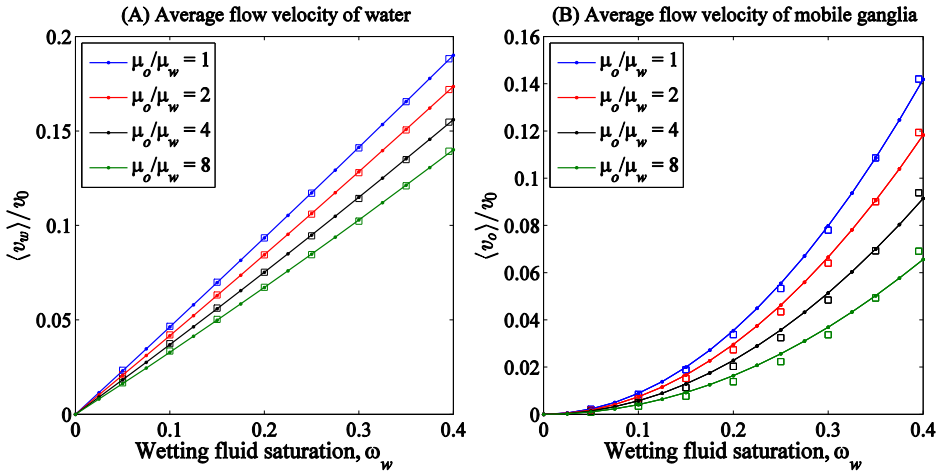

Figure 5.8: Average flow velocity of (A) water and (B) mobile ganglia oil for $\theta = 0°$ and different viscosity ratios. Markers represent simulation data, solid lines represent proposed approximations

The values of the coefficients c_k^α for different viscosity ratios, and approximation of these coefficients by rational functions (5.32) as functions of viscosity are given in Tables 5.4, 5.5 respectively. As the viscosity ratio $\tilde{\mu}_o$ tends to infinity, c_2^w approaches $C_1(0)$, calculated for immobile ganglia and c_2^o tends to zero, which is in accordance with the physical nature of the system.

According to equation (5.34), it is possible to establish a relation between the dimensionless volumetric flux of oil and water according to

$$\begin{aligned} \tilde{q}_w &= c_1^w \omega_w^2 \\ \tilde{q}_o &= (c_2^o \,/\, c_1^w)(1-\omega_w)\tilde{q}_w \end{aligned} \tag{5.35}$$

An important result is that the flux of oil is proportional to the volumetric flux of water and the area of capillary occupied with oil.

Table 5.4: Coefficients c_k^α for the polynomial approximation of the average velocity of the corner flow of water and mobile oil ganglia for $\theta = 0°$.

	$\tilde{\mu}_o = 1$	$\tilde{\mu}_o = 2$	$\tilde{\mu}_o = 4$	$\tilde{\mu}_o = 8$
c_1^w	0.071	0.064	0.058	0.052
c_2^o	0.133	0.111	0.086	0.062

Table 5.5: Coefficients for the rational function approximation $(Q_0 + Q_1\tilde{\mu}_o)/(R_0 + R_1\tilde{\mu}_o)$ of the coefficients c_k^α as functions of viscosity.

	Q_0	Q_1	R_0	R_1
c_1^w	0.082	0.016	1.0	0.390
c_2^o	0.157	–	1.0	0.198

5.5.3.1 Effect of the wetting films on the flow of mobile oil ganglia

We further study the effect of the presence of the wetting films on the surface of the rock, as illustrated in Figure 5.2b. The thickness of the wetting films in our simulations varied in the range $h = 0$ to 0.2 (a fraction of the radius of the inscribed circle r_0). It should be pointed out that presence of a wetting film does not allow the saturation to fall below a certain limit that can be calculated according to:

$$\omega_w^{\min} = 1 - (1+h)^{-2} \tag{5.36}$$

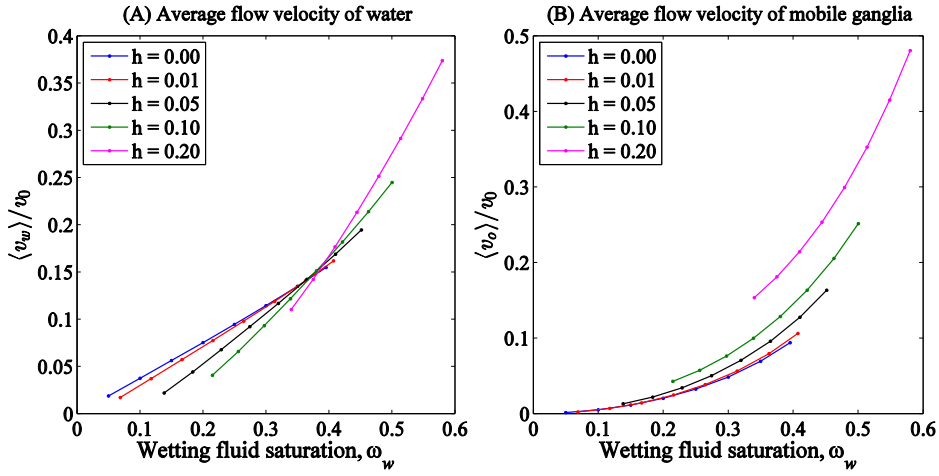

Figure 5.9: Effect of the wetting films on the average flow velocity of (A) water and (B) mobile ganglia for the case of velocity and shear stress continuity at the interface between fluids and zero pressure drop across oil phase. Viscosity ratio $\tilde{\mu}_o = 4$.

Equation (5.36) is obtained by considering a triangular capillary where oil occupies the whole capillary except for the area at a distance to the surface less than h. The calculated values of $\omega_w^{\min}(h)$ are the following: $\omega_w^{\min}(0.05) = 0.093$, $\omega_w^{\min}(0.1) = 0.174$, $\omega_w^{\min}(0.2) = 0.31$. For this reason, not all of the presented curves go to low values of saturations.

The effect of the wetting films on the average flow velocities of water and oil is illustrated in Figure 5.9. We present the results only for a single viscosity ratio of $\tilde{\mu}_o = 4$, as they are rather similar for other cases.

The effect can be described as follows. Compare two pore bodies with equal areas occupied by water, one with wetting films present, while in the other the water is present only in the corner filaments. Then the flow velocity of water is higher in the absence of the wetting films as shown in Figure 5.9A. This may be explained by a lower water-rock interface in the first case and, hence, a smaller effect of viscous forces. Also it can be seen form Figure 5.9B that emergence of wetting films results in increase of the flow velocity of oil.

This effect is due to a larger moving boundary between water and oil, even though the flow velocity of the water in the wetting films is very low (compared to the flow of water in the corners). This can be better understood by comparing dimensionless velocity fields for different wetting films of the thicknesses $h = 0.05$ and $h = 0.2$ shown in Figure 5.10.

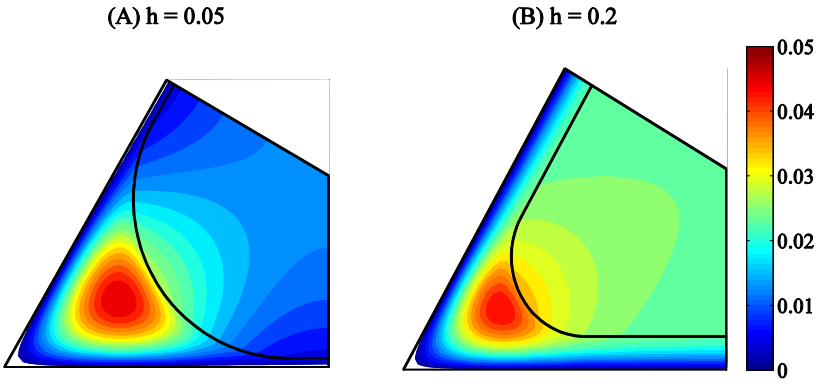

Figure 5.10: Flow velocity profile for water and oil ganglia with the wetting film thickness h equal to (A) 0.05 and (B) 0.2. Oil flow is driven by the moving oil-water interface (black arc). Viscosity ratio $\tilde{\mu}_o = 4.$ °. Saturation of the wetting phase is equal to 0.36 in both cases.

5.6 Conclusions

On the basis of performed study it may be concluded that the interactions of the two fluids in an angular pore body are significant. We have demonstrated that the interface between the two fluids is important and affects the distribution of local velocities in the cross-section. In the simplified geometry described by equilateral triangular capillaries, simple relations can be established between the velocities of the flow and saturations. One may expect these dependences to vary if other shapes are considered. The key findings of this study may be outlined as follows:

1) Flow of water may occur in the corner filaments of oil filled pore bodies even if oil is immobile. The flow velocity linearly increases with water saturation (Figure 5.3). This velocity is lower than the velocity associated with a single phase flow. This may result, for example, in the fact that if chemical solution is injected in the porous medium, the penetration of chemicals to the pores that remain filled with oil will occur with some delay.
2) Accounting for the effect of corner flow on the transport of active oil demonstrates that for higher velocities of oil its volumetric flux does not increase when saturation increases (Figure 5.6, 5.7).
3) Second-order polynomials with viscosity-dependent describe a relationship between flow velocities of the phases and water saturation (Equation (5.31), Table 5.2, 5.3) when both phases are subjected to equal pressure drop.
4) The water films may carry the oil ganglia. In the case of perfect wetting (zero contact angle), linear dependency for water and quadratic for oil can be used to relate the flow velocities of the phases to the water saturation (Equation (5.34), Table 5.4, 5.5)

5) Formation of the wetting films on the surface of the pore bodies results in an increased flow velocity of oil. The velocity increases more for a larger thickness of the wetting film. (Figure 5.9B, Figure 5.10)
6) The volumetric flux of mobile oil ganglia is proportional to the volumetric flux of water in the corner filaments and oil ganglia saturation (Equation (5.35)).

6

Tertiary Recovery Model with Mobilization of Oil Ganglia

6.1 Introduction

Injection of water to displace oil from porous media always results in trapping considerable amounts of oil in the swept zones. Oil may flow when it forms a continuous phase connected to the production side ("outlet"). When the oil saturation decreases, more oil drops separate from the continuous oil cluster. The oil drops (ganglia) are trapped inside the swept zone, and it is usually assumed that they cannot flow.

In this study, we consider oil displacement by a fluid that contains an agent changing the wettability, referred to as the active species. Changing of the wettability of the rock results in mobilization of a part of the residual oil, which is included in the flow. Mobilization may occur due to the different mechanisms depending on an injected fluid and a type of the rock. We do not specify or study any specific mechanism. The common idea is that mobilized oil simply joins the continuous oil phase [92]. One of the core ideas of this chapter is that we assume a separate transport mechanism for the flow of the mobilized oil in a form of disconnected oil ganglia. This is a new point of the present work: while the macroscopic description of flow of the two continuous phases is well established, there is a lack of a model to describe the flow of a discontinuous phase within porous media [138, 139]. Meanwhile, as follows from the results of the previous Chapter, such a flow may occur on micro-level.

We develop a mathematical model to describe macroscopic two-phase flow in porous media accounting for mobile oil ganglia. The system of the flow equations is formulated and solved numerically. It involves the flows of continuous ("active") water and oil phases, as well as of the water films and oil ganglia. The constituting relations for the model (relative permeabilities and saturations of the different phases) are evaluated by analysis of the flows in a single capillary and in a capillary network consisting of equal capillaries. This representation of the porous medium is probably oversimplified, but it gives qualitatively correct and relatively simple analytical dependencies for the functions required in the model. The model incorporates analysis of the possible patterns of microscopic two-phase flow in a separate capillary, presented in Chapter 5, with successive upscaling to obtain macroscopic flow parameters.

The structure of this Chapter is as follows. In the next Section we discuss the mechanisms that may improve the recovery due to modification of the chemistry of the injected water and, in particular, explain the mechanism of ganglia mobilization that will be studied in this work. Section 6.4 contains a formulation of the macroscopic flow model and discussion of its limitations. In Section 6.5 we describe the way to obtain macroscopic model parameters based on the pore-scale investigation performed in Chapter 5. We verify the model predictions by numerical simulation of a tertiary recovery process in Section 6.6.

6.2 Trapping of Oil

Modification of the injected water for enhanced oil recovery may affect the oil production in two ways. During the secondary water injection starting from low water saturation, an active substance added to water may affect trapping of the oil ganglia and formation of the discontinuous oil phase separated from the production site. Since such a discontinuous phase is difficult to mobilize and produce, the goal at this stage is to decrease the amount of trapped oil.

Laboratory studies performed on the rock samples after waterflooding experiments support the fact that prevailing amount of trapped oil is present in a form of oil drops with typical sizes from one to several pore diameters [68]. Different factors, such as pore geometry, wettability and injection rate, determine the magnitude of the residual oil and its microscopic distribution within porous media [140]. Reduction of the residual oil saturation is one of the most important tasks in the petroleum industry. Different enhanced oil recovery (EOR) techniques are designed in order to achieve this goal. Among them, the chemical methods mostly include surfactant-polymer-micellar flooding [140]. Recent studies also address microbial injection [141, 142] and the smart water flooding [15, 27, 143], which was discussed in details in Chapter 1.

Numerous experimental and theoretical studies addressed the mechanism controlling trapping in porous media [68, 144-146]. The instability of two-phase configurations in a thin throat connecting two oil-filled pores results in a collapse of water films, so that the throat becomes filled with water. This process is usually referred to as snap-off [67]. As a result, the connectivity in the oil phase decreases and if snap-off occurs in all the throats surrounding the oil-filled pore it is completely detached from the oil cluster.

A significant progress in this area of research has been achieved by means of pore-network simulations. These studies demonstrate that snap-off is a very frequent event among other possible displacement processes [130] and is strongly dependent on the pore to throat size ratio and rock wettability. Considering a single pore in a pore-network realization depending on the externally controlled capillary pressure, it is possible to predict the mechanism by which this specific pore is filled. This is achieved by means of the method by Mayer, Stowe, and Princen (MS-P) [147]. Simulated drainage or imbibition processes were used to predict

quantitatively such important parameters as residual saturations, relative permeabilities, and phase distribution within the pore-network [128, 148].

The intensity of snap-off is related to the rock wettability. Studies suggest that strongly water-wet conditions are not favorable for the waterflooding process [149-151]. This is in good agreement with the findings from the pore-network models [148]. However, the contact angle measurements on calcite surface demonstrated that for the smart water fluids contact angle reduces [19, 152]. A possible explanation for this inconsistency in between theoretical predictions and experiment is that trapping is not affected by the composition of the injected brine at early stages, since a bank of connate water is formed ahead of the injection brine [95]. Moreover, if the change of contact angle is not instantaneous and requires a considerable amount of time, then the effect of wettability alteration will not be seen immediately. Thus, a transition to a very strong water wet conditions does not result in increased trapping when performing smart water flooding as a secondary recovery process.

EOR is usually performed not as a secondary, but as a tertiary recovery process. This means that the residual oil saturation is already formed, and the target for recovery is mostly the disconnected oil phase. For the tertiary recovery, the mechanism of entrapment of the oil ganglia is not relevant anymore. The most important problem is what physical mechanisms may mobilize the discontinuous oil phase and make it moving towards the production site.

6.3 Mechanisms of Residual Oil Mobilization

On the later stage, when the brine saturation is sufficiently large, most of the oil is already in the form of the oil ganglia. Struggling with trapping cannot produce much at this stage. Instead, the goal is to mobilize the discontinuous oil phase.

A reason why the discontinuous oil clusters cannot flow is the action of the capillary forces (the so-called “Jamin effect” [140]. Consider a drop of oil in a capillary surrounded by the flowing water (Figure 6.1a). A moving force for this drop is the pressure difference in the water flowing around it. However, instead of being displaced, the oil drop adjusts the curvatures of menisci in such a way that the difference of capillary pressures compensates the pressure difference around the drop. The pressure inside the drop remains constant, so that it does not move. Simple order-of-magnitude estimates show that this capillary effect is impossible to overcome unless the drop becomes of a macroscopic size or the “global” pressure difference becomes extremely large.

These considerations are true provided that the drops of oil are attached to the walls of the capillary. In fact, by analysis of the force balance at the liquid-liquid-solid contact it may be demonstrated that it is the adhesion forces between liquids and solid (or, the oil-solid and water-solid surface tensions) that keep the drop attached to the surface.

Consider now the case where water is an absolutely wetting phase, that is, it spreads over the surface. In such cases, a water film is formed, and it separates the oil from the walls of the

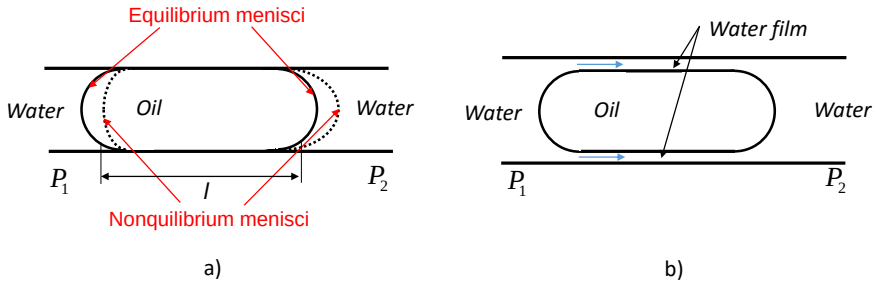

Figure 6.1: An oil drop surrounded by water in a capillary. a) Situation of the not completely water wet rock: origin of the Jamin effect; b) Absolutely water wet rock. Slide of an oil drop over the water film.

pores. If this film flows, the oil drops may slide on its surface (Figure 6.1b). The Jamin effect does not act anymore.

Assume that during the tertiary recovery stage, an agent changing the reservoir wettability towards absolutely water wet is injected. Ideally, this may result in formation of moving water films, disconnection of the oil phase from the surface and additional production of the discontinuous residual oil. As an example, injection of the brine of a different salinity has been considered as a possible way to change wettability of the rock [7, 27, 153]. Adsorption of ions on the calcite or silica surface may also result in changing wettability. Another possibility is an injection of surfactants [154, 155] or enzymes [156, 157].

An assumption that mobilized oil joins the continuous phase cannot explain multiple experimental observations, according to which additional oil in e.g. smart flooding experiments is produced after injection of many porous volumes injected [27, 158-160]. Experimental observations also show that this additional oil may come in the form of separate drops [161], although this might be explained by the small porous volumes and the interaction of the oil and the outlet tubing. The velocity of a separate oil drop sliding over the moving water film will be equal to the surface velocity of this film. Evidently, such velocity is much lower than the velocities of the continuous oil and water phases. Additionally, formation of the films may take a while, so that the discontinuous oil flow appears with a delay. As a result, the additional oil will be produced slowly, after many porous volumes have been injected.

Absolute wettability is not required for mobilization of, at least, some oil drops. This is only a condition for rather large pores. For smaller pores, change of wettability may result in a formation of water films before zero contact angle is achieved. This may explain the relation between the variation of the contact angle and the expected additional recovery [162].

In this study, we concentrate on the mechanism of the drop mobilization under the tertiary oil recovery. The model developed below is only applicable to describe this mechanism. For description of the trapping mechanism additional investigation is required, for example, an extension of the formalism proposed by P. Bedrikovetsky [139].

6.4 Macroscopic Model Formulation

In order to simulate the effect of presence and mobilization of oil ganglia on waterflooding of petroleum reservoirs, we apply the traditional approach based on mechanics of continuous medium. A similar approach was used for the water-alternate-gas injection [163]. Consider a one-dimensional problem of oil displacement by water containing a chemical. The water (subscript *w*) flows as a continuous "active" phase (subscript a) or as a film (subscript f). Oil (subscript *o*) may also flow as a continuous phase (a) or as ganglia (g). The scheme of partitioning for the pore space is shown in Figure 6.2. The chemical substance flows with the injected water and can penetrate the water films in the corners of the oil filled pores and change the wetting state. When wettability changes significantly, the water films are formed and the oil ganglia are mobilized. This provides an additional transport mechanism for the oil phase, contributing to the relative permeability curves.

The mass conservation laws describing the transport of phases that were introduced in Chapter 2 should be modified in order to account for different transport mechanisms inherent to each phase:

Water: $$\phi\partial_t s + \partial_x(u_{wa} + u_{wf}) = 0 \tag{6.1}$$

Oil: $$\phi\partial_t(s_{oa} + s_{og}) + \partial_x(u_{oa} + u_{og}) = 0 \tag{6.2}$$

Species: $$\phi\partial_t(s_{wa}c_a + s_{wf}c_f) + \partial_x(u_{wa}c_a + u_{wf}c_f) = 0 \tag{6.3}$$

where ϕ is porosity, $s = s_{wa} + s_{wf} + s_{wi}$ is the overall water saturation, u are the velocities of the different phases (depending on the subscript), c_a is the molar concentration of the active species in the water, c_f is its molar concentration in the water films. The values of c_a and c_f may be different. If, for example, the chemical is adsorbed on the surface of the rock, its concentration close to the surface should be higher than in the bulk. As discussed earlier, a considerable amount of time may be required for a chemical in order to accumulate in the water films and to start acting as a wettability modifier; thus, we introduce the kinetic description of the evolution of c_f:

$$\partial_t c_f = \kappa(\bar{c}_f(c_a) - c_f) \tag{6.4}$$

where κ is the deposition rate in s^{-1}, and $\bar{c}_f(c_a)$ is the concentration in the water films in equilibrium with the given bulk concentration c_a, which we will regard as a sorption isotherm. The velocities are determined via the generalized Darcy laws, for the water phase:

$$u_{wa} = -\frac{kk_{rwa}}{\mu_w}\partial_x P_w, \quad u_{wf} = -\frac{kk_{rwf}}{\mu_w}\partial_x P_w\,, \tag{6.5}$$

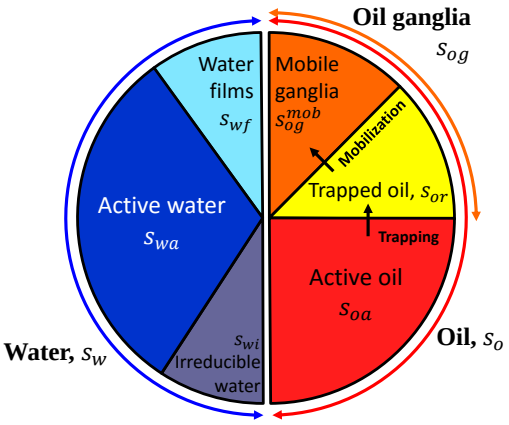

Figure 6.2: Structure of the filling of the pore space.

$$u_w = u_{wa} + u_{wf} = -\frac{k}{\mu_w}(k_{rwa} + k_{rwf})\partial_x P_w = -\frac{kk_{rw}}{\mu_w}\partial_x P_w\,, \tag{6.6}$$

and for the oil phase:

$$u_{oa} = -\frac{kk_{roa}(s_{oa})}{\mu_o}\partial_x P_o\ , \tag{6.7}$$

$$u_{og} = \mathcal{K}_{og} u_{wf} \cdot s_{og}^{mob} = -\frac{kk_{rog}(s, s_{og}^{mob})}{\mu_w}\partial_x P_w \tag{6.8}$$

$$u_o = u_{oa} + u_{og} = -\frac{kk_{roa}}{\mu_o}\partial_x P_o - \frac{kk_{rog}}{\mu_w}\partial_x P_w \tag{6.9}$$

In these equations, k is the absolute rock permeability, μ_w and μ_o are the fluid viscosities, $k_{r\alpha}$ are corresponding relative permeabilities, P_w and P_o are the pressures in the water and oil phase respectively. Equation (6.8) assumes that the flow rate of oil ganglia is proportional to the saturation of mobile oil ganglia s_{og}^{mob} and the average velocity of water films u_{wf} carrying the ganglia, with the proportionality coefficient $\mathcal{K}_{og} = \mathcal{K}_{og}(s, \mu_o, \mu_w)$ that may also depend on saturation. This coefficient reflects the fact that the average velocity of a film differs from the velocity of its surface. The corresponding relative permeability is $k_{rog} = \mathcal{K}_{og} k_{rwf} \cdot s_{og}^{mob}$. Derivation of equation (6.8) is presented in Section 6.5, based on the calculation of capillary conductances carried out in Chapter 5. It is important to point out that

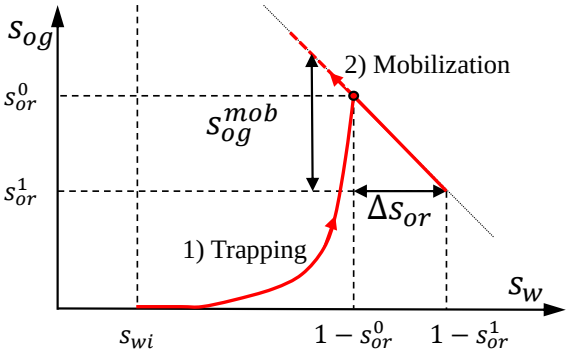

Figure 6.3: Change of oil ganglia saturation during waterflooding.

the resulting flow velocity of the oil phase contains a term proportional to the pressure drop in the water phase, which arises due to the interaction between the two phases.

We neglect the capillary pressure difference, as usual for the Buckley-Leverett scheme [92]. Then the fractional flow function is introduced, determining the amount of water in the flow:

$$f_w(s, s_{oa}, s_{og}^{mob}) = \frac{k_{rw}(s)}{k_{rw}(s) + \dfrac{\mu_w}{\mu_o} k_{ro}(s_{oa}) + k_{rog}(s, s_{og}^{mob})} \tag{6.10}$$

Evolution of oil ganglia saturation is illustrated in Figure 6.3. As the water saturation gradually increases, starting from s_{wi}, the trapping starts. Most of the trapping occurs as saturation approaches $1 - s_{or}^0$ (where s_{or}^0 is the residual oil saturation for "pure" waterflooding). At the point where water saturation is equal to $1 - s_{or}^0$, all the oil is in the form of immobile oil ganglia. Injection of chemical solution will result in the release of part of the trapped oil and formation of mobile oil ganglia. Further, the flow of mobilized ganglia will eventually decrease the saturation of trapped oil to s_{or}^1. It is also possible that mobile oil ganglia form an oil bank. As shown in Figure 6.3, the same value of the water saturation may correspond to the two different oil ganglia saturations, which does not allow to use a closure relation of the form $s_{og} = s_{og}(s)$. This problem will also be discussed in the section devoted to the limitations of the model.

Equations (6.1) to (6.3), (6.5) to (6.6), (6.10) are combined to obtain

$$\phi \partial_t s + \partial_x (u_t f_w) = 0 \tag{6.11}$$

$$\phi \partial_t (sc + s_{wf}(\sigma - c)) + \partial_x \left(\left(c + \frac{k_{rwf}}{k_{rw}} (\sigma - c) \right) u_t f_w \right) = 0 \tag{6.12}$$

where $u_t(t) = u_{wa} + u_{wf} + u_{oa} + u_{og}$ is the overall linear flow velocity determined by the injection rate. We bring system (6.11), (6.12) to dimensionless form in an ordinary way [92]:

$$x_D = \frac{x}{L}, \quad t_D = \frac{u_t}{\phi L} t \tag{6.13}$$

$$c'_a = c_a \,/\, c^J, \quad c'_f = c_f \,/\, c^J \tag{6.14}$$

where c^J is the molar concentration of chemical in the injected water. Substitution of (6.13) , (6.14) into (6.4), (6.11) and (6.12) results in

$$\partial_{t_D} s + \partial_{x_D} f_w = 0 \tag{6.15}$$

$$\partial_{t_D}(s c'_a + s_{wf}(c'_f - c'_a)) + \partial_{x_D}\left(\left(c'_a + \frac{k_{rwf}}{k_{rw}}(c'_f - c'_a)\right) f_w\right) = 0 \tag{6.16}$$

$$\partial_{t_D} c_f{}' = \frac{1}{\tau}\ \overline{c}_f(c_a) \,/\, c^J - c_f \tag{6.17}$$

The initial and boundary conditions assume the form of

$$s(0, x_D) = 1 - s^0_{or}, \quad c'(0, x_D) = 0 \tag{6.18}$$

$$f_w(t_D, 0) = 1, \quad c'(t_D, 0) = 1 \tag{6.19}$$

The dimensionless time $\tau = \kappa u_t / \phi L$ in Eq. (6.17) is the ratio of the relaxation and propagation times. As τ tends to zero (instant relaxation to equilibrium) the species concentration in the film is determined from the equilibrium relationship

$$c_f = \overline{c}_f(c_a) \tag{6.20}$$

The simplest form of dependence (6.20) is the Henry sorption isotherm:

$$\overline{c}_f = \Gamma c_a \tag{6.21}$$

In the non-equilibrium case, the dimensionless relaxation time τ is inversely proportional to the overall length L. While τ is finite under laboratory conditions, it becomes very small on the reservoir scale. Thus, the equilibrium model with the usage of (6.20) instead of (6.17) should be applied to describe the displacement in the reservoir, while the kinetic model with (6.17) is to be applied for modeling the laboratory experiments. In Section 6.6 we present sample calculations for the both cases of sorption and discuss the differences between them.

6.4.1 Features and Limitations of the Model

The most important limitation of the proposed model is that it may only be used for the description of the tertiary, but not secondary recovery processes. In order for it to be valid, it is necessary that the oil saturation is close to its residual value. There are the two reasons for that.

One reason is the assumption of the model that the oil may travel in the form of separate ganglia. If the oil saturation sufficiently differs from the residual value, such ganglia are likely to join the continuous oil phase. The percolation theory argues that most of the sites join the infinite cluster already for the probabilities slightly different from the threshold value [164]. At a current stage of development, the model cannot include both active oil and mobile ganglia. This is the main reason to consider tertiary recovery processes in this study.

Another reason for restricted applicability of the model is that it does not account for the process of trapping/snap off, as discussed above. While the described mechanism requires that the active substance makes the rock surface more water wet, efficiency of trapping is related to wettability in a more complex way. A separate model for dynamic trapping is required.

The proposed model is a two-velocity model for oil movement with the non-instantaneous release of the second oil "phase". This release is supposed to be determined by the wettability conditions; however, this is not important limitation. Any mechanism for non-instantaneous release of a fraction of the oil phase with a possibility of its slow propagation would result in a similar model.

A strong limitation of the presented approach is the necessity for additional constituting dependencies: relative permeabilities $k_{rwf}, k_{roa}, k_{rog}$ and fraction s_{wf}. They should be expressed in terms of the overall saturation s, saturation of mobile ganglia s_{og}^{mob} and concentrations of the additive on the surface and in the solution. In the next section, we discuss a relatively simple model making it possible to determine the corresponding dependencies.

6.5 Macroscopic Saturations and Permeabilities

In this section, we derive the relations for the macroscopic saturation and permeabilities based on the microscopic consideration of a two-phase flow presented in Chapter 1. The derived correlations for flow velocities of water and oil (5.31), (5.34) were obtained for a single capillary and cannot be directly used as the macroscopic permeabilities. An appropriate upscaling technique is required for that. Generally, this model should be based on a certain pore-network model, with successive statistical averaging over all the possible configurations [165]. Here we prefer a simplified treatment, which results in the analytical formula for relative permeabilities, apparently, without loss of the most important physical

effects. In this calculation, we consider porous medium saturated with water and mobile oil ganglia. The active oil cluster is not present, which corresponds to a large overall water saturation of porous medium and may be treated as the model for the flow during tertiary recovery.

A proper upscaling of microscopic conductances should include an ensemble description of a pore-network. We employ a simplified description, to gain insight into typical relations between flow parameters and phase distribution within the system. We consider a cross-section orthogonal to the direction of flow. The average number of capillaries crossing the unit cross-section area is n. Its part $y_{wa} = n_{wa}/n$ is filled with water and belongs to the infinite water cluster. The rest pores are filled with oil, which is disconnected and forms the oil ganglia. Their total oil fraction is $y_{og} = n_{og}/n$. The water films are present in the corners of the oil filled pores; hence, $y_{wf} = y_{og} = 1 - y_{wa}$. Under the assumption that the system is translationally invariant, the saturation and the volumetric flow calculated over a given cross-section will be the same as for the whole system.

The wetting fluid fraction in a capillary is $\omega_w = \omega_w(\theta, P_c)$. It is assumed that θ is constant throughout the system, and that there is a one-to-one correspondence between overall water saturation s and capillary pressure P_c, so that $\omega_w = \omega_w(s)$. The capillary saturation functions ω_α, are defined as:

$$\begin{aligned} \omega_{wa} &= 1 \\ \omega_{wf} &= \omega_w(s) \\ \omega_{og} &= 1 - \omega_w(s) \end{aligned} \tag{6.22}$$

The overall saturations $s_\alpha = \omega_\alpha y_\alpha$ for the whole system may then be calculated as follows:

$$\begin{aligned} s_{wa} &= y_{wa}, \\ s_{wf} &= y_{wf}\omega_w = (1 - s_{wa})\omega_w, \\ s_{og} &= y_{og}(1 - \omega_w) = (1 - s_{wa})(1 - \omega_w) \end{aligned} \tag{6.23}$$

The linear velocity u_α is calculated as the net volumetric flux over the unit cross-section area, using equation (5.20):

$$u_\alpha = n_\alpha q_\alpha = n y_\alpha \omega_\alpha \langle \tilde{v}_\alpha \rangle \frac{4G\mathcal{A}^2}{\mu_w} \partial_x P \qquad \alpha = wa, wf, og \tag{6.24}$$

where q_α is the volumetric flux of the fluid in a capillary, $\mathcal{A}$ is the capillary cross-section area and G is the shape factor of the capillary cross-section, $\langle \tilde{v}_\alpha \rangle$ is the dimensionless velocity in the capillary. The absolute permeability k is determined by the volumetric flux calculated for the single phase problem (5.24):

$$k = \frac{3}{5} n G \mathcal{A}^2 \tag{6.25}$$

The relative permeability is calculated as

$$k_{r\alpha} = \frac{u_\alpha}{k} \frac{\mu_w}{\partial_x P} = y_\alpha \frac{\omega_\alpha \langle \tilde{v}_\alpha \rangle}{\tilde{v}_0} \quad \alpha = wa, wf, og \tag{6.26}$$

Using the correlations for the phase velocities (5.23) and (5.34) we obtain

$$k_{rwa} = s_{wa} \tag{6.27}$$

$$k_{rwf} = \tilde{v}_0^{-1} c_1^w(\tilde{\mu}_o) y_{wf} \omega_w^2 \tag{6.28}$$

$$k_{rog} = \tilde{v}_0^{-1} c_2^o(\tilde{\mu}_o) y_{og} \omega_w^2 (1 - \omega_w) \tag{6.29}$$

Combining (6.23) together with equations (6.28), (6.29) makes it possible to eliminate ω_w, resulting in

$$k_{rwa} = s_{wa}(s) \tag{6.30}$$

$$k_{rwf}(s) = C_{rwf}(\tilde{\mu}_o) \frac{s_{wf}^2(s)}{1 - s_{wa}(s)}, \quad C_{rwf}(\tilde{\mu}_o) = \frac{c_1^w(\tilde{\mu}_o)}{\tilde{v}_0} \tag{6.31}$$

$$k_{rog}(s, s_{og}) = C_{rog}(\tilde{\mu}_o) \frac{s_{og}}{1 - s_{wa}(s)} k_{rwf}(s), \quad C_{rog}(\tilde{\mu}_o) = \frac{c_2^o(\tilde{\mu}_o)}{c_1^w(\tilde{\mu}_o)} \tag{6.32}$$

where $\tilde{\mu}_o = \mu_o / \mu_w$ is the viscosity ratio. Equation (6.32) implies that the flow of the oil ganglia is proportional to the flow of the water films and to the saturation of the oil ganglia, similarly to (5.35). C_{rwf}, C_{rog} are constants that depend on viscosity. The values of these constants may be estimated from equations (5.32), (5.34) with coefficients listed in Tables 5.4, 5.5. The calculated values of these constants for different viscosity ratios are illustrated in Figure 6.4. Alternatively, C_{rwf}, C_{rog} may be treated as adjustable parameters.

In order to use the relative permeability function given by equations (6.30) to (6.32), it is required to specify the water film saturation $s_{wf}(s)$, active water saturation $s_{wa}(s)$ and s_{og}^{mob}. These dependencies are non-trivial and, as discussed earlier, in general, s_{og}^{mob} cannot be introduced as a function of saturation. However, if the active oil phase is not involved, the overall oil saturation is equal to a sum of the mobile ganglia and residual oil saturations:

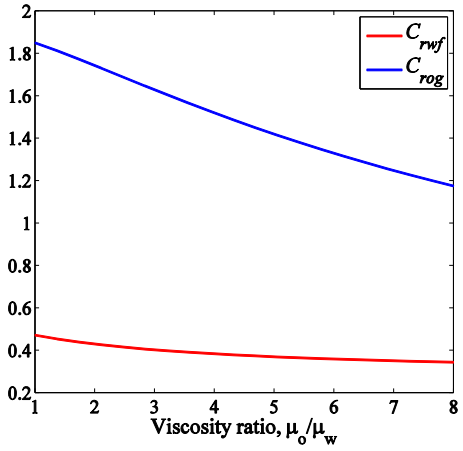

Figure 6.4: Parameters used for the estimation of relative permeability functions of water films and oil ganglia according to the values presented in Tables 5.4, 5.5.

$$\begin{aligned} s_{oa} &= 0 \\ s_{og}^{mob} + s_{or} &= 1 - s \end{aligned} \tag{6.33}$$

Therefore, the possible way to determine saturation of oil ganglia is to specify the dependency of residual oil saturation on the concentration of the chemical:

$$s_{or} = s_{or}(c_f) \tag{6.34}$$

The simplest way to do this is to introduce an interpolation based on the value of c_a and residual oil saturations for flooding with and without chemical – s_{or}^1 and $s_{or}^0 = s_{or}^1 + \Delta s_{or}$ respectively:

$$s_{or}(c_f) = H(c_f)s_{or}^0 + (1 - H(c_f))s_{or}^1 \tag{6.35}$$

We specify $H(\mathrm{x})$ determined by the hyper ellipse curve:

$$H(\mathrm{x};\mathrm{x}_L,\mathrm{x}_R;n_1,n_2) = \left(1 - \left(\frac{\mathrm{x} - \mathrm{x}_L}{\mathrm{x}_R - \mathrm{x}_L}\right)^{n_1}\right)^{1/n_2} \tag{6.36}$$

where x_L and x_R are the boundaries of the interpolation region and n_1, n_2 are parameters that determine the shape of the function. Varying parameters, it is possible to obtain different behavior of the interpolation function, which is shown in Figure 6.5. For the case $n_1 = n_2 = 1$, a simple linear interpolation is obtained. The threshold behavior can be described by $n_1 \gg 1, n_2 \approx 1$. Such an interpolation may be used to describe the case where a change of the

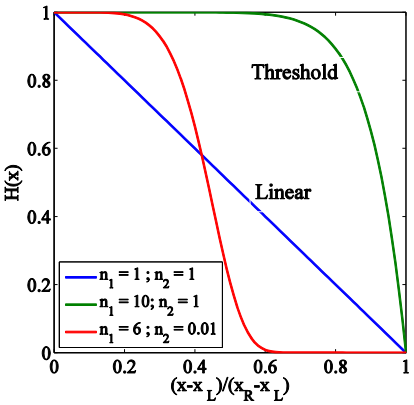

Figure 6.5: Interpolation function used in the model.

residual oil saturation will occur after a certain concentration of chemical in the wetting film is reached. This may happen if the chemical is changing the wetting state of the rock in a threshold-like manner. According to this mechanism of mobilization, the oil is released only when very low values of contact angle are reached, which requires a certain amount of active species to accumulate in the films for the mobilization to start.

At high values of water saturation, all the water is involved in the flow, and it is sufficient to determine only $s_{wf}(s)$ as

$$s_{wa}(s) + s_{wf}(s) = s \tag{6.37}$$

The dependence $s_{wf}(s)$ was determined by simulation of an imbibition process in a pore network [128, 129]. This dependence can be characterized by the following features: at the initial stage of the saturation process the value of s_{wf} grows much faster than s_{wa}, so that $ds_{wf}/ds \approx 1$. At some intermediate saturation s^*, the value of s_{wf} reaches its maximum $s_{wf}^{\max}$ and then decreases almost linearly. As the overall saturation s approaches unity, all the water in the system belongs to the infinite cluster; hence, s_{wf} tends to zero. We apply the following three-parameter model to describe this dependence:

$$s_{wf} = \begin{cases} (s - s_{wi})g_1(s), & s \le s^* \\ (1-s)^m g_2(s), & s > s^* \end{cases} \tag{6.38}$$

where the functions $g_i(s)$ are defined as

$$g_i(s) = 1 - \chi_i \exp(m_i(s - s^*)) \ (i = 1,2) \tag{6.39}$$

These functions are introduced in order to smoothen the shapes produced by equation (6.38) at point s^*. Coefficients χ_i, m_i are selected in such a way that they provide continuity of the

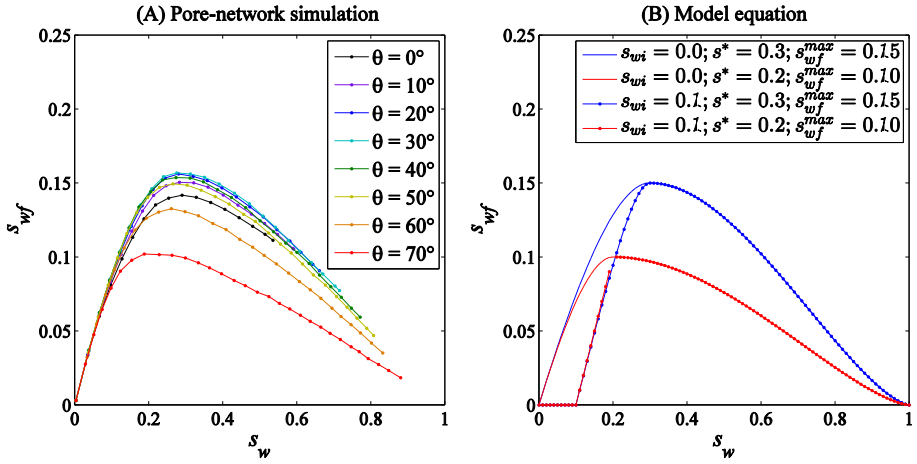

Figure 6.6: Saturation of water films (A) Pore-network simulation; (B) Model equation (6.38)

function and its first derivative. These dependencies contain the three specified parameters: the pair $(s^*; s_{wf}^{\max})$ corresponding to the point of the maximum water film saturation, and parameter m, which indicates how rapidly saturation of the films decreases after reaching its maximum value. Comparison between simulated saturations of the wetting films and model equation (6.38) is presented in Figure 6.6.

Pore network simulations make it possible to establish a relation between the saturation of oil ganglia and the overall water saturation. Even though it is not used in our model, we present these results, since they may hopefully be used for future modeling. The behavior of the oil ganglia saturation function is known from the percolation theory [164, 166]. At low water saturations, trapping is insignificant. It starts when water saturation reaches some intermediate value s^{**}. Further increase in overall saturation results in higher trapping, and finally, as saturation reaches $1 - s_{or}$, all the oil in the system is in the form of ganglia. Further mobilization of ganglia results in a linear decrease of the saturation of the trapped oil phase. Simple two-parametric power-law dependence may be used to describe this behavior:

$$s_{og}(s) = \begin{cases} (1 - s_{or})\left(\dfrac{s - s^{**}}{1 - s_{or} - s^{**}}\right)^l, & s \le 1 - s_{or} \\ 1 - s, \quad s > 1 - s_{or}, \end{cases} \tag{6.40}$$

This equation is valid if no mobile ganglia are present and the local saturation increases with time: $\partial_t s > 0$. If saturation of water decreases again, this does not necessarily result in complete mobilization of the previously trapped oil, and equation (6.41) cannot be applied. The two free parameters in this dependence are s^{**}, a value of saturation at which trapping becomes noticeable, and l which determines the rate of trapping. The comparison between simulated saturations of oil ganglia and model equation (6.40) is presented in Figure 6.7.

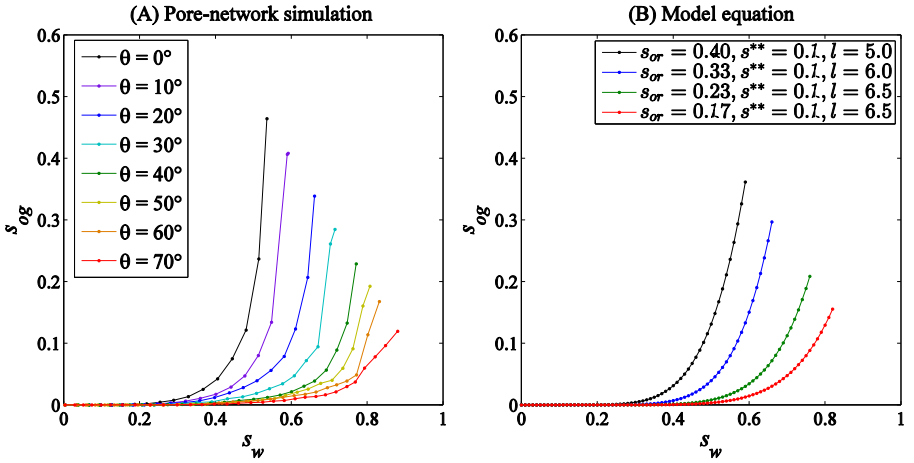

Figure 6.7: Saturation of oil ganglia (A) Pore-network simulation; (B) Model equation (6.40).

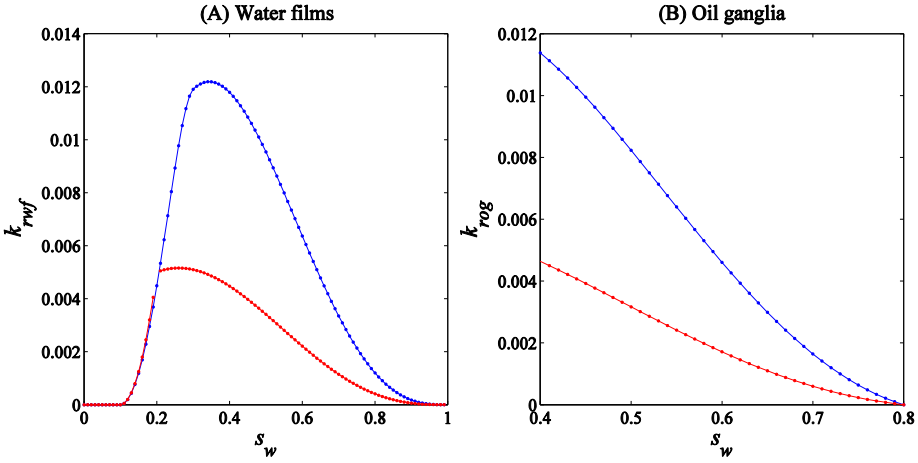

Figure 6.8: Relative permeability functions for (A) water films; (B) mobile oil ganglia. $s_{wi} = 0.1;\ s_{or}^0 = 0.4; \Delta s_{or} = 0.2$; Red: $s^* = 0.2; s_{wf}^{max} = 0.10$; Blue: $s^* = 0.3; s_{wf}^{max} = 0.15$.

The relative permeability functions of water films and mobile oil ganglia, calculated according to (6.31), (6.32) are shown in Figure 6.8 with the use of different parameters.

6.6 Sample Computations

The macroscopic displacement problem described by equations (6.15) to (6.19) combined with relative permeability function given by equations (6.30)−(6.32) and partial saturations determined according to (6.33), (6.37), (6.38) was solved using the second order accurate MUSCL-Hancock with 200 finite volume cells.

Table 6.1: Parameters used for the base-case simulation.

Parameters used for $s_{wf}(s)$:			
$s_{wi} = 0.1$	$s^* = 0.3$	$s_{wf}^{\max} = 0.15$	$m = 2.$
Parameters used for relative permeability functions $k_{rwf}(s)$, $k_{rog}(s)$:			
$C_{rwf} = 0.5$	$C_{rog} = 2.0$		
Parameters controlling change in residual oil saturation:			
$s_{or}^0 = 0.4$	$\Delta s_{or} = 0.2$		

We have performed a number of simulations to study possible outcomes of the proposed mathematical model. First we studied the case where equilibrium concentrations of active species in water films are instantly achieved according to relation (6.21), assuming that concentrations are equal in both bulk water and films ($\Gamma = 1$). The rest of the parameters for the base-case simulation are listed in Table 6.1.

The water with an active chemical changing the wetting state of the rock is injected in a porous medium after waterflooding, as the tertiary recovery method. Initial saturation is equal to the irreducible water saturation s_{or}^0. Injection continues for 20 pore volumes. The saturation profiles for this case are shown in Figure 6.9A. For comparison, we also present the results of the simulations for conventional description of chemical flooding [86, 88] with the same residual saturations.

In both cases, the residual oil bank is formed. If, in our model, the relaxation is instantaneous (that is, the dimensionless relaxation time τ in equation (6.17) tends to zero), the forward front of the oil bank travels together with the chemical concentration front. The solution contains a single shock since the oil bank is followed by gradual increase of water saturation. This is different from the conventional model for chemical flooding where oil bank moves ahead of the concentration front, as shown in Figure 6.9B.

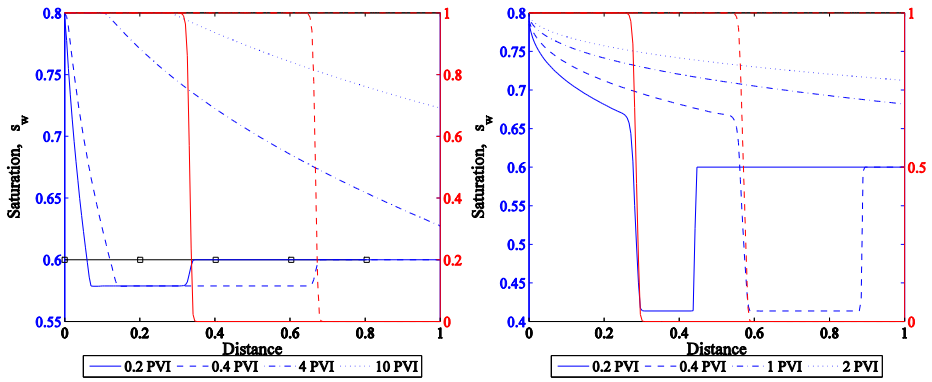

Figure 6.9: Saturation profiles. (Left) Base case; (Right) conventional chemical flooding model. Chemical concentration profiles are shown with red color.

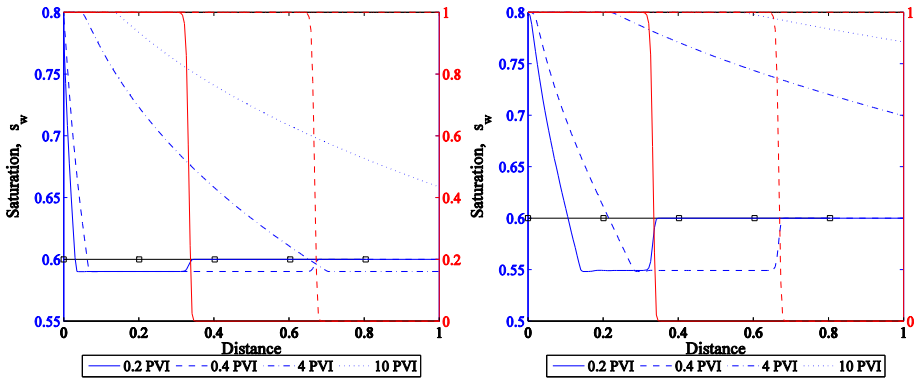

Figure 6.10: Saturation profiles for different relative permeabilities of the wetting films: (Left) $C_{rwf} = 0.25$; (Right) $C_{rwf} = 1.0$. Concentration profiles are shown with red color.

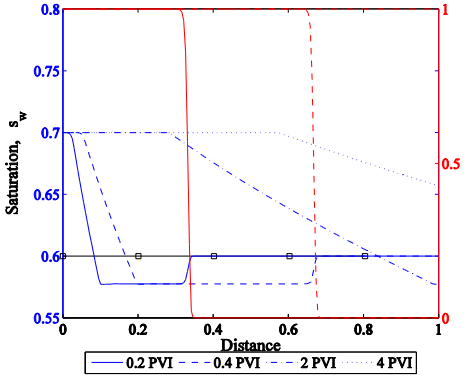

Figure 6.11: Saturation profiles for increased permeability of the wetting films $C_{rwf} = 1.0$ and decreased saturation of mobile ganglia $\Delta s_{or} = 0.1$. Concentration profiles are shown with red color.

In order to study the dependence of the model on the permeability of the water films, we performed a series of simulations with a varying value of C_{rwf}. The results for the doubled and halved value of C_{rwf} are shown in Figure 6.10. The contribution of wetting films to the transport of the chemical is insignificant, as the concentration profiles are not sensitive to variation of C_{rwf}. The permeability of oil ganglia changes proportionally to C_{rwf} according to equation (6.8). Comparison of Figures 6.9A and 6.10 shows that the relative permeability of the oil ganglia affects both the depth of the oil bank and the velocity of the rear edge of the oil bank.

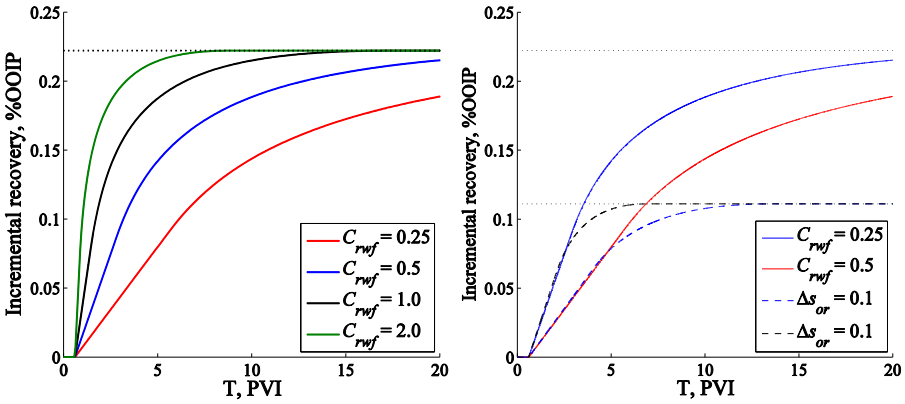

Figure 6.12: Incremental recovery. (Left) Varying the relative permeability of wetting films; (Right) Varying the amount of the mobile oil ganglia.

Variation of the value of Δs_{or} (the maxiumum amount of oil to be mobilized by the chemical) demonstrated similar results. Increasing permeability of wetting films by increasing C_{rwf} twice and reducing Δs_{or} by half almost reproduced the base case curves (Figure 6.11).

The difference may be observed when comparing the incremental recovery curves, shown in Figure 6.12. It illustrates that increased permeability of wetting films allows achieving final recovery faster. Meanwhile, decreasing Δs_{or} allows producing all the mobile oil faster at the same permeability (Figure 6.12B).

Introduction of the non-equilibrium sorption may result in a significant delay of the forward front of the disconnected oil. There are essentially two parameters, which effects should be studied. The first parameter is the dimensionless relaxation time τ, which determines the rate of chemical deposition. The value of τ equal to one corresponds to the deposition rate of $2500\ \mathrm{s}^{-1}$ at a typical laboratory conditions $L = 10$ cm, $u_t = 10^{-5}$ m/s, $\phi = 0.25$. The second parameter is the shape of the interpolation function H, which indirectly determines the rate of oil mobilization. For a linear interpolation function, the rate of oil mobilization is determined by the deposition rate of the chemical; for a non-linear interpolation function the rate of oil mobilization additionally depends on the amount of the active species accumulated in the film.

First, we studied the effect of the sorption kinetics, using the linear interpolation function for the residual oil saturation. In this case, the release of oil starts immediately as chemical starts to accumulate in the water films. The results of simulations with different relaxation times τ are illustrated by the recovery curves in Figure 6.13A. The non-equilibrium kinetics, in this case, does not affect the arrival of the oil bank. The non-instantaneous release of oil ganglia results in a decreased depth of the oil bank as less oil is involved in the flow. This can be seen by a slower increase in recovery after the arrival of the oil bank.

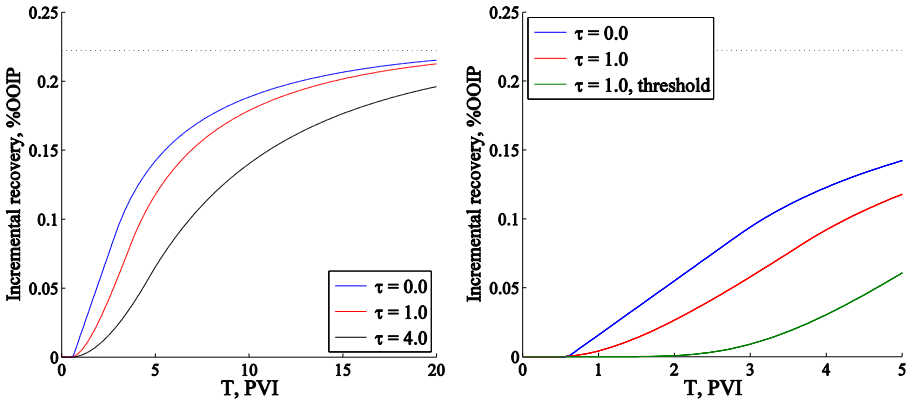

Figure 6.13: Incremental recovery. (Left) Varying the relaxation time; (Right) Varying the behavior of the interpolation function $H(\sigma)$.

Next we changed the interpolation function to account for the threshold behavior, as illustrated in Figure 6.5. The threshold behavior results in the abrupt increase in the amount of mobile oil ganglia only after a certain amount of active species is accumulated in the water films. The recovery curves for this simulation are compared with the base case in Figure 6.13B. Production of the released oil starts after injection of around 2 PV. The delay before the arrival of the oil bank depends on the choice of the relaxation time, as it controls the time required for the chemical to reach the threshold value.

6.7 Conclusions

We have developed a model for chemical flooding accounting for a possible mobilization of the residual oil in the form of ganglia, assuming that the injection of active species (or varying salinity) results in formation of water films, which make the oil ganglia mobile. The model may be used to describe tertiary oil recovery, where the initial oil saturation is close to the residual value.

The numerical solutions for the developed mathematical model were obtained. Our simulations indicate that description of tertiary recovery accounting for oil ganglia has the following important features:

1) Formation of the oil bank. As expected for all tertiary recovery models, the oil bank is formed due to the release of trapped oil (mobilization of oil ganglia). The size of the oil bank is controlled by the amount of mobilizable oil and by the relative permeabilities of the disconnected oil phase (determined by the flow rates of the water films).

2) The velocity of the forward front of the oil bank is controlled by the concentration front of active solute. If the chemical equilibrium between the bulk and the water films is achieved instantaneously, the velocity of the forward front is equal to the propagation rate of the chemical. This result is different from the conventional model of chemical flooding, where the concentration front controls the rear front of the oil bank.
3) Introduction of the non-equilibrium sorption of the active species in the water films will result in a slower increase in recovery with no additional delay of the oil bank.
4) Accounting for threshold behavior of ganglia mobilization may result in additional delay of the arrival of the residual oil bank. The delay may be up to several pore volumes injected (depending on the equilibration time)

7

Analysis of Smart Waterflooding Experiments in Carbonates

7.1 Introduction

In the previous chapters, we have discussed many phenomena that may or might be observed under smart water flooding. Among these phenomena there are: adsorption and ion exchange on the surface (Chapter 2), mineral dissolution (Chapters 2 and 4), mobility of ganglia (Chapters 5 and 6).

It is important to establish, what of these phenomena have been reproduced in the laboratory experiments on smart waterflooding. In the present Chapter, we analyze the available experimental data, trying to extract the mechanisms that were actually observed.

Evidently, this analysis cannot be complete. Some effects, like the mobility of oil ganglia, are proposed in this work for the first time. There have been no laboratory experiments, which were specially designed to observe these effects. Moreover, some effects may probably not be observed in the laboratory, since the involved pore volumes and pressures/injection rates are insufficient for their reproduction. But these effects may still be important on the reservoir scale.

Nevertheless, it is important to analyze the effects that have really been observed and to design a minimum model incorporating them. Then this model might be applied to extract the governing parameters from the experiments that have already been reported in the literature. Other effects could be of less importance or relevance, or would need special experiments in order to observe them.

The chapter is organized as follows. In the following section, we present and discuss the experimental data to illustrate what behavior is to be reproduced by the model. These include the data from both single and two-phase flooding experiments. In Section 7.3 we describe the theory about the surface chemistry of carbonates and present a 1D numerical model developed to perform modeling of flooding experiments. In Section 7.4 we carry out numerical simulations of the one phase flooding in order to verify the model and estimate the parameters that are required by our surface chemistry model. We further use the surface model in our two-phase flow simulations in Section 7.5.

7.2 Summary of Experimental Data

In order to study the surface chemistry, it is important to have experimental data on the single-phase and two-phase flows on the same rock, with measurements of the concentrations of the potential determining ions in the effluent. It is important that fluid injection in the two-phase experiments is fast so that viscous forces dominate or play an important role. Slow experiments on spontaneous imbibition may provide additional information. Also, the fast two-phase experiments should be compared to fast single-phase flow-through experiments for the same rock, where the concentrations of the ions in the effluent are measured.

The necessity to distinguish between fast and slow flows arises since (as we discuss below) there may be two mechanisms that are responsible for ion exchange with the surface. Adsorption of the ions is relatively fast and reversible. Meanwhile, under longer times the irreversible chemical reactions of dissolution-precipitation of the rock become prevailing. Comparison of fast and slow flow-through experiments demonstrates qualitatively different pictures of ion production (see comparison below). That is why fast and slow experiments should be considered separately.

We have selected the experimental data with the flow rates exceeding 5PV per day, or, approximately, 0.1 ml/min. The sets of experiments that have been selected for the present work have been carried out with Stevns Klint rock samples. To the best of our knowledge, the experiments discussed at the present Chapter are the only sets of such experiments that have reported all the necessary parameters, at least, in comparison with each other. We compare single-phase and two-phase such experiments. Separately, we compare fast and slow flow-through experiments and discuss the qualitative difference between the observed distributions of the ions in the produced effluent.

7.2.1 Fast Single-Phase Flow Experiments

An extensive study on the on the wetting properties of carbonates was carried out by Austad and co-workers [5-7, 14, 26, 32, 167]. These experiments were mainly performed with the Stevns Klint outcrop chalk, which is characterized by relatively low permeability of $2-4$ mD, porosity ϕ of $45-50\%$, and weight surface area $\hat{A}_w$ of 2 m^2/g [168]. The amount of impurities is usually low. In most experiments, that we will review, an approximate pore volume of the core plugs was around 40 ml.

A study performed by Strand et al. [32] included spontaneous imbibition tests and chromatographic analysis of the ions in the effluent. The last analysis is important for recovering the simulation parameters for our model and, therefore, will be discussed in detail. The cores were initially 100% saturated with the seawater-like brine containing no sulfate. The brine injected in the core contained sulfate together with thiocyanate (SCN^-) in equal amounts. It is suggested that thiocyanate does not interact with the surface of carbonate, and,

therefore, it can be used as a tracer. The tests were performed at different temperatures of 23, 40, 70, 100 and 130°C. Also, concentration of Ca^{2+} varied between 0.25 and 3 times the concentration in the seawater, while ionic strength was kept constant by adjusting the concentration of NaCl. In particular, Strand et al. [32] have observed that:

- Figure 7.1a: Production of SO_4^{2-} is delayed compared to the tracer SCN^-. This indicates that SO_4^{2-} is likely to reversibly adsorb on the surface. Both retardation and cumulative loss of SO_4^{2-} increases with temperature.
- Figure 7.1b: Decrease in Ca^{2+} effluent concentration is observed if sulfate is present in the injected brine. The cumulative loss of Ca^{2+} increases as more SO_4^{2-} is adsorbed on the surface.
- Figure 7.2: Increasing the Ca/SO_4 ratio results in a larger loss of SO_4^{2-}.

Measurements of the effluent concentrations of potential determining ions allow determining changes in the surface composition. Due to adsorption on the surface, potential determining ions are produced with a delay as illustrated in Figures 7.1, 7.2. The area A between the tracer and sulfate effluent concentration curves allows estimating the amount of sulfate retained in the core. Thus, A can be recalculated into the change of the surface concentration of sulfate $\Delta\sigma_{so_4}$ as the ratio of the losses in bulk $Ac_{so_4}\phi$ to the total surface $\hat{A}_w\rho_s(1-\phi)$:

$$\Delta\sigma_{so_4} = A \times \frac{c_{so_4}\phi}{\hat{A}\rho_s(1-\phi)} \tag{7.1}$$

where $\Delta\sigma_{so_4}$ is expressed in mol/m^2, ρ_s is the rock density. Similar calculations can be performed for Ca^{2+}. In this case the area should be calculated between the effluent concentration curve and relative concentration of one (as concentrations are the same for formation and injected brines and should be constant if adsorption does not take place).

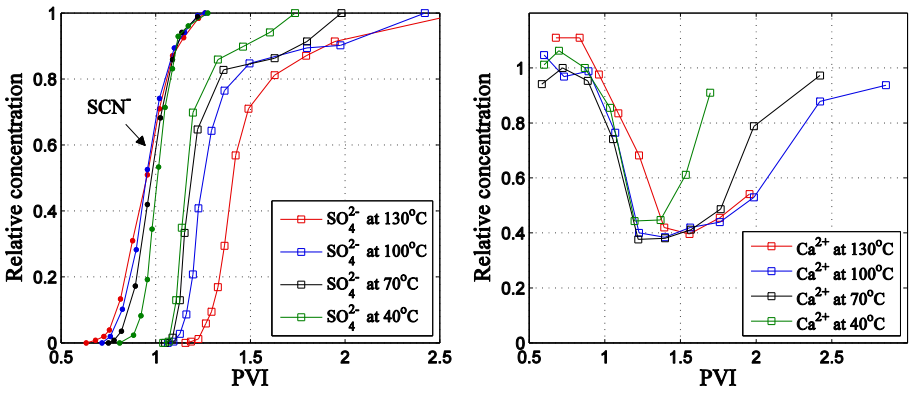

Figure 7.1: Measured effluent concentrations of (a) SCN^- and SO_4^{2-}; (b) Ca^{2+} at different temperatures of 40, 100 and 130 °C. Concentrations are normalized with respect to the injected values. Reproduced after Strand et al. [32].

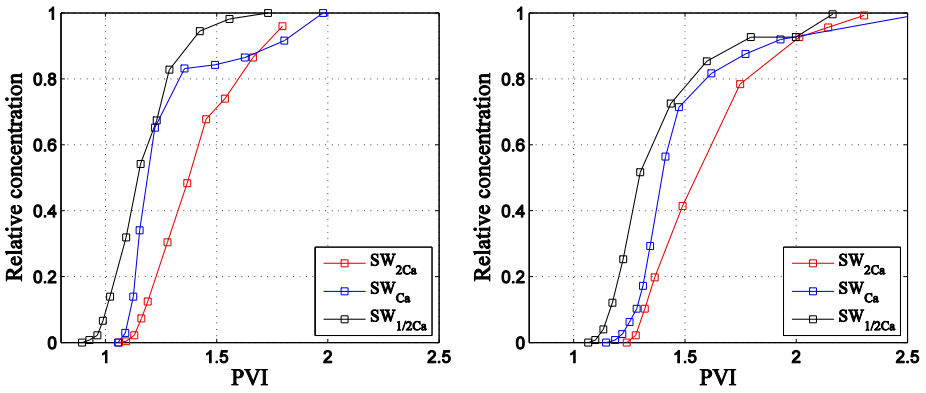

Figure 7.2: Measured effluent concentrations of SO_4^{2-} awith varied concentration of Ca^{2+} in the brines. (a) 130°C; (b) 70°C. Concentrations are normalized with respect to the injected values. Reproduced after Strand et al. [32].

In order to understand the interplay between the two cations we consider the studies of Zhang et al. [5] and Strand et al. [6]. Though different lithology of the rocks may result in different properties, we believe that it is important that more experimental data is presented for further discussion. In the first work affinities of $Ca^{2+}$and Mg^{2+} towards the surface of the Stevns Klint chalk were studied at 23°C and 130°C. The core plugs were initially saturated with 0.573M NaCl brine and flooded with the CF-M brine (see Table 7.1) with equal concentrations of $Ca^{2+}$and Mg^{2+}, while SO_4^{2-} was not present.

Table 7.1: Brine composition for the studies of Strand et al. [32], Zhang et al. [5], Zahid et al. [8]

Ion	SW	SW-U	SW-M	SW1/2Ca	SW2Ca	CF-M	ZP	SW1S	SW0S	SW3S
Na^+	0.560	0.510	0.484	0.472	0.435	0.504	0.573	0.368	0.378	0.348
Mg^{2+}	0.045	0.045	0.045	0.045	0.045	0.013	0.000	0.045	0.045	0.045
Ca^{2+}	0.013	0.013	0.013	0.006	0.026	0.013	0.000	0.013	0.013	0.013
Cl^-	0.525	0.623	0.525	0.524	0.526	0.556	0.573	0.434	0.492	0.317
SO_4^{2-}	0.024	0.000	0.024	0.024	0.024	0.000	0.000	0.024	0.000	0.072
HCO_3^-	0.002	0.002	0.002	0.002	0.002	0.002	0.000	0.002	0.002	0.002
SCN^-	0.000	0.000	0.024	0.024	0.024	0.013	0.000	-	-	-

The study of Zhang et al. [5] on the sorption of cations demonstrates the following:

- Figure 7.3a: At 23°C more Ca^{2+} is adsorbed on the surface.
- Figure 7.3b: At 130°C delay in production of both cations is almost equal. Further increase in Ca^{2+} concentration indicates that Mg^{2+}can substitute Ca^{2+} on the surface.

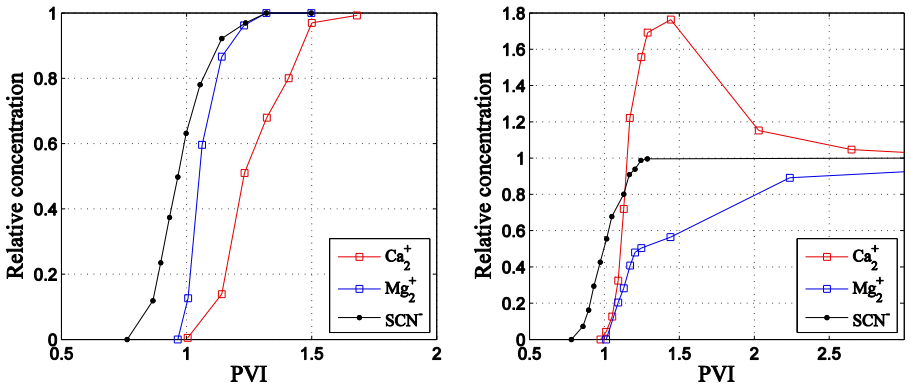

Figure 7.3: Measured effluent concentrations of Ca^{2+}, Mg^{2+} and SCN^-. (a) 23°C; (b) 130°C. Concentrations are normalized with respect to the injected values. Reproduced after Zhang et al. [5]

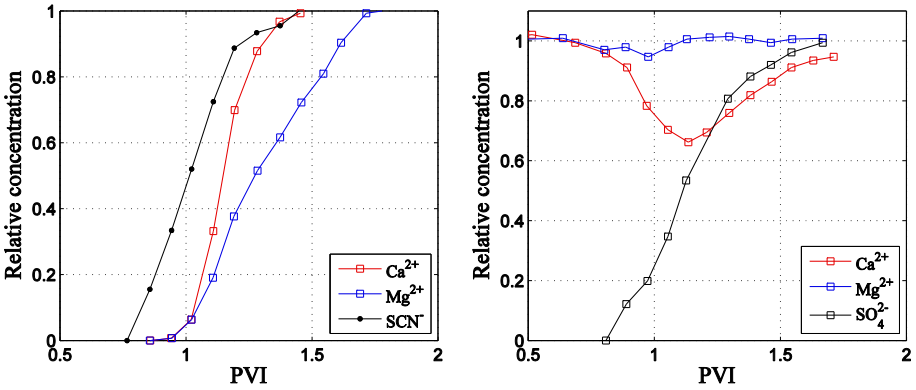

Figure 7.4: Measured effluent concentrations Ca^{2+} and Mg^{2+} with (a) no SO_4^{2-} present; (b) $[SO_4^{2-}]$ = 0.012 mol/l at 130°C. Concentrations are normalized with respect to the injected values. Reproduced after Strand et al. [6].

Now we compare these observations with the data from the similar experiments performed on the limestone cores by Strand et al. [6]. These experiments were carried out with the same brine, at 130°C, with the injection rate of 0.1 ml/min. The following was observed:

- Figure 7.4a: At 130°C Mg^{2+} has higher affinity towards the surface of limestone rock compared to Ca^{2+}.
- No substitution of $Ca^{2+}$by Mg^{2+} is observed (the concentration of calcium in the effluent does not exceed the injected concentration).
- Figure 7.4b: Concentration of Mg^{2+} is not affected if SO_4^{2-} is present in the injected brine, while Ca^{2+} is reduced as expected.

We believe that these observations are not fully consistent with each other, at least, if the ion substitution on the surface is a trusted mechanism. In the absence of sulfate, the magnesium ions are definitely preferred by the surface (Figure 7.4a). Presence of sulfate would reduce the positive surface charges and, therefore, increase this preference. Meanwhile, almost no adsorption of magnesium is observed in the presence of sulfate, while calcium still gets adsorbed (Figure 7.4b). Further discussion of this effect may be found below.

7.2.2 Comparison of Fast and Slow Flow-Through Experiments

Other studies address primarily slow injection of the modified seawater [57, 169]. During slow injection, composition of the brine produced in the effluent is much stronger affected by the mineral dissolution and precipitation reactions, as observed in some of the experiments [5, 57]. Similar to the results described in Chapter 4, presence of mineral reactions will result in the steady-state distribution of the concentrations in the brine between the inlet and outlet [170]. We will list the observations from these studies that are important for further discussion:

- At low injection rates of approximately 0.01 ml/min and high temperatures, increase in Ca^{2+} and an almost equal decrease in Mg^{2+} is observed in the effluent. This may be an indication of calcite dissolution accompanied by the formation of a magnesium-bearing mineral [33].
- SO_4^{2-} can be released from the surface if distilled water is injected [169].

As illustrated by the experimental data, Mg^{2+} can substitute Ca^{2+} both at low and high injection rates. In particular, the two different ways for such substitution should be distinguished. First, the substitution is possible on the sorption sites of the calcite surface due to higher affinity of this surface to the cations. This substitution is expected to increase concentration of Ca^{2+} (at low temperatures) for a short while. However, at high temperatures in several studies [6, 57, 167] a long-lasting substitution of calcium by magnesium was observed: during more than 5 pore volumes of injection, experimentally observed effluent concentrations of both cations were different from their injected values. The changes in cation concentrations were close by absolute value but opposite. Hiorth et al. [33] suggested that this substitution is likely to occur through combined dissolution/precipitation mechanism: dissolution of calcite and subsequent precipitation of magnesium-bearing mineral (e.g. huntite ($Mg_3Ca(CO_3)_4$ as suggested by Madland et al. [34]). This process is observed only at low injection rates and, therefore, should not influence concentrations of Ca^{2+} and Mg^{2+} in the experiments performed under high injection rates.

Sorption is considered to be a fast process, and, therefore, governs the fluid-rock interactions at high injection rates and early stages of flooding. On the contrary, mineral dissolution and precipitation processes are generally characterized by much lower rates [71, 72]. The magnitude of the effect of dissolution and precipitation on the concentrations in brine is determined by the ratios of the reaction rates to the convective flow rates (as expressed by

the Damköhler numbers). It depends on the rates of reactions, flow velocity and the distance between the inlet and outlet. The reaction rates of the brines with the carbonates may vary several orders of magnitude [76]. Therefore, exact determination of the Damköhler numbers is impossible. However, the results of the considered experiments look like the slow-rate experiments are carried out with the Damköhler numbers of the order of unity while the fast experiments correspond to the numbers much less than one. Forced core flood experiments are usually performed with high injection rates $q^{inj} > 0.1$ ml/min on the core plugs with a typical length of 10 cm. For such experiments it is likely that mineral reactions are slow compared to convective transport and have only minor effect on ion concentrations. It is additionally confirmed by the discussed experiments. In all of them concentrations of the potential determining ions were reaching their injected values after at least 3 pore volumes of injection (Figures 6.1−6.4), while in cases of irreversible chemical reactions this would never happen. For that reason, mineral reactions are not considered in our model for fast experiments.

7.2.3 Two-phase Flow Experiments

We consider now the two-phase flooding experiments performed by Zahid et al. [8]. One of the reasons for this particular choice is that these experiments were also performed on the Stevns Klint outcrop chalk. Other studies were performed on the carbonate reservoir and outcrop cores [21, 30] and demonstrated that potential of the smart water flooding is also dependent on a rock material.

In the experiments conducted by Zahid et al. [8] the core plugs were completely saturated with oil and flooded at different temperatures of 40, 90, 110 and 130°C, with the injection rate of 5 PV/day (approximately 0.1 ml/min). The brines used in these experiments were similar to the ones used in the chromatographic studies, with a slightly lower ionic strength (see Table 7.1).

No aging was performed after core saturation and, therefore, the rock could be considered to be completely water wet, as some amount of water was possibly still present in the rock in a form of the wetting films. Most tests were performed with the Latin American (LA) oil (density 0.846 g/cm^3, viscosity 13.3 cP, AN = 0.163 mg KOH/g, BN = 0.563 mg KOH/g). Only four tests were carried out with the North Sea (NS) and the Middle East (ME) oils. These oils are different mainly by acid and base numbers: for North Sea oil: AN = 0.095 mg KOH/g, BN = 2.442 mg KOH/g; for Middle East oil: AN = 0.093 mg KOH/g, BN = 0.644 mg KOH/g. Table 7.2 summarizes the data on the oil recovery for these experiments. Some of the recovery curves are also presented in Figure 7.5.

We will briefly summarize the observations for the experiments involving the Latin American and the Middle East oils:

- Final recovery achieved by seawater without sulfate (SW0S) remains similar at all the temperatures. Perhaps, a small increase is observed at higher temperatures.
- Injection of seawater (SW1S) and seawater reach in sulfate (SW3S) after SW0S brine in all cases resulted in additional recovery.
- Under equal temperatures, the effect SW3S injection was more pronounced compared to the injection of SW1S brine.
- Recovery for the injection of both SW1S and SW3S brines increased with temperature.
- Additional oil was produced within approximately 1 PV of injection.

An increase of recovery with temperature for the injection of SW0S brine may be partially explained by a more favorable mobility ratio. Viscosity of oil at low temperatures is relatively high and is expected to decrease when the temperature is raised.

Secondary flooding experiments demonstrated similar oil recoveries for all types of oil used in the study. Meanwhile, the increase in recovery with SW3S brine during tertiary flooding was negligible in Test 10, performed with the North Sea oil. It is not clear what factor caused the difference. One of the influencing factors is, perhaps, a much higher base number of the North Sea oil. However, we believe that the number of experiments with the North Sea oil is not sufficient to make far going conclusions.

Similar increases in recovery were observed in the secondary and the tertiary recovery modes, which indicates that history of flooding does not influence the final state of the rock surface. As under secondary flooding, the additional recovery was observed within approximately 1 PV of injection. The oil banks seem to come before or simultaneously with the concentration fronts. There is no reason to assume the action of the ganglia mechanism that was modeled in Chapter 6. Therefore, modeling of the available experimental data may be carried out within the standard models of two-phase flow with the convection-dispersion mechanism of the propagation of the ions, and accounting for adsorption of these ions on the rock surface. There is no seeming reason to go for a more complex model, at least, based on the available experimental data.

7.2.4 Discussion of the Experimental Data

Probably, the most controversial data are presented in Figures 6.3 and 6.4. First of all, the calculated area A_{ca} between the tracer and Ca^{2+} effluent concentration curve (Figure 7.3) is -0.535. Negative value of A_{ca} indicates that Ca^{2+} is not accumulated in the core due to adsorption; instead, the produced amount of Ca^{2+} is larger than injected. The formation brine (ZP) does not contain any Ca^{2+} and, therefore, there are the two possibilities: 1) a sufficient amount of Ca^{2+} was initially adsorbed on the surface, but for some reasons could not desorb

Table 7.2: Summary on the final recovery achieved by waterflooding of oil saturated Stevns Klint chalk in the studies of Zahid et al. [8]

Test	Oil	Brines	T, °C	Rate	Recovery, %
1	LA	SW0S → SW1S	40	5 PV/day	64.0 → 65.1
2	LA	SW0S → SW3S	40	5 PV/day	62.0 → 64.0
3	LA	SW0S → SW1S	90	5 PV/day	60.3 → 63.9
4	LA	SW0S → SW1S	90	5 PV/day	60.8 → 64.2
5	LA	SW0S → SW1S	110	5 PV/day	63.0 → 67.5
6	LA	SW1S	110	5 PV/day	68.0
7	LA	SW3S	110	5 PV/day	73.5
8	LA	SW0S → SW3S	130	1 PV/day	65.7 → 71.4
9	LA	SW3S	130	1 PV/day	72.1
10	NS	SW0S → SW3S	110	5 PV/day	62.5 → 63.8
11	NS	SW3S	110	5 PV/day	70.1
12	ME	SW0S → SW3S	110	5 PV/day	68.1 → 71.5
13	ME	SW3S	110	5 PV/day	75.9
14	LA	SW0S	110	5 PV/day	64.9
15	LA	SW3S	110	5 PV/day	70.2

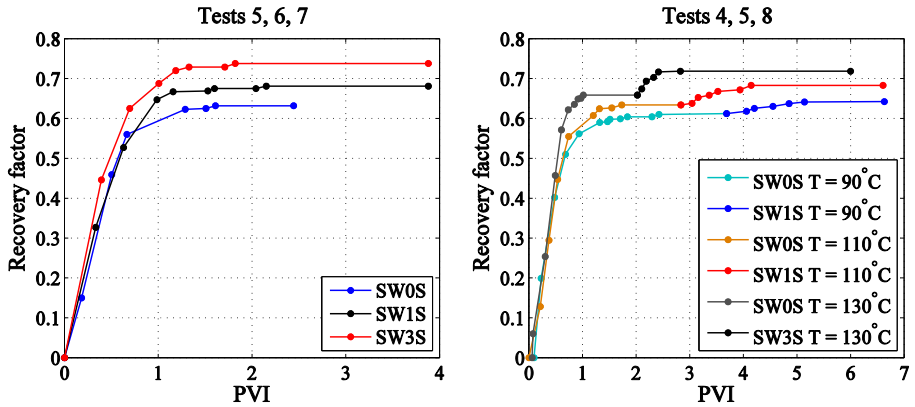

Figure 7.5: Recovery curves for waterflooding of oil saturated Stevns Klint chalk. (Left) Injection of brines with different concentrations of sulfate in the oil saturated core at 110°C. (Right) Injection of sulfate containing brines (SW1S and SW3S) after residual oil saturation was achieved with the sulfate-free brine (SW0S) at different temperatures. Reproduced after Zahid et al. [8]

when the rock was saturated with NaCl brine; 2) an additional source of calcium should be considered (e.g. from the mobile fines contained in the core). In both cases the assumption about stronger adsorption of Mg^{2+} is questionable.

Another argument against the statement about stronger adsorption of Mg^{2+} at high temperatures is that the delay in breakthrough for both cations is identical (Figure 7.3). Meanwhile, stronger adsorption of Mg^{2+} should have resulted in a larger delay compared to Ca^{2+}. Additionally, the behavior of the Mg^{2+} production curve at 130°C changes at 1.2 PV (Figure 7.3), where it seems to be controlled by a slower substitution mechanism.

It is important to mention that substitution of Ca^{2+} by Mg^{2+} was not observed in experiments performed on the limestone cores (Figure 7.4a). Mg^{2+} was still slightly stronger adsorbed on the surface in the absence of sulfate. This implies that on the injection of seawater in the core, the variation of the Mg^{2+} concentration should be greater than that of Ca^{2+}. The results of the corresponding experiment, shown in Figure 7.4b, do not confirm the expected behavior: only substantial decrease of Ca^{2+} concentration is observed while concertation of Mg^{2+} remains unchanged.

Finally, there is a question of the repeatability of the experimental data. Most of the presented experiments were performed once, and the range of variation in the measured effluent concentration curves is not known.

If we compare observations from the flow-through experiments and two-phase displacement experiments, there is an indication that increase in recovery corresponds to a change in the surface composition. The analysis of the experimental data indicates that

- Conditions favorable for recovery: increased temperature and larger concentration of sulfate in the injected brine, correspond to an increased concentration of sulfate on the surface.
- Adsorption of sulfate has an effect on adsorption of calcium and magnesium through the change of the surface charge.

Hence, a minimum model fitting reasonably reproducible results of the experiments should include consideration of the surface composition. Adsorption of all of the potential determining ions should be considered simultaneously and the surface charge should be introduced as a parameter governing the adsorption process.

7.3 Model Formulation

In this section, we describe the mathematical model to account for the adsorption of potential determining ions on the surface of the rock and its effects on the flooding efficiency. This is achieved by combining the surface chemistry model with a 1D Buckley-Leverett model presented in Chapter 2. The single phase flow is described as a special case with water saturation equal to unity. For the two-phase flow, the parameters determining the relative permeability curves are assumed to be dependent on the surface concentrations of adsorbed ions. This approach is similar to the one used in modeling of the low salinity effects on waterflooding [171].

7.3.1 Surface Chemistry

A model for description of the surface chemistry should take in account that adsorption of the different ions takes place on the charged surface of calcite. This charge changes the

affinity of ions towards the surface. A relevant description is provided by the surface complexation model of carbonate surface developed in [5, 6, 33, 55, 172]. Analysis of these studies reveals a certain variation in parameters that are used for modeling of fluid-rock interactions.

According to the model, adsorption of potential determining ions takes place on two different surface complexes: $> CO_3^-$ and $> CaOH_2^+$. Exchange reactions between surface sites and aqueous species, that were presented in Chapter 2, result in the following possible configurations of surface complexes (species): $> CO_3^-$, $> CO_3H^0$, $> CO_3Ca^+$, $> CO_3Mg^+$, $> CaOH^0$, $> CaOH_2^+$, $> CaSO_4^-$, $> CaCO_3^-$. Several studies [33, 55] on thermodynamic equilibria of carbonate surface in contact with seawater-like brines claim that at pH from 7 to 9, and low bicarbonate concentrations the most abundant surface species are: $> CO_3^-$, $> CO_3Ca^+$, $> CO_3Mg^+$, $> CaOH_2^+$, $> CaSO_4^-$. Therefore, it is sufficient to account only for the following adsorption reactions:

$$>CO_3^- + Mg^{2+} \rightleftarrows >CO_3Mg^+ \tag{7.2}$$

$$>CO_3^- + Ca^{2+} \rightleftarrows >CO_3Ca^+ \tag{7.3}$$

$$>CaOH_2^+ + SO_4^{2-} \rightleftarrows >CaSO_4^- + H_2O \tag{7.4}$$

Presence of charged complexes on the surface results in non-zero surface charge density δ_s which is calculated according to:

$$\delta_s = \mathcal{F}\sum_{a_s} z_{a_s}\sigma_{a_s} \tag{7.5}$$

where summation is performed over all charged surface species; σ_{a_s} represents the surface concentration of the species in $[\mathrm{mol/m^2}]$; and $\mathcal{F}$ is the Faraday constant, $\mathcal{F} = 96485\ \mathrm{C/mol}$.

An important parameter that influences the sorption capacity of the surface is the site density d_s, which for carbonate rocks is estimated to be between 2 and 5 $\mathrm{sites/nm^2}$ [33, 55] and equal for both $> CO_3^-$ and $> CaOH_2^+$. The site density can be recalculated into sorption capacity: $T_s = d_s/N_A = 3.32$ to $8.85\ \mu\mathrm{mol/m^2}$. We estimate the number of moles of aqueous species per unit surface of the rock to be around $1.85\ \mu\mathrm{mol/m^2}$ for 0.01M solution. A large value of T_s indicates that the surface can accommodate large amounts of adsorbed species and has strong influence on the brine composition. It is also convenient to describe composition of the surface in terms of the surface mole fractions:

$$\beta_{a_s} = \sigma_{a_s} / T_s \tag{7.6}$$

Applying eq. (7.6) one can express the surface charge density in terms of surface mole fractions of the potential determining ions:

$$\delta_s = 2\mathcal{F}T_s(\beta_{ca} + \beta_{mg} - \beta_{so_4}) \tag{7.7}$$

The surface charge density determines the surface potential ψ_s, which affects activities of ions close to the surface. The surface potential is calculated using the Gouy-Chapman theory [75, 82]:

$$\delta_s = \sqrt{8\varepsilon\varepsilon_0 RT \cdot I \times 10^3}\,\sinh\left(\frac{\mathcal{F}\psi_s}{2RT}\right) \tag{7.8}$$

where ε is the dielectric constant of water, ε_0 is the permittivity of the free space, $\varepsilon_0 = 8.854 \times 10^{-12}\ \mathrm{C}^2/(\mathrm{m}\cdot\mathrm{J})$, R is the universal gas constant, T is the absolute temperature, I is the ionic strength (molal).

The equilibrium conditions for the surface reactions (7.2)–(7.4) are described by the mass action equations:

$$K_1 = \frac{[>\mathrm{CO_3Mg^+}]}{[>\mathrm{CO_3^-}][\mathrm{Mg^{2+}}]} \cdot \chi^2 \tag{7.9}$$

$$K_2 = \frac{[>\mathrm{CO_3Ca^+}]}{[>\mathrm{CO_3^-}][\mathrm{Ca^{2+}}]} \cdot \chi^2 \tag{7.10}$$

$$K_3 = \frac{[>\mathrm{CaSO_4^-}][\mathrm{H_2O}]}{[>\mathrm{CaOH_2^+}][\mathrm{SO_4^{2-}}]} \cdot \chi^{-2} \tag{7.11}$$

$$\chi = \exp\ \mathcal{F}\psi_s\ /\ RT \tag{7.12}$$

where [X] denotes the activity of a species X; K_1, K_2 and K_3 are equilibrium constants dependent on temperature. Additional exponential term χ accounts for the interactions of the ions with the charged surface. It decreases the activities of ions with the charge of the same sign as that of the surface, and increases the activities of species with opposite charge.

The activities of the surface species are taken to be equal to their mole fractions β_{a_s} [72]. The activities of species in the aqueous solution are related to molar concentrations: $a_a = \gamma_a c_a / c_a^{\ominus}$, where $c_a^{\ominus}$ is the reference concentration. The activity coefficients γ_a can be calculated with the Davis equation:

$$\log_{10}\gamma_a = -Az_a^2\left(\frac{\sqrt{I}}{1+\sqrt{I}} - 0.3I\right) \tag{7.13}$$

where A is the temperature dependent constant and z_a is the valence of the species. In our model we account also for complexation between potential determining ions: $CaSO_4(aq)$ and $MgSO_4(aq)$. Formation of complexes is more pronounced at high temperatures and can significantly affect the activity of Mg^{2+}. In order to take this into account we performed the PHREEQC simulations [173] for the seawater (SW and SW1S in Table 7.1) varying the concentration of SO_4^{2-}, and computed the activity coefficients for Ca^{2+}, Mg^{2+} and SO_4^{2-} as functions of c_{so_4}. For a given temperature these dependences were used to calculate the activity coefficients of the potential determining ions.

The surface mole fractions for complexes $> CO_3^-$ and $> CaOH_2^+$ are $\beta_X = 1 - \beta_{ca} - \beta_{mg}$ and $\beta_Y = 1 - \beta_{so_4}$ respectively. Based on equations (7.9)–(7.11), the equilibrium surface mole fractions can be expressed in the form:

$$\bar{\beta}_{mg} = \frac{K_1 \chi^{-2} a_{mg}}{1 + K_1 \chi^{-2} a_{mg} + K_2 \chi^{-2} a_{ca}} \tag{7.14}$$

$$\bar{\beta}_{ca} = \frac{K_2 \chi^{-2} a_{ca}}{1 + K_1 \chi^{-2} a_{mg} + K_2 \chi^{-2} a_{ca}} \tag{7.15}$$

$$\bar{\beta}_{so_4} = \frac{K_3 \chi^{2} a_{so_4}}{1 + K_3 \chi^{2} a_{so_4}} \tag{7.16}$$

It should be noted that apparent similarity of sorption isotherms (7.14)–(7.16) with Langmuir sorption isotherms is misleading. The electrostatic exponential term χ is dependent on $\bar{\beta}_{a_s}$, and therefore the equilibrium surface composition cannot be calculated explicitly.

Dielectric permittivity of water appears in equation (7.8) and is known to vary with temperature and ionic strength of brine [174, 175]. The variation with temperature is from 80 at 23°C to 50 at 130°C. We applied the correlation for the permittivity suggested in [25]. Ionic strength in the discussed experiments was kept around the same level, hence, we assume ε to be constant. However, we believe that effect of ionic strength may be pronounced when salinity of the brine varies significantly (e.g. low salinity flooding).

The input parameters, that are required by this surface chemistry model are:

- Equilibrium constants for adsorption reactions K_1, K_2, K_3.
- Site density d_s (we apply d_s = 5 sites/nm^2).
- Specific surface area of the rock.

7.3.2 The Transport Model

Below we present the 1D transport model for a two-phase flow of water (*w*) and oil (*o*). It is based on the Buckley-Leverett model for incompressible fluids [92]. It was described in details in Chapter 2; here we will briefly outline the major points. The equations for the single-phase flow are a special case of the derived system with the water saturation equal to unity.

The flow of phases is determined according to the generalized Darcy law:

$$u_\alpha = -k\lambda_\alpha \partial_x P \quad \alpha = w, o \tag{7.17}$$

where k is the absolute permeability, λ_α is the phase mobility, P is the pressure. Additional dependence on the molar fractions of adsorbed species is introduced in the phase mobilities λ_α. This is done in Section 7.5 by correlating observed experimental oil recovery with the predicted equilibrium surface composition for different brines and temperatures.

We assume that initially present formation brine is in equilibrium with the surface of the rock, corresponding to the composition β_a^0 of the adsorbed species. As saturation increases, part of the surface α_r is put in contact with the injected water, while the rest is in contact with the formation water. Therefore, adsorption process takes place only on the fraction α_r of the surface, and composition β_a^0 remains unchanged on the fraction $1 - \alpha_r$ of the surface. The global concentrations of adsorbed species (per unit volume of the porous medium) are given by:

$$c_a^* = \hat{A} T_s (\alpha_r \beta_a + (1 - \alpha_r)\beta_a^0) \tag{7.18}$$

where $\hat{A}$ is the specific surface area in $\mathrm{m}^2/\mathrm{l(core)}$. Porosity and absolute permeability are considered to be constant and fluids are assumed to be incompressible. This results in constancy of the linear flow velocity u_t:

$$u_t = u_w + u_o = -k(\lambda_w + \lambda_o)\partial_x P \tag{7.19}$$

Therefore, we can use the fractional flow formulation and disregard pressure from the computations. The system of material balance equations for the components is obtained in accordance with the description given in Chapter 3:

$$\phi \partial_t s_w + u_t \partial_x f_w = 0 \tag{7.20}$$

$$\partial_t (\phi s_w c_a + \hat{A} T_s (\alpha \beta_a + (1 - \alpha)\beta_a^0)) + u_t \partial_x (c_a f_w) = 0 \tag{7.21}$$

$$\partial_t (\hat{A} T_s (\alpha_r \beta_a + (1 - \alpha_r)\beta_a^0)) = \dot{r}_a^{sorb} \quad a = \mathrm{Ca}, \mathrm{Mg}, \mathrm{SO}_4 \tag{7.22}$$

where $\dot{r}_a^{sorb}$ is the sorption rate, which we is defined as follows:

$$\dot{r}_a^{sorb} = \alpha_r \hat{A} k_a^{sorb} (\chi^{-z_a} IAP^{+} - IAP^{-} \,/\, K_a) \quad a = \mathrm{Ca}, \mathrm{Mg}, \mathrm{SO}_4 \tag{7.23}$$

where IAP^{+} and IAP^{-} are the ion activity products for a forward and backward reactions, as defined in (7.2)–(7.4), and K_a' includes the electrostatic term χ. For the reaction of magnesium sorption the rate law (7.23) reads:

$$\dot{r}_{mg}^{sorb} = \alpha_r \hat{A} k_{mg}^{sorb} (a_{mg} \beta_X - \beta_{mg} \,/\, (K_1 \chi^{-2})) \tag{7.24}$$

Sorption rates for the rest of the reactions (7.3), (7.4) are calculated correspondingly. This approach allows calculating both equilibrium and non-equilibrium surface reactions by tuning the reaction rate constants. The limiting case of the infinite rate constants corresponds to the equilibrium sorption [92].

The fraction of the reactive surface in contact with brine $\alpha_r \in [0,1]$ should be related to saturation. It increases with saturation between zero, for a fully oil saturated core, and one, for a fully water saturated core. The simplest model is

$$\alpha_r = s_w \tag{7.25}$$

The effect of pore-size distribution and presence of wetting films are likely to modify this dependence. At this stage of the model development, the actual dependence on the saturation was found not to play an important role and we use equation (7.25) without any modifications.

7.3.3 Numerical Model

The numerical methods used in our studies were covered in Chapter 3. We used the finite volume formulation with discretized domain consisting of 80 cells. The ratio of the time step to the space step was 1/10. With this choice, the numerical diffusion was of the same order of magnitude as the typical values of the convective diffusion in a porous medium. The match was assessed by comparison of the tracer effluent concentration curves in experiments and model calculations since dispersion is the only mechanism affecting the wash-out of the tracer production curves.

The advection and reaction terms were treated separately. According to this approach, each time step is split into advection and reaction sub-steps. During the advection sub-step, only transport terms are considered in equations (7.20), (7.21) and solution for saturation and new aqueous concentrations is updated using forward Euler method. During the reactions step only equations containing reaction terms (7.22) are considered. The reaction step was treated implicitly. The solution of the system of non-linear equations representing (7.22) was obtained using the solver from the Fortran minpack library [111].

7.4 Numerical Modeling of the Single Phase Experiments

All the simulations presented in this work were performed with the constant sorption rate constants k_a^{sorb}. The choice of significantly large rate constants results in contracted transition zone of species concentrations between injection and formation values compared to the experimental curves. Usage of significantly small rate constants results in earlier breakthrough and broad transitions zone with intermediate concentrations. We found that the choice $k^{sorb} = \{300{,}300{,}600\}\,\mathrm{mol \cdot s^{-1}/m^3(core)}$ resembled the width of the transition zone observed in the experiments relatively well.

As a first step, we performed modeling of the co-adsorption of Ca^{2+} and SO_4^{2-} and compared it with the experimental data from the study of Strand et al. [32]. As concentration of Mg^{2+} is not reported in the study, there is an ambiguity in determining the equilibrium constants K_a and different sets of K_a can give a reasonable fit. The values used in our simulations were obtained using a trial and error method. We also compared the equilibrium constants with the rest of our simulations, requiring that all equilibrium constants K_a are of the same order of magnitude as reported in [33, 55]. Table 7.3 summarizes the equilibrium constants used in our simulations. Simulation results for these experiments are shown in Figures 7.6, 7.7.

Table 7.3: Summary on the equilibrium constants used in simulations

Description	T, °C	K_1	K_2	K_3	Figure
ZP → CF-M	23°C	20	50	–	7.10
SW-U → SW-M	23°C	20	50	30	7.6
SW-U → SW-M	40°C	20	70	35	7.6
SW-U → SW-M	70°C	30	80	40	7.8
SW-U → SW-M (xCa)	70°C	15	120	45	7.9
SW-U → SW-M	100°C	60	120	60	7.7
ZP → CF-M	130°C	1000	200	–	7.11, 7.12
SW-U → SW-M	130°C	100	200	110	7.7, 7.8
SW-U → SW-M (xCa)	130°C	55	300	120	7.9

At low temperatures of 40°C and 70°C the model captures the qualitative behavior reasonably well (Figure 7.6). It clearly demonstrates that adsorption of sulfate on the surface will result in additional adsorption of Ca^{2+} from the solution, as observed by the decreased effluent concentration. Same is true for the simulations performed at high temperatures (Figure 7.7). In this case, the discrepancy with experimental data is more significant for the concentration of Ca^{2+}, while the effluent concentration of SO_4^{2-} is reproduced relatively well. The main inconsistency is that our model does not predict a long-term decrease in calcium concentration. According to model formulation, adsorption of sulfate results in the co-adsorption of cations, therefore, variation of concentrations should be observed at the effluent during a similar time.

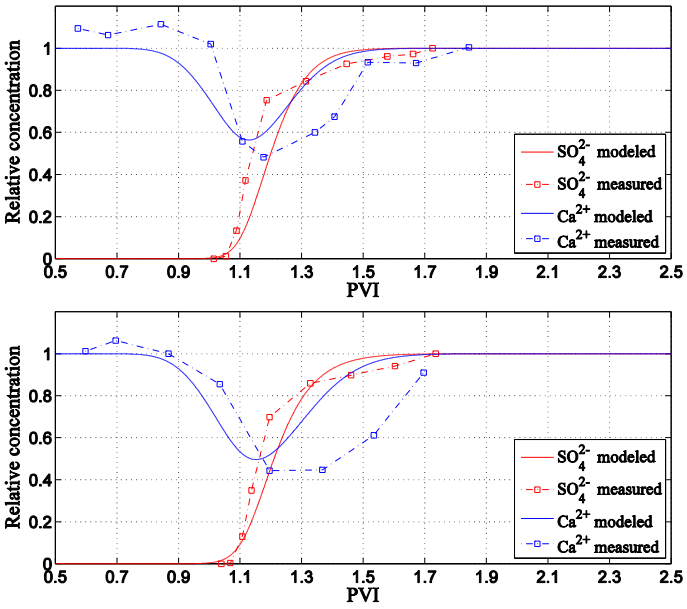

Figure 7.6: Modeled and experimentally measured effluent concentrations of $Ca^{2+}$and SO_4^{2-} at low temperatures: (Upper) 23°C ($K_1 = 20, K_2 = 50, K_3 = 30$); (Lower) 40°C ($K_1 = 20, K_2 = 70, K_3 = 35$). SW-M brine is injected in the chalk core initially saturated with SW-U brine.

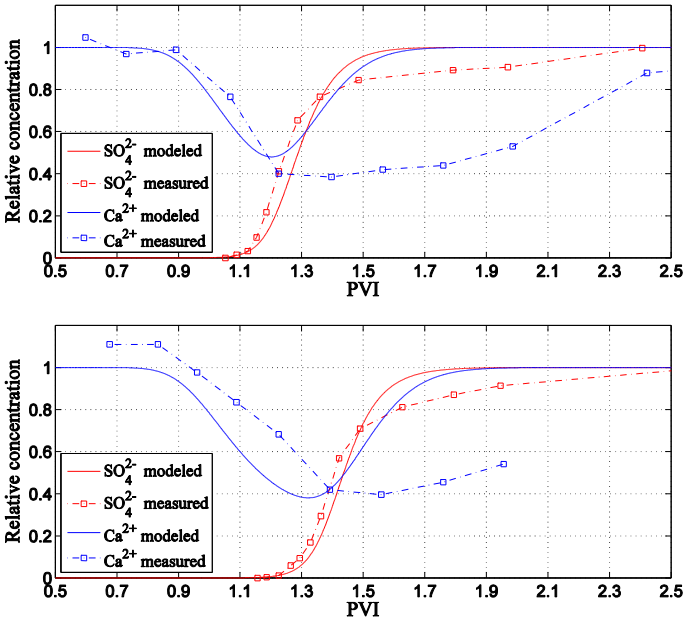

Figure 7.7: Modeled and experimentally measured effluent concentrations of $Ca^{2+}$and SO_4^{2-} at high temperatures: (Upper) 110°C ($K_1 = 60, K_2 = 120, K_3 = 60$); (Lower) 130°C ($K_1 = 100, K_2 = 200, K_3 = 110$). SW-M brine is injected in the chalk core initially saturated with SW-U brine**.**

The model is not able to reproduce the long climb of concentrations towards the injected values after the breakthrough. In order to understand, what can cause this behavior, we checked for the possibility $CaSO_4^{2-}$ precipitation. Using the PHREEQC software, we computed anhydrite saturation index for the seawater (SW-M brine) at different temperatures. This analysis showed that with seawater concentrations no precipitation is expected, even at high temperatures. Moreover, if precipitation would be involved and could affect concentrations, the effluent concentrations would not be expected to reach their injected values after 2.5 – 3 PVI, as it was observed in all of the experiments. We are not sure what changes in the model are required to eliminate the inconsistency.

For this set of experiments we also calculated the change in the surface concentrations of Ca^{2+} compared to those of SO_4^{2-} according to equation (7.1); the results obtained are listed in Table 7.4. It can be seen from the calculated values that change of the surface concentration of Ca^{2+} is close to that of sulfate. This is not what should have been expected. Indeed, if the assumption that Mg^{2+} is stronger adsorbed on the surface is valid, this would immediately mean that $\Delta\sigma_{mg} > \Delta\sigma_{ca}$. As a result, the surface charge should increase (as $\Delta\sigma_{mg} + \Delta\sigma_{ca} > \Delta\sigma_{so_4}$), which is controversial: injection of seawater resulting in adsorption of sulfate should decrease the surface charge. This explains why we are using $K_2 > K_1$ both at low and high temperatures. Thus, our modeling suggests that during interaction of seawater with calcite, a stronger preference of Mg^{2+} to the surface compared to that of Ca^{2+} should be reconsidered.

Table 7.4: Comaprison on change in surface concentrations of Ca^{2+} and SO_4^{2-}

	23°C	40°C	70°C	100°C	130°C
$\Delta\sigma_{ca}/\Delta\sigma_{so_4}$	0.45	0.71	0.98	0.90	–

The next step of model verification was to study the effect of the Ca/SO_4 ratio on the surface adsorption on the basis of experimental data from the work of Strand et al. [32]. Initially, we used the same sets of equilibrium constants in our simulations. The results of these simulations for at 70°C and 130°C are presented in Figure 7.8. Adsorption of sulfate increases with increasing Ca/SO_4 ratio, which is confirmed by the increased retardation of sulfate in the modeling. However, we observed much less sensitivity of sulfate effluent concentration curves to the variation of Ca/SO_4 ratio compared to the change of the sulfate effluent concentrations in the experiments.

The main reason for low sensitivity to the change of the Ca/SO_4 ratio may be that concentration of Mg^{2+} is 4 times larger than those of Ca^{2+} and has a similar affinity towards the surface. Therefore, variation of calcium concentration does not strongly affect equilibrium surface composition. Increasing K_2 and decreasing K_1 resulted in a better description of the effluent curves (Figure 7.9). This is consistent with the conclusion that strong adsorption of Mg^{2+} at high temperatures is questionable.

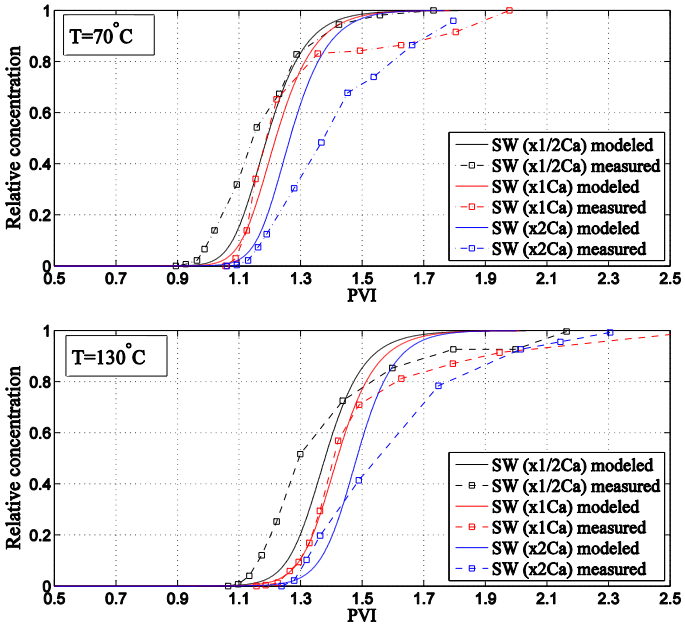

Figure 7.8: Modeled and experimentally measured effluent concentrations of $Ca^{2+}$and SO_4^{2-} at (Upper) 70°C ($K_1 = 30, K_2 = 80, K_3 = 40$); (Lower) 130°C ($K_1 = 100, K_2 = 200, K_3 = 110$). Concentrations of Ca^{2+} were varied in the injected brine.

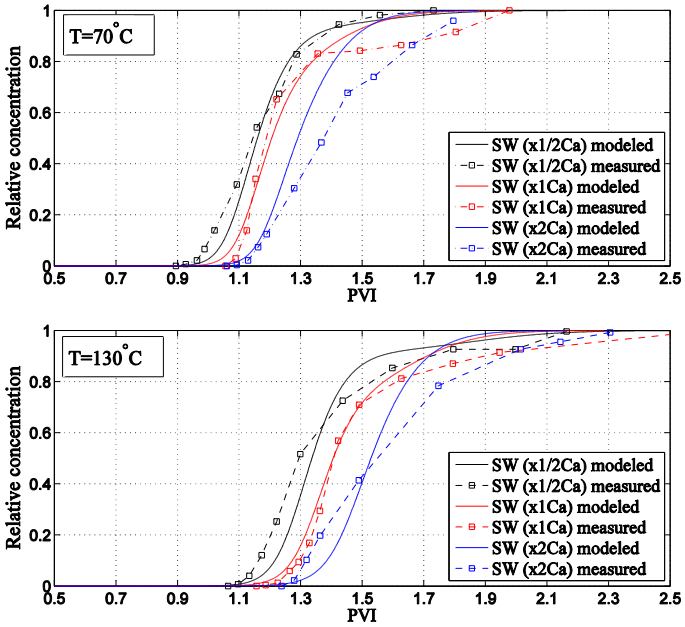

Figure 7.9: Modeled and experimentally measured effluent concentrations of $Ca^{2+}$and SO_4^{2-} at (Upper) 70°C ($K_1 = 15, K_2 = 120, K_3 = 45$); (Lower) 130°C ($K_1 = 55, K_2 = 300, K_3 = 120$). Concentrations of Ca^{2+} were varied in the injected brine.

Finally, we performed simulations to study competitive sorption of $Ca^{2+}$and Mg^{2+} on the surface in the absence of sulfate (experimental data of Zhang et al. [5]). Modeling of competitive sorption of cations at 23°C is illustrated in Figure 7.10 and was performed with $K_1 = 20, K_2 = 50$. Our results indicate that a higher affinity of Ca^{2+} ($K_2 > K_1$) should result in an increase of the effluent concentration of Mg^{2+}, which was not observed in the experiment. This increase is not significant and is around 5-10% with our choice of equilibrium constants.

Results of simulation for a similar experiment performed at 130°C are shown in Figure 7.11. To achieve a significant increase in Ca^{2+} concentration we had to increase the ratio of the equilibrium constants K_1/K_2 to 5. Still, the discrepancy between model predictions and experiment is high. Our results indicate that stronger adsorption of one of the cations in our model will always result in an increase in the effluent concentration of the second cation. The magnitude of this increase is proportional to the ratio of equilibrium constants.

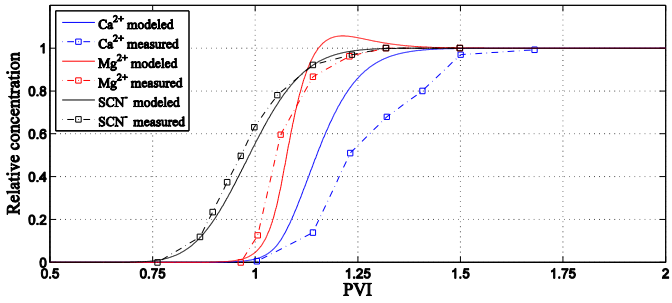

Figure 7.10: Modeled and experimentally measured effluent concentrations of Ca^{2+}, Mg^{2+} and SCN^- at 23°C. CF-M brine is injected in the chalk core initially saturated with ZP brine. $K_1 = 20$, $K_2 = 50$

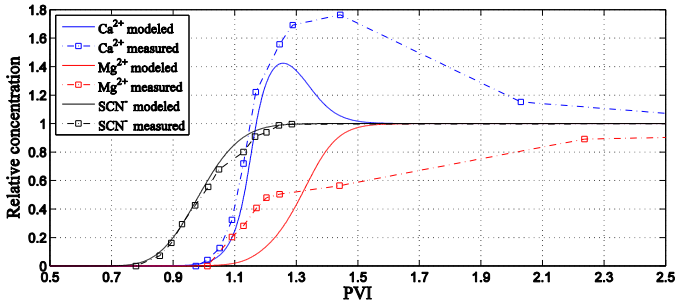

Figure 7.11: Modeled and experimentally measured effluent concentrations of Ca^{2+}, Mg^{2+} and SCN^- for 130°C . CF-M brine is injected in the chalk core initially saturated with ZP brine. $K_1 = 1000$, $K_2 = 200$.

Results of simulation for a similar experiment performed at 130°C are shown in Figure 7.11. In order to achieve a significant increase in Ca^{2+} concentration we had to increase the ratio between equilibrium constants to $K_1/K_2 = 5$. Still, the discrepancy between model predictions and experiment is high. Our results indicate that stronger adsorption of one of the cations in our model will always result in an increase of the effluent concentration of the second cation. The magnitude of this increase is proportional to the ratio of equilibrium constants.

In the discussion section, we pointed out that in this particular experiment Ca^{2+} is produced from the core. In order to achieve this, it is required that the adsorbed $Ca^{2+}$is initially present on the surface. We accounted for this possibility by setting a low value of Ca^{2+} in the ZP brine (0.573M NaCl): $c_{ca} = 0.001$ mol/l and a negative initial surface charge (to allow for more calcium on the surface). In this case the increase in the effluent concentration of Ca^{2+} was more similar to the one observed in the experiments (Figure 7.12). However, the delay between Ca^{2+} and Mg^{2+} breakthrough also significantly increased.

One of the possible explanations for inaccurate reproduction of these experimental data is the simplifications introduced in the model by neglecting some of the surface complexes. In the absence of sulfate, the complex $>CaCO_3^-$ that we do not consider in this study would affect the adsorption of calcium and magnesium. Because concentration of HCO_3^- in the injected brines is low $c_{HCO_3} = 0.002$ mol/l, it is possible that equilibrium concentrations are achieved after sufficient amount of brine is injected which is observed on the experimental curves (Figure 7.11). Probably, full surface complexation model of carbonate surface described in Chapter 3 should be used in order to provide a better match for this experiment.

The results presented in this section indicate that our model can qualitatively reproduce the interaction between brines and the chalk surface. The match, however, is not accurate. In order to improve the reliability of modeling, it is important to assess the repeatability of the experiments, to know how broad the variation in the effluent concentrations curves is. Such

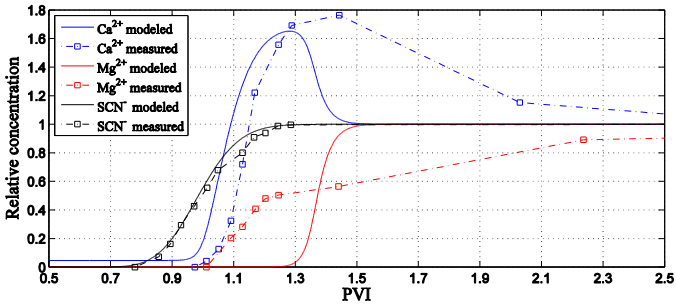

Figure 7.12: Modeled and experimentally measured effluent concentrations of Ca^{2+}, Mg^{2+} and SCN^- for 130°C. CF-M brine is injected in the chalk core initially saturated with ZP brine with c_{ca} = 0.001 mol/l. $K_1 = 1000$, $K_2 = 200$.

information is rarely reported due to obvious experimental difficulties. Also, more experiments that report concentration of Mg^{2+} are required in order to understand the interplay between the competitive adsorption of cations.

The equilibrium constants used in this study require additional investigation. In general, we were not able to identify a unique set of equilibrium constants that can be used to model all the single-phase experiments examined in our study. We compared our values of equilibrium constants with those used in other studies [33, 55]. They are of the same order of magnitude; the difference can be partially explained by the fact that different site densities are used in the models. A larger surface site density corresponds to lower equilibrium constants, in order to provide similar surface concentrations.

7.5 Numerical Modeling of Water Flooding in Oil Saturated Core

In this section, we demonstrate the application of the model to the smart water injection into the oil saturated cores. Sulfate has been recognized as one of the ions, which presence is crucial for the additional recovery with smart water. We performed calculations of the equilibrium concentrations of potential determining ions in contact with the brines used in the study of Zahid et al. [8]. Based on these calculations, it may be deduced that surface fractions of adsorbed sulfate correlate with the observed increase in recovery (see Figure 7.13). Therefore, the smart water effect is introduced in the model by the dependence of the fractional flow function on β_{so_4}.

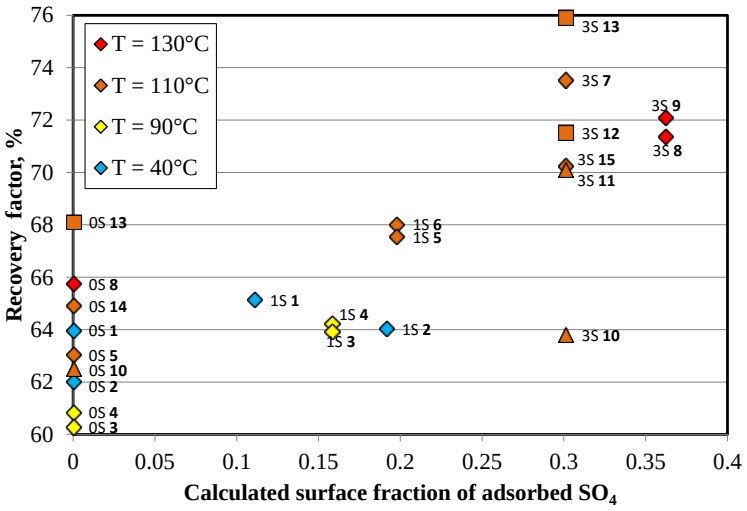

Figure 7.13: Comparison of the predicted surface fractions of the adsorbed SO_4^{2-} and the recovery factor from the experiments of Zahid et al. [8]. Diamond marker is used for the Latin American oil, triangle for the North Sea oil, square for the Middle East oil. Data labels indicate the concentration of sulfate and corresponding experiment.

A possible way to apply this information would be to pick Corey parameters for each particular experiment and to introduce dependence of the relative permeabilities on β_{so_4}. We follow an alternative approach:

- For each test from Table 7.1 calculate the sulfate surface fractions β_{so_4}. These surface fractions are determined by the brine composition (concentration of sulfate) and temperature.
- Correlate the residual oil saturation observed in the tests with β_{so_4}.

$$s_{or} = \langle s_{or} \rangle + b \cdot \beta_{so_4} \tag{7.26}$$

  where b is constant.
- For a secondary recovery, experiment performed with SW1S or SW3S set

$$s_{or} = \bar{s}_{or} + b \cdot \beta_{so_4} \tag{7.27}$$

  where $\bar{s}_{or}$ is the average residual oil saturation for flooding with SW0S at a given temperature.
- For a tertiary recovery, experiment performed with SW1S or SW3S set

$$s_{or} = s_{or,\mathrm{SW0S}} + b \cdot \beta_{so_4} \tag{7.28}$$

  where $s_{or,SW0S}$ is the residual oil saturation after flooding with SW0S brine.

Usage of linear correlation of the form (7.26) is justified by considering Figure 7.13, where final recovery is plotted versus the calculated sulfate surface fractions. It demonstrates that linear fit is sufficient to describe the effect. The resulting value of linear coefficient b is found to be approximately -0.25.

For the experiments that do not involve the injection of sulfate we estimate the Corey parameters, using the Welge method [176]. The pressure drops are not reported in the experiments of Zahid et al. [8], and the dependence of oil viscosity on temperature is not known. Hence, determination of relative permeabilities is impossible, and only the fractional flow function may be found from the experimental data. According to the definition of the fractional function and Corey-type relative permeabilities from Chapter 2, one can write

$$\begin{aligned} f_w &= \frac{1}{1 + \dfrac{\mu_w}{\mu_o}\dfrac{k_{ro}}{k_{rw}}} = \frac{1}{1 + \dfrac{\mu_w}{\mu_o}\dfrac{k_{rowi}}{k_{rwor}}(1 - s_{wi} - s_{or})^{n_o - n_w}\dfrac{(s - s_{wi})^{n_w}}{(1 - s_{or} - s)^{n_o}}} \\ &= \frac{1}{1 + \Lambda\dfrac{(s - s_{wi})^{n_w}}{(1 - s_{or} - s)^{n_o}}} \end{aligned} \tag{7.29}$$

According to the above equations, the fractional flow function requires three parameters to be determined: Λ and two Corey exponents n_w, n_o. The following parameters were obtained on the basis of provided experimental data:

$$\Lambda = 2.4; \quad n_w = 2.2; \quad n_o = 1.1 \tag{7.30}$$

The results of the simulations for secondary and tertiary recovery modes are presented in Figure 7.14. A good match between the simulation results and the experimental data can be observed. This results also indicate that the major change in the fractional flow function is mainly due to the change of the residual oil saturation while other Corey parameters experience much less variation.

As can be seen from the Figure 7.14, the model can both over- and underestimate the predicted recovery. The misfit is mostly noticed in modeling the displacement involving the brine reach in sulfate (SW3S). The experimental data show also a much broader variation in recovery with SW3S flooding. Therefore, this inaccuracy may be partially explained by the uncertainty in the recovery from different cores.

It is important to notice that the model reproduces relatively well an increase in the recovery factor during tertiary injection (Figure 7.14b). The oil bank is produced within 0.5 to 1 PV of injection. Results of our simulations indicate that in studied case the flow of oil,

mobilized by the injection of smart water, is likely to be governed by the same flow mechanism as during the secondary flooding. The discrepancy between simulation results and experimental data for SW3S flooding at 130°C is probably due to a lower injection rate of 1 PV/day used in the experiment. For this slow experiment, dissolution and precipitation reactions could affect the concentrations of the potential determining ions during flooding.

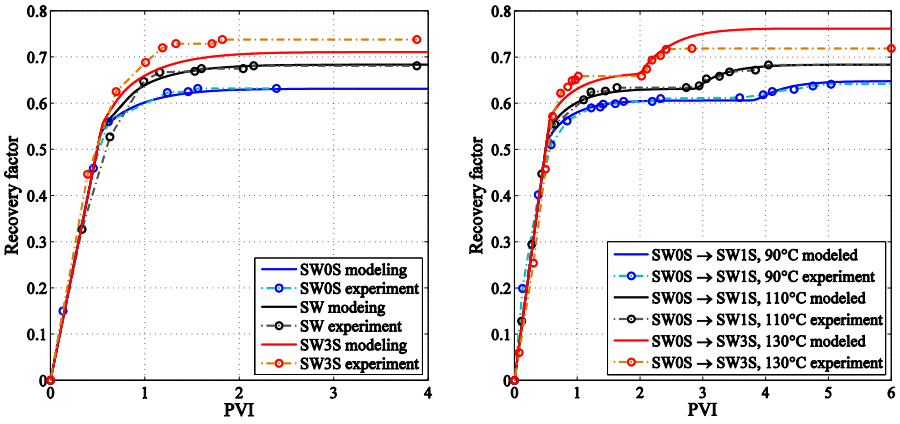

Figure 7.14: Comparison of numerical modeling and experimental data from the work of Zahid et al. [8]. (Left) Injection of brines with different concentrations of sulfate in the oil saturated core at 110°C. (Right) Injection of sulfate containing brines (SW1S and SW3S) after residual oil saturation was achieved with the sulfate-free brine (SW0S) at different temperatures.

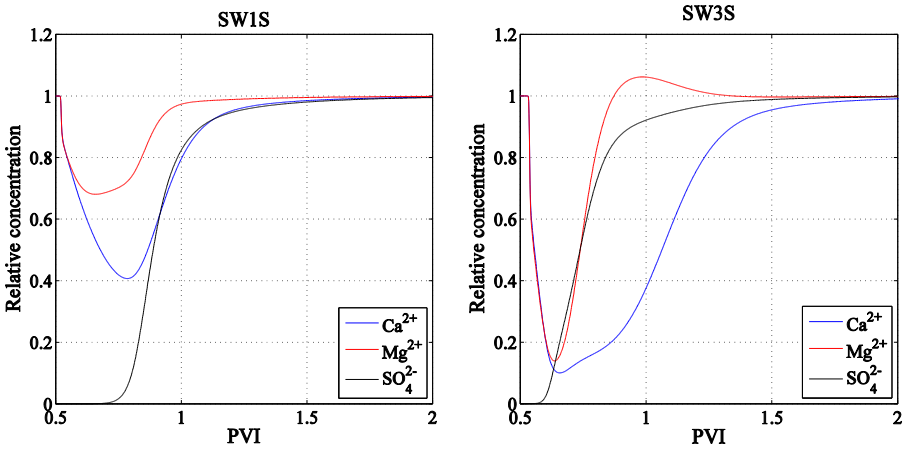

Figure 7.15: Predicted effluent concentrations of Ca^{2+}, Mg^{2+} and SO_4^{2-} for core flooding experiments at 110°C. (Left) Flooding with SW1S; (Right) flooding with SW3S.

Predicted effluent concentrations of potential determining ions for flooding experiments performed with SW1S and SW3S at 110°C are shown in Figure 7.15. We do not present the effluent concentrations for the rest of the simulations as they exhibit similar behavior. It can be seen from Figure 7.15 that concentration of a cation that has a higher affinity towards the surface is affected much stronger and requires more pore volumes of injection to reach its injected value. For the injection of SW3S, insignificant increase in Mg^{2+} concentration is also observed. This implies that analysis of the effluent concentrations of water produced during two-phase flow experiments should exhibit behavior similar to those observed in single-phase experiments. Therefore, such analysis can also be utilized to improve predictive capabilities of the model.

7.6 Conclusions

We presented a 1D numerical model for continuum scale simulation of the one- and two-phase flow in porous medium accounting for the adsorption of potential determining ions. The model assumes that adsorption of sulfate can improve recovery by affecting relative permeability functions, mainly by decreasing residual oil saturation. For a sound interpretation of the experimental data, it is necessary to distinguish between reversible adsorption of the ions during fast displacement experiments and irreversible chemical substitution during the slow experiments. These two groups of the experiments should be considered separately.

By comparison of the simulation results with the experimental data, we conclude that the model is able to qualitatively reproduce single phase flow experiments. However, the accuracy of data matching is low and further development of the model is required here.

Application of the model to the displacement of the oil by smart water predicts the increase in oil recovery with a good match with the experimental data. The recovery is well correlated with the presence of the sulfate ions. This indicates that the proposed simplified model incorporates the recovery mechanisms that have been observed in the experiments. Further development of the model is required in order to transfer the results onto the reservoir scale, where slow chemical mechanisms may play a higher role.

The main conclusions that we draw from this study are:

1) The relative affinity of Ca^{2+} and Mg^{2+} changes with temperature. Some of the experimental data suggest that Mg^{2+} will substitute Ca^{2+} on the surface at high temperatures, while other data probably indicate that Mg^{2+} is inert towards the surface. The results of the modeling suggest that adsorption of Ca^{2+} should be stronger at high temperatures if sulfate is present.
2) At high temperatures, the model is not able to catch long-term decrease in Ca^{2+} concentration. The results of the modeling suggest that this should not be related to the slower mechanisms of adsorption on the surface.
3) Concentrations of the potential determining ions in the water produced during two-phase flow should exhibit behavior similar to those of the single-phase flow. Therefore, we suggest that presenting data on the composition of the produced water is essential for all the kinds of smart water flooding experiments.
4) Modeling of the two-phase flow flooding experiments indicates that incremental recovery can be correlated to the change of the surface concentration of sulfate.

Conclusions and Future Work

Understanding of the factors that control the enhanced oil recovery during the smart waterflooding in carbonate rocks is essential, since a considerable part of the hydrocarbon reserves is contained in carbonate reservoirs. To improve this understanding, we addressed several phenomena related to the smart water flooding, such as mineral dissolution, surface chemistry of the carbonate rocks, and mechanisms that influence mobilization of trapped oil and its transport. More specifically,

- In Chapter 4 we presented a reactive transport model for the displacement problem accounting for the fluid compressibility. Dissolution of the rock material was affecting both the porosity/permeability of the rock and the density of the brine. It was demonstrated that the velocity of the displacement front was slightly affected by the non-additivity of the volumes under dissolution: the difference of individual volumes of the mineral in solid and in solution. Contrary to our expectations, no significant effect of non-additivity on the pressure was observed. We studied the effect of the dissolution rate and observed that fast dissolution resembles formation of wormholes with a significant change in porosity and permeability close to the injection site. However, modeling in multiple dimensions is required to investigate these effects more thoroughly.
- In Chapter 5 we presented a micromodel for the two-phase flow in a single pore body represented by an angular capillary. We performed numerical simulations to study the effect of mutual presence and flow of the two fluids. The results of the study indicate that presence of the water on the surface of the rock and in the corner filaments of angular capillaries increases the velocity of the viscous flow of the oil phase. We explain this phenomenon by the increased area of the moving boundary of the oil-water interface. In the case of zero pressure drop in the oil phase, the flow of oil may be induced by the action of viscous forces at the oil-water interface, which appears to be a new mechanism for the transport of disconnected oil ganglia in porous media. We found that the flow velocity of the oil ganglion is proportional to the average flow velocity of the water present in the corner filaments.
- In Chapter 6 we develop a macroscopic model to take into account the effects associated with oil trapping and mobilization. We suggest that mobilization of trapped oil ganglia may occur due to increasing wetness of the rock caused by the presence of an active substance in the injected brine. According to the results of Chapter 5, the flow of oil ganglia is slow as it is determined by the flow of the water films. Results of numerical modeling of the tertiary recovery process indicate that

production of oil ganglia may continue for a long time of injection of around 10 to 20 PVI. An important finding is that with the ganglia mobilization mechanism, the oil bank travels behind the concentration front of the active substance. This result is different from the predictions of the conventional model of chemical flooding, where production of mobilized oil starts earlier than production of a chemical in the effluent. Introduction of the non-equilibrium alteration of wettability and non-instantaneous oil mobilization may be used to explain the delay observed in some experiments, where mobilized oil is produced after several pore volumes of the smart water injection.

- In Chapter 7 we established a model to describe the interaction between an aqueous solution and chalk during fast flooding experiments. Analysis of the available flow-through experiments indicates that during flooding at high injection rates the brine-rock interactions are determined by adsorption of the potential determining ions, while both adsorption of ions and mineral reactions should be considered at low injection rates and in spontaneous imbibition experiments. We estimated the parameters that are used for the adsorption model by fitting the effluent concentrations observed in the flow-through experiments. The computations suggest that there is no evidence of usually assumed stronger adsorption of magnesium ion compared to calcium at high temperatures. We combined the adsorption model with the Buckley-Leverett model to perform simulations of the two-phase flow experiments performed on the water-wet outcrop chalk [8]. Computation of the equilibrium surface composition demonstrated a correlation between the concentration of the adsorbed sulfate and the ultimate recovery observed in the experiments. Therefore, it might be suggested that a more negatively charged surface of carbonate can be a factor that affects the recovery efficiency without wettability modification.

Suggestions for Future Work

Considering the work and results presented in this thesis, it is clear that there are still major uncertainties associated with the smart water flooding phenomena. The directions in which the work can be extended include the following:

- Oil-water and oil-rock interactions. More generally, this direction may be described as the chemical theory of wettability in carbonates. Surface complexation models [55] of the carbonate and the oil surfaces can be used to study the link between the brine composition, concentrations of surface species and the polar oil components. This will require introducing a number of poorly determined parameters, such as equilibrium constants for the adsorption reactions at the oil-water interface and the area of the interface. These constants are to be found in more refined experiments, e.g. with the oil adhesion on the surface of calcite.

- A more realistic description of transport of the oil ganglia. We suggest that further improvement of the oil ganglia model is required. The model should be extended to account for the following possible processes: ganglia coalescence, retrapping and transport in a pore network with varying capillary sizes. In order to make further conclusions about the applicability of the model, it is also necessary to take into account the end effects at the core facets.
- The effect of mineral dissolution and solid precipitation on the concentrations of the potential determining ions should be considered. The dissolution and precipitation reactions play an important role at lower injection rates. Considering displacement on the reservoir scale, both ion exchange on the surface and geochemical reactions should be taken in account.
- Inclusion of the capillary effects. Flooding in fractured carbonate reservoirs requires accounting for both the viscous flow in the fractures and spontaneous imbibition in the oil-wet porous matrix. For that reason, description of flooding in a core and in a heterogeneous reservoir may be significantly different. Due to the slowness of spontaneous imbibition process, this would require to consider the mineral dissolution and precipitation reactions as suggested above.
- Involvement of the migration of fines. It has been suggested that the fine migration can be a reason for the smart water effects during injection of low salinity brine in the sandstone and carbonate rocks. The effect of fines is associated with pore throat blocking and diversion of the flow paths. The effect of fines migration cannot be described adequately using only the macroscopic approach. However, it may be studied within the framework of the deep bed filtration theory, which should incorporate a physicochemical model of the interaction between the diluted aqueous solution and the surface of the rock.
- Geometry of the pore space should be described in more detail. It was observed that smart water flooding in outcrop and reservoir cores can produce different results. If the mineralogy of the rocks is similar, another reason that may cause the difference should be found. One of the possibilities is to introduce the effect of the pore size distribution, through a mesoscopic model based on the ensemble of pores [177]. This approach can be applied to describe a number of phenomena related to the smart water effect and petrophysical experimental procedures including fines migration, heterogeneous wettability and its alteration, the NMR measurements.

Nomenclature

Abbreviation	Description
AN	Acid number
BC	Boundary conditions
BN	Base number
CBR	Crude oil/brine/rock
EDL	Electric double layer
EOR	Enhanced oil recovery
ERA	Equilibrium-rate-annihilation
FDM	Finite difference method
FEM	Finite element method
FIM	Fully implicit method
FVM	Finite volume method
FW	Formation water
HS	High salinity
HLL	Harten, Lax, van Leer
IAP	Ion activity product
IC	Initial conditions
IFT	Interfacial tension
IMPESC	Implicit pressure, explicit saturations and compositions
LS	Low salinity
LSW	Low salinity waterflooding
MIE	Multicomponent ion exchange
MPFA	Multi-point flux approximation
MUSCL	Monotonic upstream-centered scheme for conservation laws
OOIP	Original oil in place
PVI	Pore volumes injected
SI	Saturation index
SPU	Single-point upwind
SW	Seawater
SWF	Smart water flooding
TPFA	Two-point flux approximation
USBM	U.S. Bureau of Mines
WI	Wettability index

WAG	Water alternating gas

Nomenclature	Description
A_{ij}	Interface area between adjacent gridblocks, $[\mathrm{m}^2]$
$\hat{A}$	Specific surface area of rock, $[\mathrm{m}^2/\mathrm{l(core)}]$
$\mathcal{A}$	Area of the capillary cross-section, $[\mathrm{m}^2]$
$\mathcal{A}_\alpha$	Area of the capillary cross-section occupied by phase α, $[\mathrm{m}^2]$
C_m	Molar concentration of mineral species, $[\mathrm{m}^2/\mathrm{l(core)}]$
c_a	Molar concentration of species in phase, $[\mathrm{m}^2/\mathrm{l}]$
c^*	Molar concentration per bulk volume, $[\mathrm{m}^2/\mathrm{l(core)}]$
$\hat{c}_{P,\alpha}$	Compressibility of phase α with regard to pressure
$\hat{c}_{wc,a}$	Compressibility of brine with regard to composition
CEC	Cation exchange capacity, $[\mathrm{eq}/\mathrm{m}^2]$
$\mathbf{D}_w$	Diffusion tensor in water
Da	Damköhler number
d_s	Surface site density, $[\mathrm{sites}/\mathrm{nm}^2]$
f_w	Fractional flow function of water
$\mathcal{F}$	Faraday's constant, $\mathcal{F} = 96485.3\ C/mol$
$\vec{\mathbf{F}}$	Flux term
G	Shape factor
$\vec{g}$	Gravitational acceleration, $g = 9.81\ \mathrm{m}/\mathrm{s}^2$
H	Interpolation function
$H_{\alpha,ij}$	Fluid part of transmissibility for phase α between adjacent gridblocks
h	Dimensionless thickness of the wetting film
I	Ionic strength, $[\mathrm{mol}/\mathrm{l}]$
$\mathbf{I}$	Identity matrix
$\mathbf{J}$	Jacobian matrix
K_n	Equilibrium constant for reaction n
k	Scalar absolute permeability, [mDa]
$\mathbf{k}$	Absolute permeability tensor, [mDa]
k_n	Rate constant for reaction n, $[\mathrm{mol}/\mathrm{m}^2/\mathrm{s}]$
k_n^f, k_n^b	Forward and backward rate constant for reaction n, $[\mathrm{mol}/\mathrm{m}^2/\mathrm{s}]$
$k_{r\alpha}$	Relative permeability of phase α
k_{rwor}, k_{rowi}	End point relative permeabilities for water and oil
L	Distance between injection and production sites, [m]
l	Length of capillary, [m]
M_a	Molar weight, $[\mathrm{kg}/\mathrm{mol}]$

$\vec{n}$	Normal vector
n_{sp}	Number of species
n_{react}	Number of reactions
N	Number of gridblocks
n_w, n_o	Corey exponents
P	Pressure, [Pa]
$\dot{r}_n$	Rate of reaction n, $[\mathrm{mol/m^3/s}]$
r_h	Hydraulic radius, [m]
$\mathbf{Q}$	Convection source term
$\mathbf{q}^{inj}$	Injection rate
q_α	Volumetric flux of phase α in capillary, $[\mathrm{m^3/s}]$
R	Gas constant, $R = 8.31\ \mathrm{J/K/mol}$
$\mathbf{S}$	Reactive source term
s, s_w	Saturation of water
s_α	Saturation of phase α
s_{or}	Residual oil saturation
s_{wi}	Irreducible water saturation
T	Absolute temperature, [K]
T_s	Sorption capacity, $[\mathrm{mol/m^2}]$
t	Time, [s]
t_D	Dimensionless time
$\mathbf{U}$	Accumulation term
u_t	Total flow velocity, $[\mathrm{m/s}]$
u_α	Flow velocity of phase α, $[\mathrm{m/s}]$
V_i	Volume of the gridblock, $[m^3]$
v_α	Flow velocity of phase in capillary, $[\mathrm{m/s}]$
$\mathbf{W}$	Primary variables
X_a	Chemical species
x	Horizontal coordinate, [m]
x_D	Dimensionless horizontal coordinate
$\vec{x}$	Spatial vector
$\vec{x}_i$	Gridblock node vector
$\vec{x}_{ij}$	Internode vector
y	Coordinate
z	Coordinate along the capillary
z_a	Charge of the species a
α_r	Water-wet fraction of surface area
β_a	Molar fractions of surface species
β_a^{GT}	Equivalent fractions of surface species
β_i	Corner half-angles
Γ	Henry adsorption constant

Γ_{ij}	Geometric part of transmissibility between adjacent gridblocks
$\Gamma_{\alpha\beta}$	Interface between phases α and β in capillary cross-section
γ_a	Activity coefficient of aqueous species
γ_m	
γ_{ow}	Interfacial tension between water and oil, $[\mathrm{mN/m}]$
Δ_i	Limited slopes for the gridblock i
δ_s	Surface charge, $[\mathrm{C/m^2}]$
ε	Dielectric constant of water
ε_0	Permittivity of free space, $\varepsilon_0 = 8.854 \times 10^{-12}\ \mathrm{F/m}$
ϵ_{tol}	Tolerance
Θ_α	Volumetric fraction of the porous medium occupied by phase α
θ	Contact angle
κ	Deposition rate, $[\mathrm{s^{-1}}]$
λ_α	Mobility of the phase α
Λ_k	Eigenvalues of the matrix
μ_α	Viscosity of phase α, [cP]
ν_a^n	Stoichiometric coefficient for species a in reaction n
Ξ_α	Pressure gradient in phase α, $[\mathrm{Pa/m}]$
Π	Perimeter of capillary cross-section, [m]
ρ_α	Density of phase α, $[\mathrm{kg/m^3}]$
σ_a	Surface molar concentration of species a, $[\mathrm{mol/m^2}]$
τ	Relaxation time
Υ_{ij}	Transmissibility between adjacent gridblocks
ϕ	Porosity
χ	Electrostatic term
ψ_s	Surface potential, [V]
Ω_i	Gridblock
$\partial\Omega_i$	Boundary of the gridblock
ω_w	Wetting fluid saturation in capillary

Indexes

a	Index for chemical species
i, j	Indexes for gridblock
inj, J	Index indicating injection
m	Index for mineral species
n	Index for time step
o	Index for oil
oa	Index for oil cluster (“active” oil)
og	Index for oil ganglia

out	Index indicating location at the outlet
s	Index for solid phase
w	Index for water
wa	Index for water cluster (“active” water)
wf	Index for water films
α	Index for phases
α_s	Index for surface species
$0, I$	Index indicating the initial state

Bibliography

[1] H. Hermansen, G. Landa, J. Sylte, and L. Thomas, "Experiences after 10 years of waterflooding the Ekofisk Field, Norway," *Journal of Petroleum Science and Engineering*, vol. 26, no. 1, pp. 11–18, 2000.

[2] T. Puntervold, S. Strand, R. Ellouz, T. Austad, *et al.*, "Why is it Possible to Produce Oil from the Ekofisk Field for Another 40 Years?," in *International Petroleum Technology Conference*, International Petroleum Technology Conference, 2014.

[3] T. Austad, S. Strand, E. Høgnesen, P. Zhang, *et al.*, "Seawater as IOR fluid in fractured chalk," in *SPE International Symposium on Oilfield Chemistry*, Society of Petroleum Engineers, 2005.

[4] S. Strand, T. Puntervold, and T. Austad, "Effect of temperature on enhanced oil recovery from mixed-wet chalk cores by spontaneous imbibition and forced displacement using seawater," *Energy & Fuels*, vol. 22, no. 5, pp. 3222–3225, 2008.

[5] P. Zhang, M. T. Tweheyo, and T. Austad, "Wettability alteration and improved oil recovery by spontaneous imbibition of seawater into chalk: Impact of the potential determining ions Ca^{2+}, Mg^{2+}, and SO_4^{2-}," *Colloids and Surfaces A: Physicochemical and Engineering Aspects*, vol. 301, no. 1, pp. 199–208, 2007.

[6] S. Strand, T. Austad, T. Puntervold, E. J. Høgnesen, M. Olsen, and S. M. F. Barstad, ""Smart water" for oil recovery from fractured limestone: a preliminary study," *Energy & fuels*, vol. 22, no. 5, pp. 3126–3133, 2008.

[7] S. J. Fathi, T. Austad, and S. Strand, ""Smart Water" as a Wettability Modifier in Chalk: The Effect of Salinity and Ionic Composition," *Energy & fuels*, vol. 24, no. 4, pp. 2514–2519, 2010.

[8] A. Zahid, E. H. Stenby, A. A. Shapiro, *et al.*, "Improved Oil Recovery in Chalk: Wettability Alteration or Something Else?," in *SPE EUROPEC/EAGE Annual Conference and Exhibition*, Society of Petroleum Engineers, 2010.

[9] R. Gupta, G. G. Smith, L. Hu, T. Willingham, M. Lo Cascio, J. J. Shyeh, C. R. Harris, *et al.*, "Enhanced waterflood for carbonate reservoirs-impact of injection water composition," in *SPE Middle East Oil and Gas Show and Conference*, Society of Petroleum Engineers, 2011.

[10] A. A. Yousef, S. H. Al-Saleh, A. Al-Kaabi, M. S. Al-Jawfi, *et al.*, "Laboratory investigation of the impact of injection-water salinity and ionic content on oil recovery from carbonate reservoirs," *SPE Reservoir Evaluation & Engineering*, vol. 14, no. 05, pp. 578–593, 2011.

[11] O. Karoussi and A. A. Hamouda, "Imbibition of sulfate and magnesium ions into carbonate rocks at elevated temperatures and their influence on wettability alteration and oil recovery," *Energy & fuels*, vol. 21, no. 4, pp. 2138–2146, 2007.

[12] J. Romanuka, J. Hofman, D. J. Ligthelm, B. Suijkerbuijk, F. Marcelis, S. Oedai, N. Brussee, H. van der Linde, H. Aksulu, T. Austad, *et al.*, "Low salinity eor in carbonates," in *SPE Improved Oil Recovery Symposium*, Society of Petroleum Engineers, 2012.

[13] S. Strand, D. C. Standnes, and T. Austad, "Spontaneous imbibition of aqueous surfactant solutions into neutral to oil-wet carbonate cores: Effects of brine salinity and composition," *Energy & fuels*, vol. 17, no. 5, pp. 1133–1144, 2003.

[14] P. Zhang, M. T. Tweheyo, and T. Austad, "Wettability alteration and improved oil recovery in chalk: The effect of calcium in the presence of sulfate," *Energy & fuels*, vol. 20, no. 5, pp. 2056–2062, 2006.

[15] A. RezaeiDoust, T. Puntervold, S. Strand, and T. Austad, "Smart water as wettability modifier in carbonate and sandstone: A discussion of similarities/differences in the chemical mechanisms," *Energy & fuels*, vol. 23, no. 9, pp. 4479–4485, 2009.

[16] H. H. Al-Attar, M. Y. Mahmoud, A. Y. Zekri, R. Almehaideb, and M. Ghannam, "Low-salinity flooding in a selected carbonate reservoir: experimental approach," *Journal of Petroleum Exploration and Production Technology*, vol. 3, no. 2, pp. 139–149, 2013.

[17] E. J. Hognesen, S. Strand, T. Austad, *et al.*, "Waterflooding of preferential oil-wet carbonates: Oil recovery related to reservoir temperature and brine composition," in *SPE Europec/EAGE Annual Conference*, Society of Petroleum Engineers, 2005.

[18] T. Puntervold, S. Strand, and T. Austad, "Water flooding of carbonate reservoirs: Effects of a model base and natural crude oil bases on chalk wettability," *Energy & fuels*, vol. 21, no. 3, pp. 1606–1616, 2007.

[19] M. T. Tweheyo, P. Zhang, T. Austad, *et al.*, "The effects of temperature and potential determining ions present in seawater on oil recovery from fractured carbonates," in *SPE/DOE Symposium on Improved Oil Recovery*, Society of Petroleum Engineers, 2006.

[20] S. J. Fathi, T. Austad, and S. Strand, "Water-based enhanced oil recovery (EOR) by "smart water": Optimal ionic composition for EOR in carbonates," *Energy & fuels*, vol. 25, no. 11, pp. 5173–5179, 2011.

[21] A. Zahid, A. A. Shapiro, A. Skauge, *et al.*, "Experimental Studies of Low Salinity Water Flooding Carbonate: A New Promising Approach," in *SPE EOR Conference at Oil and Gas West Asia*, Society of Petroleum Engineers, 2012.

[22] H. S. Al-Hadhrami, M. J. Blunt, *et al.*, "Thermally induced wettability alteration to improve oil recovery in fractured reservoirs," in *SPE/DOE Improved Oil Recovery Symposium*, Society of Petroleum Engineers, 2000.

[23] L. Yu, D. C. Standnes, and S. M. Skjæveland, "Wettability alteration of chalk by sulphate containing water, monitored by contact angle measurement," in *SCA2007-01, presented at the International Symposium of the Society of Core Analysis, Calgary*, 2007.

[24] A. Lager, K. Webb, C. Black, M. Singleton, K. Sorbie, *et al.*, "Low Salinity Oil Recovery-An Experimental Investigation," *Petrophysics*, vol. 49, no. 01, 2008.

[25] A. A. Yousef, S. Al-Saleh, M. S. Al-Jawfi, *et al.*, "Improved/enhanced oil recovery from carbonate reservoirs by tuning injection water salinity and ionic content," in *SPE Improved Oil Recovery Symposium*, Society of Petroleum Engineers, 2012.

[26] S. J. Fathi, T. Austad, S. Strand, and T. Puntervold, "Wettability alteration in carbonates: The effect of water-soluble carboxylic acids in crude oil," *Energy & Fuels*, vol. 24, no. 5, pp. 2974–2979, 2010.

[27] A. Zahid, *Smart Waterflooding in Carbonate Reservoirs*. PhD thesis, Technical University of Denmark, 2012.

[28] K. H. Chakravarty, P. L. Fosbøl, K. Thomsen, *et al.*, "Brine Crude Oil Interactions at the Oil-Water Interface,," in *SPE International Symposium on Oilfield Chemistry*, Society of Petroleum Engineers, 2015.

[29] J. Benicek, "Application of Emulsion Formed Enzymes for Enhanced Oil Recovery," Master's thesis, Technical University of Denmark, 2015.

[30] A. Zahid, A. Shapiro, E. H. Stenby, and W. Yan, "Managing injected water composition to improve oil recovery: A case study of North Sea chalk reservoirs," *Energy & Fuels*, vol. 26, no. 6, pp. 3407–3415, 2012.

[31] I. Fjelde and S. Aasen, "Improved spontaneous imbibition of water in reservoir chalks," in *IOR 2009-15th European Symposium on Improved Oil Recovery*, 2009.

[32] S. Strand, E. J. Høgnesen, and T. Austad, "Wettability alteration of carbonates—Effects of potential determining ions (Ca^{2+} and SO_4^{2-}) and temperature," *Colloids and Surfaces A: Physicochemical and Engineering Aspects*, vol. 275, no. 1, pp. 1–10, 2006.

[33] A. Hiorth, L. Cathles, and M. Madland, "The impact of pore water chemistry on carbonate surface charge and oil wettability," *Transport in porous media*, vol. 85, no. 1, pp. 1–21, 2010.

[34] M. Madland, B. Zangiabadi, R. Korsnes, S. Evje, L. Cathles, T. Kristiansen, and A. Hiorth, "Rock Fluid Interactions in Chalk with $MgCl_2$ and Na_2Cl_4 Brines with Equal Ionic Strength," in *15th European Symposium on Improved Oil Recovery*, 2009.

[35] G.-Q. Tang and N. R. Morrow, "Influence of brine composition and fines migration on crude oil/brine/rock interactions and oil recovery," *Journal of Petroleum Science and Engineering*, vol. 24, no. 2, pp. 99–111, 1999.

[36] H. Pu, X. Xie, P. Yin, N. R. Morrow, *et al.*, "Low-salinity waterflooding and mineral dissolution," in *SPE Annual Technical Conference and Exhibition*, Society of Petroleum Engineers, 2010.

[37] W. Winoto, N. Loahardjo, S. X. Xie, P. Yin, N. R. Morrow, *et al.*, "Secondary and tertiary recovery of crude oil from outcrop and reservoir rocks by low salinity waterflooding," in *SPE Improved Oil Recovery Symposium*, Society of Petroleum Engineers, 2012.

[38] K. H. Chakravarty, P. L. Fosbøl, K. Thomsen, *et al.*, "Importance of Fines in Smart Water Enhanced Oil Recovery (SmW-EOR) for Chalk Outcrops," in *EUROPEC 2015*, Society of Petroleum Engineers, 2015.

[39] D. J. Ligthelm, J. Gronsveld, J. Hofman, N. Brussee, F. Marcelis, H. van der Linde, *et al.*, "Novel waterflooding strategy by manipulation of injection brine composition.," in *EUROPEC/EAGE Conference and Exhibition*, Society of Petroleum Engineers, 2009.

[40] G. G. Bernard *et al.*, "Effect of floodwater salinity on recovery of oil from cores containing clays," in *SPE California Regional Meeting*, Society of Petroleum Engineers, 1967.

[41] P. P. Jadhunandan, *Effects of brine composition, crude oil, and aging conditions on wettability and oil recovery*. Department of Petroleum Engineering, New Mexico Institute of Mining & Technology, 1990.

[42] P. Jadhunandan and N. Morrow, "Spontaneous imbibition of water by crude oil/brine/rock systems," *In Situ;(United States)*, vol. 15, no. 4, 1991.

[43] P. Jadhunandan, N. R. Morrow, *et al.*, "Effect of wettability on waterflood recovery for crude-oil/brine/rock systems," *SPE reservoir engineering*, vol. 10, no. 01, pp. 40–46, 1995.

[44] G. Tang, N. R. Morrow, *et al.*, "Salinity, temperature, oil composition, and oil recovery by waterflooding," *SPE Reservoir Engineering*, vol. 12, no. 04, pp. 269–276, 1997.

[45] P. McGuire, J. Chatham, F. Paskvan, D. Sommer, F. Carini, *et al.*, "Low salinity oil recovery: An exciting new EOR opportunity for Alaska's North Slope," in *SPE Western Regional Meeting*, Society of Petroleum Engineers, 2005.

[46] G. R. Jerauld, K. J. Webb, C.-Y. Lin, J. C. Seccombe, *et al.*, "Modeling low-salinity waterflooding," *SPE Reservoir Evaluation & Engineering*, vol. 11, no. 06, pp. 1–000, 2008.

[47] H. Mahani, T. Sorop, D. J. Ligthelm, D. Brooks, P. Vledder, F. Mozahem, Y. Ali, *et al.*, "Analysis of field responses to low-salinity waterflooding in secondary and tertiary mode in Syria," in *SPE EUROPEC/EAGE Annual Conference and Exhibition*, Society of Petroleum Engineers, 2011.

[48] A. Omekeh, S. Evje, I. Fjelde, and H. A. Friis, "Experimental and modeling investigation of ion exchange during low salinity waterflooding," in *SCA 2011-038 presented at the International Symposium of the Society of Core Analysts, Austin, Texas, USA*, pp. 18–21, 2011.

[49] A. V. Omekeh, A, S. Evje, S., and H. A. Friis, H. A.Riis, "Modeling of low salinity effects in sandstone oil rocks," *International Journal of Numerical Analysis and Modelling*, vol. 1, no. 1, pp. 1–18, 2012.

[50] C. T. Q. Dang, L. X. Nghiem, Z. J. Chen, Q. P. Nguyen, *et al.*, "Modeling low salinity waterflooding: ion exchange, geochemistry and wettability alteration," in *SPE Annual Technical Conference and Exhibition*, Society of Petroleum Engineers, 2013.

[51] C. T. Dang, L. X. Nghiem, Z. Chen, Q. P. Nguyen, N. T. Nguyen, *et al.*, "State-of-the art low salinity waterflooding for enhanced oil recovery," in *SPE Asia Pacific Oil and Gas Conference and Exhibition*, Society of Petroleum Engineers, 2013.

[52] A. Hiorth, E. Jettestuen, L. M. Cathles, R. I. Korsnes, and M. V. Madland, "A fully Coupled Geochemical Model with a Pore Scale Lattice Boltzmann Simulator-Principles and First Results," SCA, 2010.

[53] S. Evje and A. Hiorth, "A mathematical model for dynamic wettability alteration controlled by water-rock chemistry," *NHM*, vol. 5, no. 2, pp. 217–256, 2010.

[54] S. Strand, D. Standnes, and T. Austad, "New wettability test for chalk based on chromatographic separation of SCN^- and SO_4^{2-}," *Journal of Petroleum Science and Engineering*, vol. 52, no. 1, pp. 187–197, 2006.

[55] P. V. Brady, J. L. Krumhansl, P. E. Mariner, *et al.*, "Surface complexation modeling for improved oil recovery," in *SPE Improved Oil Recovery Symposium*, Society of Petroleum Engineers, 2012.

[56] Y. Zaretskiy, *Towards modelling physical and chemical effects during wettability alteration in carbonates at pore and continuum scales*. PhD thesis, Heriot-Watt University, 2012.

[57] M. Madland, A. Hiorth, E. Omdal, M. Megawati, T. Hildebrand-Habel, R. Korsnes, S. Evje, and L. Cathles, "Chemical alterations induced by rock–fluid interactions when injecting brines in high porosity chalks," *Transport in porous media*, vol. 87, no. 3, pp. 679–702, 2011.

[58] R. Salathiel *et al.*, "Oil recovery by surface film drainage in mixed-wettability rocks," *Journal of Petroleum Technology*, vol. 25, no. 10, pp. 1–216, 1973.

[59] W. G. Anderson, "Wettability literature survey-Part 1: Rock/oil/brine interactions and the effects of core handling on wettability," *J. Pet. Technol.;(United States)*, vol. 38, no. 11, 1986.

[60] R. Johnson and R. Dettre, "Wettability and contact angles," *Surface and colloid science*, vol. 2, pp. 85–153, 1969.

[61] W. Abdallah, J. S. Buckley, A. Carnegie, J. Edwards, B. Herold, E. Fordham, A. Graue, T. Habashy, N. Seleznev, C. Signer, H. Hussain, B. Montaron, and M. Ziauddin, "Fundamentals of wettability," *Oilfield Review*, 2007.

[62] M. Leverett *et al.*, "Capillary behavior in porous solids," *Transactions of the AIME*, vol. 142, no. 01, pp. 152–169, 1941.

[63] E. C. Donaldson, R. D. Thomas, P. B. Lorenz, *et al.*, "Wettability determination and its effect on recovery efficiency," *Society of Petroleum Engineers Journal*, vol. 9, no. 01, pp. 13–20, 1969.

[64] N. R. Morrow, *Interfacial phenomena in petroleum recovery*. CRC Press, 1990.

[65] W. Anderson *et al.*, "Wettability literature survey-part 2: Wettability measurement," *Journal of Petroleum Technology*, vol. 38, no. 11, pp. 1–246, 1986.

[66] F. F. Craig, *The reservoir engineering aspects of waterflooding*. Richardson, TX: Henry L. Doherty Memorial Fund of AIME, Society of Petroleum Engineers, 1993.

[67] J. Roof *et al.*, "Snap-off of oil droplets in water-wet pores," *Society of Petroleum Engineers Journal*, vol. 10, no. 01, pp. 85–90, 1970.

[68] I. Chatzis, N. R. Morrow, H. T. Lim, *et al.*, "Magnitude and detailed structure of residual oil saturation," *Society of Petroleum Engineers Journal*, vol. 23, no. 02, pp. 311–326, 1983.

[69] W. G. Anderson *et al.*, "Wettability literature survey-part 6: the effects of wettability on waterflooding," *Journal of Petroleum Technology*, vol. 39, no. 12, pp. 1–605, 1987.

[70] L. P. Dake, *Fundamentals of reservoir engineering*. Elsevier, 1983.

[71] L. Plummer, T. Wigley, and D. Parkhurst, "The kinetics of calcite dissolution in CO2-water systems at 5 degrees to 60 degrees C and 0.0 to 1.0 atm CO_2," *American Journal of Science*, vol. 278, no. 2, pp. 179–216, 1978.

[72] C. A. J. Appelo and D. Postma, *Geochemistry, groundwater and pollution*. CRC press, 2005.

[73] O. S. Pokrovsky, S. V. Golubev, J. Schott, and A. Castillo, "Calcite, dolomite and magnesite dissolution kinetics in aqueous solutions at acid to circumneutral pH, 25 to 150 C and 1 to 55 atm pCO2: new constraints on CO_2 sequestration in sedimentary basins," *Chemical geology*, vol. 265, no. 1, pp. 20–32, 2009.

[74] D. Hasson and J. Zahavi, “Mechanism of calcium sulfate scale deposition on heat transfer surfaces,” *Industrial & Engineering Chemistry Fundamentals*, vol. 9, no. 1, pp. 1–10, 1970.

[75] C. M. Bethke, *Geochemical and biogeochemical reaction modeling*. Cambridge University Press, 2007.

[76] R. S. Arvidson, I. E. Ertan, J. E. Amonette, and A. Luttge, “Variation in calcite dissolution rates:: A fundamental problem?,” *Geochimica et cosmochimica acta*, vol. 67, no. 9, pp. 1623–1634, 2003.

[77] J. A. Davis and D. Kent, “Surface complexation modeling in aqueous geochemistry,” *Reviews in Mineralogy and Geochemistry*, vol. 23, no. 1, pp. 177–260, 1990.

[78] P. A. Domenico and F. W. Schwartz, *Physical and chemical hydrogeology*, vol. 44. Wiley New York, 1998.

[79] A. W. Adamson, A. P. Gast, *et al.*, *Physical chemistry of surfaces*. Interscience publishers New York, 1967.

[80] W. Stumm and J. Morgan, “Aquatic chemistry, chemical equilibra and rates in natural waters,” *Environmental Science and Technology Series*, 1996.

[81] G. Sposito, *The chemistry of soils*. Oxford university press, 2008.

[82] J. N. Israelachvili, *Intermolecular and surface forces: revised third edition*. Academic press, 2011.

[83] D. A. Dzombak and F. M. Morel, *Surface complexation modeling: hydrous ferric oxide*. John Wiley & Sons, 1990.

[84] D. C. Grahame, “The electrical double layer and the theory of electrocapillarity,” *Chemical reviews*, vol. 41, no. 3, pp. 441–501, 1947.

[85] S. E. Buckley, M. Leverett, *et al.*, “Mechanism of fluid displacement in sands,” *Transactions of the AIME*, vol. 146, no. 01, pp. 107–116, 1942.

[86] G. A. Pope *et al.*, “The application of fractional flow theory to enhanced oil recovery,” *Society of Petroleum Engineers Journal*, vol. 20, no. 03, pp. 191–205, 1980.

[87] R. Brooks and T. Corey, “Hydraulic properties of porous media,” 1964.

[88] L. W. Lake, *Enhanced oil recovery*. Old Tappan, NJ; Prentice Hall Inc., 1989.

[89] H. J. Welge *et al.*, “A simplified method for computing oil recovery by gas or water drive,” *Journal of Petroleum Technology*, vol. 4, no. 04, pp. 91–98, 1952.

[90] J. S. Archer and C. G. Wall, *Petroleum engineering: principles and practice*. Springer Science & Business Media, 2012.

[91] P. Donnez, *Essentials of reservoir engineering*, vol. 2. TECHNIP OPHRYS EDITIONS, 2012.

[92] P. Bedrikovetsky, *Mathematical theory of oil and gas recovery: with applications to ex-USSR oil and gas fields*, vol. 4. Springer Science & Business Media, 1993.

[93] J. Sheng, *Modern chemical enhanced oil recovery: theory and practice*. Gulf Professional Publishing, 2010.

[94] R. Courant and K. O. Friedrichs, *Supersonic flow and shock waves*, vol. 21. Springer Science & Business Media, 1999.

[95] U. Korsbech, H. Aage, K. Hedegaard, B. L. Andersen, N. Springer, *et al.*, "Measuring and modeling the displacement of connate water in chalk core plugs during water injection," *SPE Reservoir Evaluation & Engineering*, vol. 9, no. 03, pp. 259–265, 2006.

[96] J. Patton, K. Coats, G. Colegrove, *et al.*, "Prediction of polymer flood performance," *Society of Petroleum Engineers Journal*, vol. 11, no. 01, pp. 72–84, 1971.

[97] W. Foster *et al.*, "A low-tension waterflooding process," *Journal of Petroleum Technology*, vol. 25, no. 02, pp. 205–210, 1973.

[98] R. Larson *et al.*, "Analysis of the physical mechanisms in surfactant flooding," *Society of Petroleum Engineers Journal*, vol. 18, no. 01, pp. 42–58, 1978.

[99] E. F. Toro, *Riemann solvers and numerical methods for fluid dynamics: a practical introduction*. Springer Science & Business Media, 2009.

[100] L. Nghiem, P. Sammon, J. Grabenstetter, H. Ohkuma, *et al.*, "Modeling CO_2 storage in aquifers with a fully-coupled geochemical EOS compositional simulator," in *SPE/DOE symposium on improved oil recovery*, Society of Petroleum Engineers, 2004.

[101] C. Hirsch, *Numerical Computation of Internal and External Flows: The Fundamentals of Computational Fluid Dynamics*, vol. 1. Butterworth-Heinemann, 2007.

[102] Z. Chen, *Reservoir simulation: mathematical techniques in oil recovery*, vol. 77. SIAM, 2007.

[103] R. J. LeVeque, *Finite difference methods for ordinary and partial differential equations: steady-state and time-dependent problems*, vol. 98. Siam, 2007.

[104] H. K. Versteeg and W. Malalasekera, *An introduction to computational fluid dynamics: the finite volume method*. Pearson Education, 2007.

[105] K. Aziz and A. Settari, *Petroleum reservoir simulation*. Chapman & Hall, 1979.

[106] J. H. Abou-Kassem, S. Farouq-Ali, and M. R. Islam, *Petroleum Reservoir Simulations*. Elsevier, 2013.

[107] J. Cordazzo, C. R. Maliska, and A. Silva, "Interblock transmissibility calculation analysis for petroleum reservoir simulation," in *2nd Meeting on Reservoir Simulation, Universidad Argentina de la Empresa, Buenos Aires, Argentina, November*, pp. 5–6, 2002.

[108] G. L. Chierici, *Principles of petroleum reservoir engineering*, vol. 2. Springer Science & Business Media, 2012.

[109] L. F. Shampine, *Numerical solution of ordinary differential equations*, vol. 4. CRC Press, 1994.

[110] J. M. Ortega and W. C. Rheinboldt, *Iterative solution of nonlinear equations in several variables*, vol. 30. Siam, 1970.

[111] J. J. Moré, B. S. Garbow, and K. E. Hillstrom, "User guide for MINPACK-1," tech. rep., CM-P00068642, 1980.

[112] D. E. van Odyck, S. Lovett, F. Monmont, and N. Nikiforakis, "An efficient shock capturing scheme for multicomponent multiphase thermal flow in porous media," in *Proceedings of the Royal Society of London A: Mathematical, Physical and Engineering Sciences*, p. rspa20120152, The Royal Society, 2012.

[113] M. B. Alotaibi, H. A. Nasr-El-Din, *et al.*, "Chemistry of injection water and its impact on oil recovery in carbonate and clastics formations," in *SPE international symposium on oilfield chemistry*, Society of Petroleum Engineers, 2009.

[114] T. Austad, S. Shariatpanahi, S. Strand, C. Black, and K. Webb, "Conditions for a low-salinity enhanced oil recovery (EOR) effect in carbonate oil reservoirs," *Energy & fuels*, vol. 26, no. 1, pp. 569–575, 2011.

[115] A. C. Lasaga, "Chemical kinetics of water-rock interactions," *Journal of Geophysical Research: Solid Earth (1978–2012)*, vol. 89, no. B6, pp. 4009–4025, 1984.

[116] O. Singurindy and B. Berkowitz, "Evolution of hydraulic conductivity by precipitation and dissolution in carbonate rock," *Water Resources Research*, vol. 39, no. 1, 2003.

[117] P. G. Bedrikovetsky, E. J. Mackay, R. M. Silva, F. M. Patricio, and F. F. Rosário, "Produced water re-injection with seawater treated by sulphate reduction plant: Injectivity decline, analytical model," *Journal of Petroleum Science and Engineering*, vol. 68, no. 1, pp. 19–28, 2009.

[118] P. Bedrikovetsky, R. M. Silva, J. S. Daher, J. A. Gomes, and V. C. Amorim, "Well-data-based prediction of productivity decline due to sulphate scaling," *Journal of Petroleum Science and Engineering*, vol. 68, no. 1, pp. 60–70, 2009.

[119] S. Houston, B. Yardley, P. Smalley, and I. Collins, "Precipitation and dissolution of minerals during waterflooding of a North Sea oil field," *paper SPE*, vol. 100603, 2006.

[120] E. Aharonov, M. Spiegelman, and P. Kelemen, "Three-dimensional flow and reaction in porous media: Implications for the Earth's mantle and sedimentary basins," *JOURNAL OF GEOPHYSICAL RESEARCH-ALL SERIES-*, vol. 102, pp. 14–821, 1997.

[121] J. Spivey, W. McCain Jr, R. North, *et al.*, "Estimating density, formation volume factor, compressibility, methane solubility, and viscosity for oilfield brines at temperatures from 0 to 275C, pressures to 200 MPa, and salinities to 5.7 mole/kg," *Journal of Canadian Petroleum Technology*, vol. 43, no. 07, 2004.

[122] E. J. Lam, M. N. Alvarez, M. E. Galvez, and E. B. Alvarez, "A model for calculating the density of aqueous multicomponent electrolyte solutions," *Journal of the Chilean Chemical Society*, vol. 53, no. 1, pp. 1393–1398, 2008.

[123] J. Rubin, "Transport of reacting solutes in porous media: Relation between mathematical nature of problem formulation and chemical nature of reactions," *Water resources research*, vol. 19, no. 5, pp. 1231–1252, 1983.

[124] A. Settari, F. Mourits, *et al.*, "A coupled reservoir and geomechanical simulation system," *Spe Journal*, vol. 3, no. 03, pp. 219–226, 1998.

[125] R. P. Chapuis and M. Aubertin, *Predicting the coefficient of permeability of soils using the Kozeny-Carman equation*. École polytechnique de Montréal, 2003.

[126] M. M. Alam, I. L. Fabricius, and M. Prasad, "Permeability prediction in chalks," *AAPG bulletin*, vol. 95, no. 11, pp. 1991–2014, 2011.

[127] M. J. Blunt, "Flow in porous media—pore-network models and multiphase flow," *Current opinion in colloid & interface science*, vol. 6, no. 3, pp. 197–207, 2001.

[128] P. H. Valvatne, *Predictive pore-scale modelling of multiphase flow*. PhD thesis, Imperial College London, 2004.

[129] P. H. Valvatne, M. Piri, X. Lopez, and M. J. Blunt, "Predictive pore-scale modeling of single and multiphase flow," in *Upscaling Multiphase Flow in Porous Media*, pp. 23–41, Springer, 2005.

[130] T. W. Patzek *et al.*, "Verification of a complete pore network simulator of drainage and imbibition," in *SPE/DOE Improved Oil Recovery Symposium*, Society of Petroleum Engineers, 2000.

[131] T. Patzek and J. Kristensen, "Shape factor correlations of hydraulic conductance in noncircular capillaries: II. Two-phase creeping flow," *Journal of colloid and interface science*, vol. 236, no. 2, pp. 305–317, 2001.

[132] T. Patzek and D. Silin, "Shape factor and hydraulic conductance in noncircular capillaries: I. One-phase creeping flow," *Journal of colloid and interface science*, vol. 236, no. 2, pp. 295–304, 2001.

[133] A. Ryazanov, M. Van Dijke, and K. Sorbie, "Two-phase pore-network modelling: existence of oil layers during water invasion," *Transport in Porous Media*, vol. 80, no. 1, pp. 79–99, 2009.

[134] P.-E. Oren, S. Bakke, O. J. Arntzen, *et al.*, "Extending predictive capabilities to network models," *SPE Journal*, vol. 3, no. 04, pp. 324–336, 1998.

[135] W. Rose, "Coupling coefficients for two-phase flow in pore spaces of simple geometry," *Transport in Porous Media*, vol. 5, no. 1, pp. 97–102, 1990.

[136] A. A. Shapiro, "Two-Phase Immiscible Flows in Porous Media: The Mesocopic Maxwell–Stefan Approach," *Transport in Porous Media*, vol. 107, no. 2, pp. 335–363, 2015.

[137] F. U. Guide, *Version 5.0, PDE Solutions*, 2005.

[138] A. Payatakes, "Dynamics of oil ganglia during immiscible displacement in water-wet porous media," *Annual Review of Fluid Mechanics*, vol. 14, no. 1, pp. 365–393, 1982.

[139] P. Bedrikovetsky *et al.*, "A new mathematical model for EOR displacements honouring oil ganglia," in *SPE Annual Technical Conference and Exhibition*, Society of Petroleum Engineers, 1997.

[140] D. W. Green, *Enhanced oil recovery*. 1998.

[141] M. Gray, A. Yeung, J. Foght, H. W. Yarranton, *et al.*, "Potential microbial enhanced oil recovery processes: a critical analysis," in *SPE Annual Technical Conference and Exhibition*, Society of Petroleum Engineers, 2008.

[142] A. Halim, A. Shapiro, A. E. Lantz, and S. M. Nielsen, "Experimental study of bacterial penetration into chalk rock: mechanisms and effect on permeability," *Transport in porous media*, vol. 101, no. 1, pp. 1–15, 2014.

[143] T. Austad, "Water-Based EOR in Carbonates and Sandstones: New Chemical Understanding of the EOR Potential Using Smart Water," *Enhanced Oil Recovery Field Case Studies*, pp. 301–335, 2013.

[144] R. Lenormand, C. Zarcone, and A. Sarr, "Mechanisms of the displacement of one fluid by another in a network of capillary ducts," *Journal of Fluid Mechanics*, vol. 135, pp. 337–353, 1983.

[145] E. J. Spiteri, R. Juanes, M. J. Blunt, F. M. Orr, *et al.*, "A new model of trapping and relative permeability hysteresis for all wettability characteristics," *Spe Journal*, vol. 13, no. 03, pp. 277–288, 2008.

[146] C. H. Pentland, E. Itsekiri, S. Al-Mansoori, S. Iglauer, B. Bijeljic, M. J. Blunt, *et al.*, "Measurement of nonwetting-phase trapping in sandpacks," *Spe Journal*, vol. 15, no. 02, pp. 274–281, 2010.

[147] H. Princen, "Capillary phenomena in assemblies of parallel cylinders: II. Capillary rise in systems with more than two cylinders," *Journal of Colloid and Interface Science*, vol. 30, no. 3, pp. 359–371, 1969.

[148] A. V. Ryazanov, M. I. van Dijke, K. S. Sorbie, *et al.*, "Pore-network prediction of residual oil saturation based on oil layer drainage in mixed-wet systems," in *SPE Improved Oil Recovery Symposium*, Society of Petroleum Engineers, 2010.

[149] N. R. Morrow *et al.*, "Wettability and its effect on oil recovery," *Journal of Petroleum Technology*, vol. 42, no. 12, pp. 1–476, 1990.

[150] X. Zhao, M. J. Blunt, and J. Yao, "Pore-scale modeling: Effects of wettability on waterflood oil recovery," *Journal of Petroleum Science and Engineering*, vol. 71, no. 3, pp. 169–178, 2010.

[151] K. P. Abeysinghe, I. Fjelde, A. Lohne, *et al.*, "Dependency of Remaining Oil Saturation on Wettability and Capillary Number," in *SPE Saudi Arabia Section Technical Symposium and Exhibition*, Society of Petroleum Engineers, 2012.

[152] K. A. Rezaei Gomari, O. Karoussi, A. A. Hamouda, *et al.*, "Mechanistic study of interaction between water and carbonate rocks for enhancing oil recovery," in *SPE Europec/EAGE Annual Conference and Exhibition*, Society of Petroleum Engineers, 2006.

[153] M. B. Alotaibi, R. Azmy, H. A. Nasr-El-Din, *et al.*, "Wettability challenges in carbonate reservoirs," in *SPE Improved Oil Recovery Symposium*, Society of Petroleum Engineers, 2010.

[154] A. Seethepalli, B. Adibhatla, K. Mohanty, *et al.*, "Wettability alteration during surfactant flooding of carbonate reservoirs," in *SPE/DOE Symposium on Improved Oil Recovery*, Society of Petroleum Engineers, 2004.

[155] D. C. Standnes and T. Austad, "Wettability alteration in chalk: 2. Mechanism for wettability alteration from oil-wet to water-wet using surfactants," *Journal of Petroleum Science and Engineering*, vol. 28, no. 3, pp. 123–143, 2000.

[156] H. Nasiri, K. Spildo, and A. Skauge, "Use of enzymes to improve waterflood Performance," in *International Symposium of the Society of Core Analysts*, pp. 27–30, 2009.

[157] R. Sen, "Biotechnology in petroleum recovery: the microbial EOR," *Progress in Energy and Combustion Science*, vol. 34, no. 6, pp. 714–724, 2008.

[158] B. Soraya, C. Malick, C. Philippe, H. J. Bertin, G. Hamon, *et al.*, "Oil recovery by low-salinity brine injection: Laboratory results on outcrop and reservoir cores," in *SPE Annual Technical Conference and Exhibition*, Society of Petroleum Engineers, 2009.

[159] N. Hadia, H. H. Lehne, K. G. Kumar, K. A. Selboe, F. Å. Stensen, O. Torsater, *et al.*, "Laboratory Investigation of Low Salinity Waterflooding on Reservoir Rock Samples from the Froy Field," in *SPE Middle East Oil and Gas Show and Conference*, Society of Petroleum Engineers, 2011.

[160] C. Callegaro, M. Bartosek, F. Masserano, M. Nobili, P. Parracello, V. Parasiliti, C. S. Pizzinelli, A. Caschili, *et al.*, "Opportunity of Enhanced Oil Recovery Low Salinity Water Injection: From Experimental Work to Simulation Study up to Field Proposal," in *EAGE Annual Conference & Exhibition incorporating SPE Europec*, Society of Petroleum Engineers, 2013.

[161] A. Y. Halim, S. M. Nielsen, A. E. Lantz, V. S. Suicmez, N. Lindeloff, and A. Shapiro, "Investigation of spore forming bacterial flooding for enhanced oil recovery in a North Sea chalk reservoir," *Journal of Petroleum Science and Engineering*, vol. 133, pp. 444–454, 2015.

[162] K. S. Sorbie, I. Collins, *et al.*, "A proposed pore-scale mechanism for how low salinity waterflooding works," in *SPE Improved Oil Recovery Symposium*, Society of Petroleum Engineers, 2010.

[163] P. Bedrikovetsky, "WAG displacements of oil-condensates accounting for hydrocarbon ganglia," *Transport in porous media*, vol. 52, no. 2, pp. 229–266, 2003.

[164] A. Hunt, R. Ewing, and B. Ghanbarian, *Percolation theory for flow in porous media*, vol. 880. Springer, 2014.

[165] E. M. Schlueter, "Predicting the transport properties of sedimentary rocks from microstructure," tech. rep., Lawrence Livermore National Lab., CA (United States), 1995.

[166] R. Larson, L. Scriven, and H. Davis, "Percolation theory of two phase flow in porous media," *Chemical Engineering Science*, vol. 36, no. 1, pp. 57–73, 1981.

[167] P. Zhang and T. Austad, "Wettability and oil recovery from carbonates: Effects of temperature and potential determining ions," *Colloids and Surfaces A: Physicochemical and Engineering Aspects*, vol. 279, no. 1, pp. 179–187, 2006.

[168] P. Frykman, "Spatial variability in petrophysical properties in Upper Maastrichtian chalk outcrops at Stevns Klint, Denmark," *Marine and Petroleum Geology*, vol. 18, no. 10, pp. 1041–1062, 2001.

[169] M. Megawati, A. Hiorth, and M. Madland, "The impact of surface charge on the mechanical behavior of high-porosity chalk," *Rock mechanics and rock engineering*, vol. 46, no. 5, pp. 1073–1090, 2013.

[170] S. Evje, A. Hiorth, M. V. Madland, and R. I. Korsnes, "A mathematical model relevant for weakening of chalk reservoirs due to chemical reactions," *NHM*, vol. 4, no. 4, pp. 755–788, 2009.

[171] A. V. Omekeh, H. A. Friis, I. Fjelde, S. Evje, *et al.*, "Modeling of ion-exchange and solubility in low salinity water flooding," in *SPE improved oil recovery symposium*, Society of Petroleum Engineers, 2012.

[172] O. Pokrovsky and J. Schott, "Surface chemistry and dissolution kinetics of divalent metal carbonates," *Environmental science & technology*, vol. 36, no. 3, pp. 426–432, 2002.

[173] D. L. Parkhurst, C. Appelo, *et al.*, *User's guide to PHREEQC (Version 2): A computer program for speciation, batch-reaction, one-dimensional transport, and inverse geochemical calculations*, 1999.

[174] A. Stogryn, "Equations for calculating the dielectric constant of saline water (correspondence)," *IEEE transactions on microwave theory and Techniques*, pp. 733–736, 1971.

[175] M. Uematsu and E. Frank, “Static dielectric constant of water and steam,” *Journal of Physical and Chemical Reference Data*, vol. 9, no. 4, pp. 1291–1306, 1980.

[176] J. R. Fanchi, *Principles of applied reservoir simulation*. Gulf Professional Publishing, 2005.

[177] O. Y. Dinariev and D. Mikhailov, “Modeling of isothermal processes in porous materials on the basis of the concept of an ensemble of pores,” *Fluid Dynamics*, vol. 42, no. 5, pp. 784–797, 2007.

Center for Energy Resources Engineering
Department of Chemical and
Biochemical Engineering
Technical University of Denmark

Søltofts Plads, Building 229
DK-2800 Kgs. Lyngby
Tlf. +45 4525 2800
Fax +45 4525 4588

www.cere.dtu.dk